Equilibrium and Stability Studies of Plasmas Confined in a Dipole Magnetic Field Using Magnetic Measurements

by

Ishtak Karim

Submitted to the Department of Nuclear Science and Engineering
in partial fulfillment of the requirements for the degree of

Doctor of Science in Applied Plasma Physics

at the

MASSACHUSETTS INSTITUTE OF TECHNOLOGY

February 2007

Author .....
Department of Nuclear Science and Engineering
January 12, 2007

Certified by .....
Jay Kesner
Senior Research Scientist
Thesis Supervisor

Certified by .....
Darren Garnier
Research Scientist, Columbia University
Thesis Cosupervisor

Certified by .....
Ron Parker
Professor of Nuclear Engineering
Thesis Reader

Accepted by .....
Jeffrey A. Coderre
Chairman, Department Committee on Graduate Students

Equilibrium and Stability Studies of Plasmas Confined in a Dipole Magnetic Field Using Magnetic Measurements

by

Ishtak Karim

Submitted to the Department of Nuclear Science and Engineering
on January 12, 2007, in partial fulfillment of the
requirements for the degree of
Doctor of Science in Applied Plasma Physics

Abstract

The Levitated Dipole Experiment (LDX) is the first experiment of its kind to use a levitated current ring to confine a plasma in a dipole magnetic field. The plasma is stabilized by compressibility and can theoretically attain a peak beta on the order of unity. Various magnetic sensors have been designed, calibrated, installed, and operated to measure the plasma current, from which the pressure profile is deduced through a mathematical process called reconstruction. Both isotropic and anisotropic models are introduced and used to obtain the equilibrium. The need for an anisotropic pressure model is evident since electron cyclotron resonance heating produces highly anisotropic plasmas in LDX. Compared to the isotropic pressure models, the anisotropic model predicts a larger peak beta for a given set of magnetic measurements due to a modification in the current-pressure relationship. We have achieved a peak beta in excess of 26 % using the anisotropic model.

One of the important results of this work involves characterizing the properties of reconstructing LDX plasmas. Because the floating coil is superconducting, it must be ensured that the flux linked to it is kept constant while deducing the plasma current. A significant difficulty in reconstructing LDX plasmas is that the magnetic sensors are sensitive mostly to the plasma dipole moment due to their large distances from the plasma. This means that a family of current and pressure profiles with the same dipole moment fits the magnetic measurements equally well. X-ray emissivity data is used as a supplemental measurement to unequivocally determine the pressure profile. Simulation results show that adding internal flux loops close to the plasma can increase their sensitivity to higher order moments.

In addition to demonstrating the feasibility of achieving high beta, the magnetic diagnostics have decisively shown that LDX plasmas routinely have supercritical pressure profiles that exceed the MHD limit. The plasmas we have achieved to date have a significant fraction of hot electrons, which are susceptible to a kinetic analog of the MHD interchange mode called the hot electron interchange mode (HEI). Although the MHD gradient limit is slightly increased by incorporating pressure anisotropy, the best fit profile usually gives a pressure gradient that substantially exceeds even the

anisotropic limit. Magnetic measurements therefore confirm that the hot electrons are not subject to the MHD interchange mode, and the HEI is the relevant instability. The HEI's have been measured by Mirnov coils, and their occurrences have been correlated to drops in flux measurements. Lastly, a stored energy-plasma current relationship has been derived, and its result has been used to estimate the energy confinement time of LDX plasmas with different heating frequency compositions.

Thesis Supervisor: Jay Kesner
Title: Senior Research Scientist

Acknowledgments

I would hereby like to acknowledge the people in my group who have made this work possible. Jay Kesner for being the laid back advisor who never breathed down behind my neck and allowed me to do my research freely. Darren Garnier for leading the way and advising me on both engineering and physics issues and giving me logistic support when needed. Mike Mauel for always being keen on the details of what I did. Alex Hansen for letting me use his credit card. Jennifer Ellsworth for supplementing my below average computer skills. Eugene Ortiz for broaching all kinds of physics questions related to my measurements and pushing me when necessary. Alex Boxer for being more absent than I am and attending me for hours while I worked inside the vessel and engaging me with interesting conversations from time to time. Austin Roach and Daniel Benitez for allowing me to abuse you as UROPs. Rick Lations for letting me use his tools and forgiving me when I drank his coffee. Lastly, but not leastly, Don Strahan for welding many many studs for me inside the vessel wearing a heat-maintaining bunny suit in the 110° chamber. Thank you all.

My thanks also go to my reader, Ron Parker, and the committee members for my defense, Ian Hutchinson and Jeff Freidberg.

Contents

List of Figures

List of Tables

Chapter 1

Introduction

The Levitated Dipole Experiment (LDX) is a joint MIT-Columbia experiment that studies the basic physics of a plasma confined in a dipole magnetic field [20]. Its global goal is to demonstrate the feasibility of sustaining a stable, high-beta plasma in this unique and simple magnetic configuration. LDX is first of its kind amongst other dipole confinement experiments in terms of its large size. It is also the first experiment to utilize plasma compressibility for its stability. LDX is a culmination of recent advances made in superconductor technology along with a better understanding of relevant plasma theory that predicts the possibility of a good dipolar confinement.

1.1 Fusion as a Power Source

Magnetic confinement of hot and dense plasmas may be the most viable method for attaining controlled nuclear fusion, and it therefore plays an important role in making cheap energy from fusion power a reality. Fusion energy production may soon by approaching the break-even point (i.e. getting as much power out as putting in), but its high cost of production prevents it from becoming an economically viable alternative to coal, petroleum, and nuclear fission. Only when we nearly exhaust our fossil fuel availability (in a few decades) may fusion become an economically competitive source of energy. However, economics is not the sole arbiter of energy choices, and increasing environmental awareness among the populous is driving the

need for clean energy sources. Because fusion is relatively clean and has a semi-infinite source of fuel, it is unquestionably one of the most important energy sources of the future.

The most extensively studied and tested device for doing plasma confinement is the tokamak. Although the tokamak may be the most promising machine for becoming the prototype of a future reactor, it is not without disadvantages, and numerous other types of "alternate concept" machines have been studied. One of them derives from the concept of confining a plasma in a dipolar magnetic field. The motivation for using a dipole magnetic configuration for plasma confinement comes from numerous observations made by astronomers and astrophysicists concerning planetary plasma confinement. One of the important things learned from these observations is that one of the planets, namely Jupiter, confines plasma very efficiently with a local maximum β on the order of unity. Such a high β is unheard of in any conventional tokamak (i.e. excluding spherical torii), and fusion scientists began to think about adopting this confinement scheme to a laboratory setting to study its plasma physics. Akira Hasegawa is credited for envisioning the use of a dipole field created by a levitated ring to confine a hot plasma for fusion power generation [15, 16]. LDX has been designed to test the feasibility of such a confinement scheme.

1.2 LDX Hardware

The Levitated Dipole Experiment roughly consists of a large vacuum vessel ($80m^3$) and three superconducting magnets [10] (Figure 1-1). The vacuum vessel is constructed of 3/4" thick stainless steel to maintain its structural integrity while minimizing eddy currents. Each of the three magnets plays an integral role in the operation of the experiment. Additional components of the experiment consist of Helmholtz shaping coils, diagnostic sensors, and various pumps to evacuate the vessel.

The floating coil (F-coil) is the magnet that produces the necessary dipole field to confine the plasma (Figure 1-2). It consists of a central Nb_3Sn conductor surrounded by three concentric toroidal structures. The inner most torus is a helium pressure

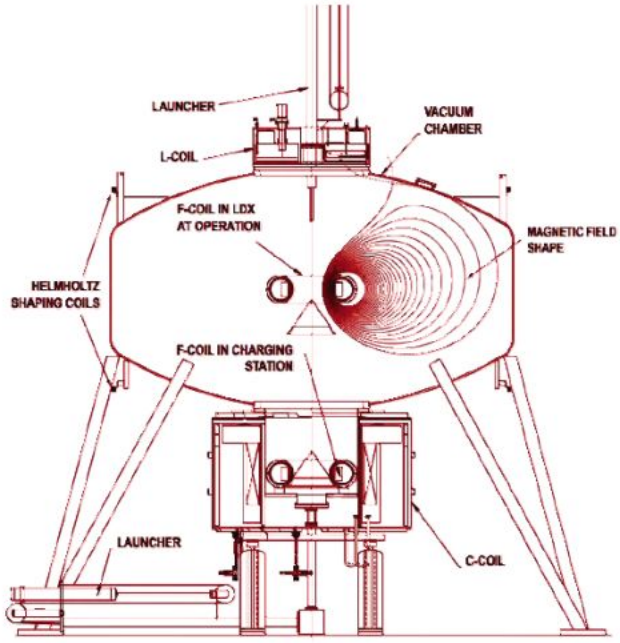

Figure 1-1: A schematic view of the LDX apparatus.

vessel that contains super-cold helium gas to keep the conductor below its critical temperature. The middle shell is made of lead and protects the conductor from heating up with its high heat capacity. The outermost structure is a stainless steel vacuum vessel that keeps the internal components under vacuum. The coil weighs about 550 kg and has an outer radius of 58.5 cm. The magnet can carry up to 1.5 MA of current and remain superconducting for more than 2 hours. At its maximum current, the magnet produces a peak field in the plasma of greater than 3 Tesla.

The largest magnet of the experiment is the charging coil (C-coil) (Figure 1-3). This large magnet is used to inductively charge the F-coil in a relatively short time (30 min). It has a bore diameter of 1.2 m, just large enough to fit the F-coil. The bore of the coil surrounds the housing (charging station) in which the F-coil sits while it is being charged. Its conductor is made of NbTi and can carry enough current to produce a peak field of 4.3 Tesla. The conductor is enclosed in a large stainless steel casing that contains a cryostat that keeps the magnet cold.

While the F-coil and C-coil are traditional low-temperature superconducting magnets, the levitation coil (L-coil) uses a high-temperature superconducting material (Figure 1-4). Its BSCCO conductor can stay superconducting at above 20 K, eliminating the need to use excessive amounts of expensive liquid helium. As its name implies, the L-coil's primary function is to keep the F-coil levitated. This entails providing the necessary field at all times to keep the F-coil at its equilibrium position. A simple mechanical analysis shows that a floating magnet supported by another magnet from the top is tilt and horizontally stable but vertically unstable. Hence, the L-coil is controlled by a fast feedback system that acquires its signals from a set of laser detectors that measures the F-coil's deviation from its equilibrium position. The corrective current is typically less than 1% of the equilibrium operating current. The L-coil is being tested at the time of this writing, and LDX has been operating in the "supported mode," in which the F-coil is supported by solid spokes, thus far. LDX is the first experiment to use a high-temperature superconductor in the US fusion energy program.

Finally, LDX is equipped with a pair of Helmholtz coils (H-coils) that can impose a spatially uniform vertical field on the plasma. These coils use standard copper conductors, and each can carry a current of up to about 80 kA-turns. With a radius and vertical separation of 2.44 m, the coils can produce a near-uniform field of close to 300 G in the plasma at maximum current. However, the resistive heating of the coils limits the pulse time and/or duty cycle at high operating currents.

1.3 Diagnostics

In order to study the properties of the plasmas produced in LDX, multifarious diagnostics have been installed in, on, and around the machine. Because LDX is a new experiment, only the most basic set of diagnostics has been commissioned to date. Nevertheless, they can give important information that is needed to understand the plasmas.

The current set of diagnostics on LDX includes various electric (Langmuir) probes,

Figure 1-2: The floating coil.

Figure 1-3: The charging coil.

Figure 1-4: The levitation coil.

a four-channel x-ray pulse height analyzer, an x-ray camera, a photodiode array, a single channel microwave interferometer, and an assortment of magnetic diagnostics. Some of these sensors allow us to measure different plasma parameters while others measure similar properties and serve as complimentary diagnostics. There are multiple sets of moveable and fixed Langmuir probes that operate in different modes. Some are biased at a fixed voltage while others are voltage swept to obtain current-voltage characteristics. The probes that are kept at a fixed voltage allow us to measure and characterize electrostatic fluctuations whereas those that are swept give density and temperature measurements. Because the swept probes are voltage swept many times over one shot, sufficient time resolution can be obtained for these measurements. Since the probes can significantly perturb the plasma and cannot withstand too much heat flux, probe measurements are limited to the plasma edge.

X-ray diagnostics are primarily used to measure the energy of the hot electron species produced by electron cyclotron resonance heating (ECRH) of LDX plasma. A 4-channel pulse height analyzer gives the energy distribution of the collected electrons, from which temperature information can be deduced. An x-ray camera converts the x-ray intensity to a visible light intensity on a phosphor screen. Hence, a line integrated x-ray intensity can be attained through proper calibration. Because both of these measurements are line integrated measurements, a proper inversion scheme (i.e. Abel inversion) must be employed in order to obtain any spatial resolution of the data.

A heterodyne interferometer is used in LDX to measure its core plasma density. As with the x-ray measurements, the interferometer measures a line integrated value and hence requires more than one chord to get a spatial resolution. The interferometer system has not been completed at this time and only uses a single chord. Although the current system can only measure line integrated density values, it will be upgraded in the near future to include multiple chords to allow for the measurement of density profiles.

LDX has a sizable set of magnetic diagnostics for equilibrium and perturbation measurements. Their details will be discussed in the next chapter and hence will

not be elaborated here. Figure 1-5 summarizes the locations of the diagnostics with respect to the vacuum vessel.

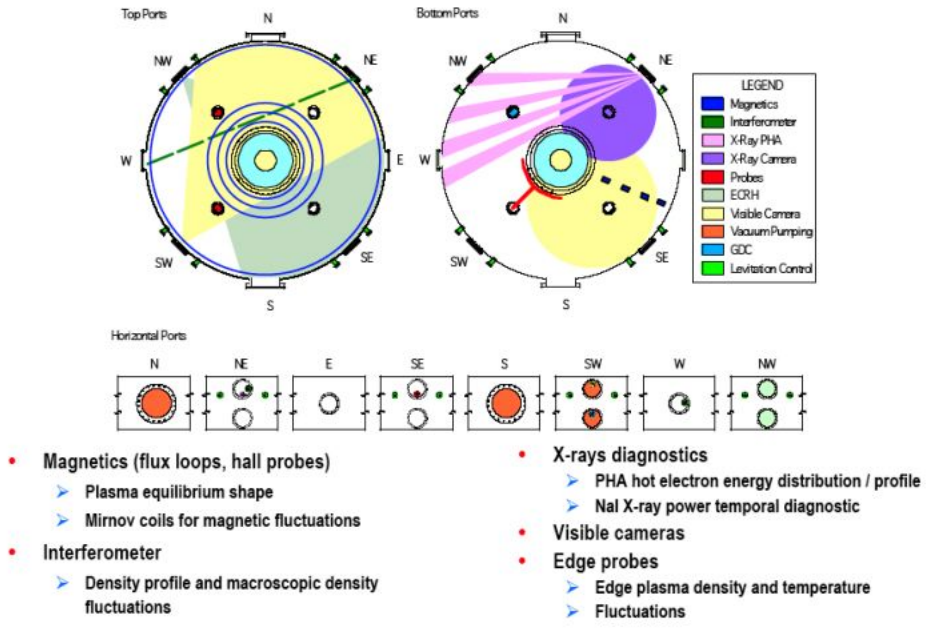

Figure 1-5: The locations of different diagnostics. The initial sets of diagnostics include magnetics, electric probes, x-ray detectors, and a single-chord interferometer.

1.4 Experimental Goals, Procedures, and Accomplishments

The Levitated Dipole Experiment is designed to test the feasibility of concept for realizing a future levitated dipole fusion reactor. To this end, the experiment serves as establishing the physics feasibility of heating, confining, and sustaining a high beta plasma in the dipole magnetic configuration. LDX is not a proof of concept experiment in the sense that it does not address the effects of a burning plasma on the hardware or on the plasma itself. In addition to fulfilling its role as a fusion experiment, LDX is an excellent testing bed to study the physics of planetary and

stellar plasmas. The magnetic field of LDX is designed to mimic that of planets and stars as previously mentioned, hence it is only natural that LDX plasmas are relevant for learning and understanding plasmas that occur naturally in space.

One of the key questions LDX must answer is whether it can sustain a high beta plasma. The answer to this question has already been half-obtained. LDX has attained a peak local beta in excess of 20%. However, attaining high beta by itself is not sufficient; we need to understand the conditions that lead to the creation of high beta plasmas and gain a physical insight into how these conditions facilitate such creation. Only after understanding the physics of producing high beta plasmas can one develop a relevant theory or connect current theories to experimental data. The understanding and confirmation of such theories are essential to reproducing high beta plasmas, not only in our experiment, but also in a scaled up version of LDX.

Another key question LDX is purposed to explore is the plasma confinement properties in a magnetic dipole. Specifically, we want to learn about the formation and evolution of convective cells that may arise in this kind of plasma. Convective cells are global convective motions of particles caused by exceeding the MHD stability limit. It is of great interest to study how convective cells affect the energy and particle transport. If convective cells only transport particles and not energy, it would be of great consequence to solving the fueling and ash removal problems in a future reactor. Because LDX plasmas are quasi-steady state (limited only by the RF source), we would also like to study their long term evolution. This issue is related to the first question; can we sustain a quiescent high-beta plasma for an indefinite time without causing disruptions or otherwise violent instabilities? The longest shots we have had so far were on the order of ten seconds, and we have been successful in sustaining a high-beta 20% plasma for this length of time. The next obvious step would be to lengthen our shots to demonstrate the true quasi-steadiness of our plasma.

In reaching the objectives of the experiment, LDX will be operated in three distinct phases. Phase one is the current phase in which the dipole is supported during operation. Although there are only three thin supports, they are enough to cause end losses that limit the beta of the plasma. Plasma formation and profile control

by multi-frequency electron cyclotron resonance heating is being explored in this phase. The measurement of beta and instabilities that limit it is crucial at this stage. The next phase is the levitated dipole phase. The mechanical supports will be gone, and the dipole will be supported by the levitation coil. The eradication of the supports will eliminate end losses, and pitch angle scattered particles will survive, leading to the attainment of higher beta. True confinement studies can be done in this phase since most of the energy losses can be attributed to classical diffusion and bremmstrahlung. In these first two phases of operation, there will be two marginally interacting populations of electrons– hot and cold. The hot electrons are produced by ECRH, and they eventually become cold electrons through collisions. However, during ECRH there always will be a population of hot electrons that have not had the time to cool down; in other words, the characteristic time of the creation of hot electrons is much shorter than that of them cooling down through collisions. Hence, the distribution function of electrons is never a maxwellian during the initial two phases. The final phase of operation is intended to produce a maxwellian population of electrons through gas puffs and pellet injections.

1.5 Thesis Goals

The purpose of this thesis is to answer and resolve some of the questions and issues broached in the previous section. Of course, it is not the intent and would be inappropriate to cover the broad range of questions related to LDX as a whole in a single thesis. Accordingly, this work focuses on the key results obtained from the magnetic diagnostics that help elucidate the physics of LDX. The magnetic diagnostics alone provide enough data to answer some of the most important questions about LDX that need to be answered in its first phase of operation.

The outline of the thesis goes as follows: Ch. 2 introduces and discusses the different types of magnetic diagnostics on LDX, Ch. 3 examines the mathematical procedure used to optimize the sensor locations, Ch. 4 is devoted to error analysis, equilibrium and stability of LDX are studied in Ch. 5, and the characteristics of

reconstructing LDX plasmas are explained in Ch. 6. Chapters 7-9 deal with the interpretation of the magnetic data obtained from measuring LDX plasmas under various experimental conditions. The main points of the thesis are summarized and recommendations for future work are given in Ch. 10.

Amongst other notable achievements in the thesis, the two that clearly stand out as most important are the measurement of high beta and the measurement of supercritical pressure profiles. These two measurements are momentous not only because they prove that LDX can do what it was designed to do, but also because they show how MHD applies (or not apply) to LDX in a favorable way. It is generally understood that the assumptions of MHD rarely, if ever, conform with the parameters of a given plasma experiment. However, it often is the case that despite its fallacious assumptions, MHD predictions prevail. MHD predictions usually give the worst case scenarios and hence are inconvenient for the experimenters. Ironically in LDX, the pressure gradient routinely exceeds the MHD limit. Although the pressure in LDX plasmas is dominated by the contribution from the hot electrons that clearly violate the MHD assumptions, the fact that it is not somehow bound by the MHD limit is noteworthy. It is important to point out that the ability of LDX plasmas to attain high betas does not depend on them exceeding the MHD gradient limit. Of course, the steeper the pressure gradient can get, the higher the peak beta can be for a given edge pressure. But the marginal gradient is still very steep, and large peak betas can still be attained if there is sufficient edge pressure. In other words, MHD does not inherently limit the peak beta; MHD limits the pressure gradient, which can affect the peak beta. Hence, we can expect to achieve high betas even in the third phase of the experiment, in which all the electrons are thermalized.

Chapter 2

Magnetic Diagnostics

One of the most important and basic diagnostics that LDX has is magnetic diagnostics. The magnetic sensors are integral to achieving one of the goals of the experiment; they allow us to deduce the pressure and beta profiles of the plasma, if not alone then in conjunction with other diagnostics. Without magnetic sensors, it would be very difficult to measure the beta of the plasma and hence gauge the performance of the machine in attaining its goals.

The importance of the determination of the pressure profile extends well beyond finding the peak beta. The pressure profile measurement is crucial to understanding the nature of the instability that is most expected to occur in the dipole configuration. Specifically, MHD pressure driven instabilities such as interchange and ballooning modes depend on the steepness of the pressure profile, and we need to be able to measure the marginal (maximum) pressure gradient we can have without exciting them. With different magnetic sensors working synchronically, it is possible to capture the maximum equilibrium pressure gradient the plasma can support and the structure and dynamics of subsequent instabilities caused by exceeding the limit. In the first phase of operation, however, we will not expect the stability property of the plasma to be limited by the pressure gradient since most of the pressure is carried by the hot electrons that do not adhere to the MHD stability theory. Instead, the hot electrons are subject to a kinetic analog of the MHD interchange instability called the hot electron interchange instability (HEI). The HEI is dependent on the

density gradient and the ratio of the hot electrons to cold electrons rather than on the pressure gradient. Although the measurement of the pressure profile is less important to characterizing the HEI than to characterizing MHD pressure driven modes, it is nevertheless of great interest to know how much pressure gradient (beyond the MHD marginal gradient) the hot electrons can sustain.

Another notable role that magnetic diagnostics play is in the determination of the plasma shape and size. MHD theory predicts that the pressure profile of the LDX plasma is a strong function of its shape and size. This is a result of the fact that the LDX plasma is stabilized by plasma compressibility (as will be discussed in Ch. 5). It goes without saying that simultaneous determination of the plasma shape, size, and pressure profile is needed to test the compressibility theory. LDX will be operated with different internal and external magnetic configurations, and it is of great interest to learn how the plasma shape and size change as the currents in the different magnets are varied. For example, in going from phase one of operation to phase two, the L-coil will be activated and its field is predicted to change how the plasma is limited at the edge, potentially altering the confinement properties. Another example is the use of the Helmholtz coils to abruptly change the size of the plasma to test for compressibility. These are just a few examples of why it is so vital to know what the plasma looks like in the vacuum chamber.

As its name implies, a magnetic diagnostic is a sensor that measures magnetic fields. Some sensors measure the time rate of change of the field while others measure the absolute field. The field that these sensors measure is a combination of the field from the magnets on (or floating within) the machine and that from plasma current. Knowing the plasma current profile allows for determining the plasma pressure profile through a mathematical process known as reconstruction. This process will be discussed in detail in Ch. 6.

2.1 Magnetic Diagnostics on LDX

LDX is equipped with multifarious magnetic sensors. Most of the sensors are located outside of the vacuum vessel (as opposed to inside) for several reasons. The most obvious reason is for simplicity in their construction and installation. If a sensor were to go inside the vessel, it would need to be constructed of high vacuum compatible materials that could withstand sufficient heat flux from the plasma. Even if they meet these requirements, it is generally bad practice to expose them directly to the plasma and some kind of metal shielding is usually required. Another reason for putting the sensors outside is to minimize their effect on the plasma. A solid object in the plasma inevitably perturbs or limits it, hence changing the very property of the entity that is being measured. The final reason the sensors are placed outside is because they simply do not have to go inside. In saying this, we need to consider what effect the vacuum vessel has on the magnetic measurements.

A change in the magnetic field propagates as an electromagnetic wave at the speed of light in a given medium. If the change is produced in the vacuum vessel, this information has to travel through the vessel wall to reach an external sensor. Depending on the characteristic time (or frequency) of the changing field, the EM wave will be attenuated when it travels through a conductive medium such as the vessel wall. This attenuation is exponential for a plane wave and can be calculated in a straight-forward manner. The result is usually written as the skin depth, or the distance the wave has to travel in the material to become attenuated by a factor of e,

$$\delta_{skin} = \sqrt{\frac{2}{\omega \mu_0 \sigma}} \ . \tag{2.1}$$

Assuming that an e-fold attenuation can be tolerated, the equation can be rewritten to find the maximum frequency a given wall will transmit,

$$f_{max} = \frac{1}{\pi \mu_0 \sigma d^2} \ , \tag{2.2}$$

where d is the wall thickness.

The LDX vessel wall has a thickness of 3/4" and is made of type 302 stainless steel. Plugging in the appropriate physical parameters, it is expected that the vessel

will significantly attenuate EM frequencies above 500 Hz. Frequencies below 500 Hz are not necessarily safe since there is another frequency limit below f_{max} that is associated with the mode size and given by [18],

$$f_{limit} = \frac{1}{\mu_0 \sigma L w} \ , \tag{2.3}$$

where w is the wall thickness and L is the characteristic size of the mode. A large mode in LDX may be on the order of a meter, and this would give a frequency limit of 30 Hz. A typical shot on LDX lasts for multiple seconds, so the frequencies associated with equilibrium measurements are much lower than 500 Hz and sufficiently lower than 30 Hz. This means that all magnetic sensors associated with equilibrium measurements can be placed outside the vacuum chamber without losing pertinent information. On the other hand, magnetic fluctuations of the plasma are typically of much higher frequency than 500 Hz, and it is imperative that the sensors that detect them go inside the vessel. For example, a typical MHD fluctuation has a characteristic frequency that goes like the Alfven speed divided by the characteristic length $\omega_{MHD} \sim \frac{v_A}{L}$. Taking $B \sim 1$ T, $n \sim 10^{17}$ m^{-3}, and $L \sim 1$ m (order of magnitude of the machine dimension), we get ω_{MHD} of more than 10 MHz. If the fluctuation sensors are placed outside the vessel, there is absolutely no chance they will detect these fast activities. For this simple reason, all fluctuation measuring detectors have been placed inside the vacuum chamber and made from vacuum compatible and heat resistant materials.

2.1.1 Sensors for Equilibrium Measurement

There are three main types of magnetic sensors that measure the equilibrium fields and fluxes. Poloidal field (B_p) coils and flux loops depend on Faraday's Law for their utility whereas Hall probes take advantage of the Hall effect. Because these diagnostics are placed outside the vessel wall, they are relatively simple to build and install.

Poloidal field coils are designed to measure the boundary magnetic fields of LDX plasma. The field in LDX is only in the poloidal direction, so these coils are oriented

and named accordingly. As the name implies, these sensors are basically coils of thin wire wound around a solid mandrel. Faraday's Law says that a time rate of change of field ($\frac{dB}{dt}$) produces a voltage at the ends of a coil,

$$V = NA\frac{dB}{dt} \ , \tag{2.4}$$

where N is the number of turns and A is the cross-sectional area.

Since the quantity of interest is the ΔB produced by the plasma current, the output voltage from a coil must be integrated over the time of plasma existence. For this purpose, the outputs of all the coils are connected to analog integrator circuits that have been specifically developed for Alcator C-Mod magnetic diagnostics. The integrator circuits integrate the input voltage (output from a coil) over time and divide the result by their respective RC time constants [27],

$$V_{out} = \frac{1}{RC}\int_{t_1}^{t_2} V_{in}dt \ , \tag{2.5}$$

where the integration starts at t_1 and ends at t_2.

Substituting in the output voltage from a coil for V_{in}, we get,

$$V_{out} = \frac{NA}{\tau}\Delta B \qquad (\tau \equiv RC) \ . \tag{2.6}$$

Experimentally, it is ideal to get an output voltage on the order of a few volts for a typically expected ΔB of LDX plasma. Through simulated equilibrium reconstructions with reasonable plasma parameters, it has been found that a typical ΔB at the vessel wall is on the order of 10 G. Setting the ideal output voltage to be $\sim$ 5 V, a requirement is imposed on the quantity $\frac{NA}{\tau}$. Furthermore, all integrators are prone to drift more with decreasing time constant, so τ should be kept above 1 ms to avoid signal adulteration by wild drifts. With this additional constraint, the required condition becomes $NA > 5$ m^2. The question now is to choose the appropriate number of turns and area to meet this condition. It is easy to see that increasing A entails compromising the spatial resolution of the coil, so it may seem logical to minimize the area and make enough turns as necessary. This is true as long as the $\frac{L}{R_0}$ time (where R_0 is the sum of the resistance of the coil, resistance of the transmission line, and the

integrator input impedance) is kept significantly shorter than the characteristic time of equilibrium measurement. In lieu of the fact that the vessel wall cannot transmit any signal much faster than 500 Hz, it is more than sufficient to keep $\frac{L}{R_0} < 2$ ms.

With all this in consideration, the B_p coils for LDX have been designed to have $N = 1000$ and $A = 50$ cm^2 giving a total effective area $NA = 5$ m^2 (Figure 2-1). Using a 30 AWG magnet wire wrapped around a cylindrical G-10 mandrel of 8 cm diameter and 15 cm length, the calculated inductance of the coils comes to about 34 mH. The integrators built for the coils have an input impedance of 20 kΩ, hence giving an $\frac{L}{R_0}$ time of about 2 μs. The characteristic dimension of the coils is about 10 cm, which is small compared to the size of the machine or the characteristic length of the plasma field gradient $|\frac{B}{\nabla B}|$. It therefore can be concluded that the designed coil geometry meets the requirements of the given constraints.

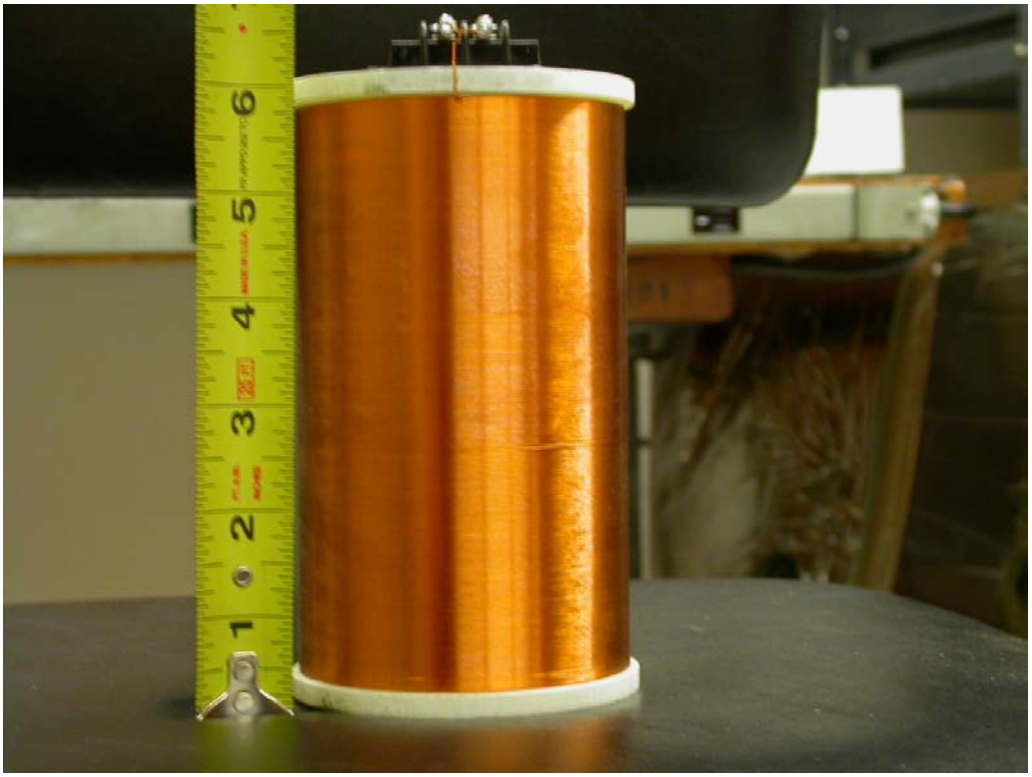

Figure 2-1: A poloidal field coil.

Flux loops are another set of sensors that measure an equilibrium quantity. As

the name implies, they are basically loops of wire that measure the equilibrium flux. These sensors are topologically equivalent to B_p coils, the only difference being that the mandrel of the loops is the vacuum vessel itself. Just like for the B_p coils, flux loop signals are derived from Faraday's Law and must be integrated to get the equilibrium flux. The calculation to obtain the integrated output voltage for these loops is exactly the same as was done for the B_p coils (with the substitution $NAB \rightarrow \psi$) and will not be replicated. The result is,

$$V_{out} = \frac{\Delta\psi}{\tau} \ . \tag{2.7}$$

Notice that the number of turns has been constrained to one (as is for a typical flux loop), but this need not be the case. If after calculating a typical $\Delta\psi$ at the vessel wall and finding that the signal is too weak, more turns can be added as needed. Simulated equilibrium reconstructions showed that a typical $\Delta\psi$ at the wall is on the order of 10 mWb. Setting the integrator time constant to be 1 ms, this gives an integrated output voltage of about 10 V, which is more than what is needed. It was consequently determined that a single turn would be enough for all the flux loops (Figure 2-2).

Figure 2-2: Flux loops at the bottom of the vessel.

The final set of equilibrium magnetic diagnostics is the Hall probes. Hall probes are basically solid-state devices that depend on the Hall effect to output a voltage to an applied magnetic field. The advantage of having these sensors is that they can measure the steady-state field rather than the transient field, and hence their signals do not have to be electronically integrated. It seems like Hall probes can replace B_p coils as sensors for the poloidal field measurement, but it is hard to find Hall sensors that are sensitive enough and can work within the specified field range. One major characteristic of Hall sensors is that they have a specified field range of linearity. Once the measured field falls out of this range, the probe either saturates or its sensitivity becomes a function of the field, both of which make the voltage readout meaningless or hard to interpret. Given the size of a Hall probe, its valid output voltage range is usually fixed, so there is a compromise between the sensitivity and the field range of linearity; the more sensitive the probe is, the narrower its field range of linearity is. Since the valid output voltage range can be widened by increasing the probe size, the ultimate competition is between spatial resolution, field resolution, and the measurable field range.

The steady-state field at the vessel wall is typically on the order of 100 G, so the desired probes will have a field range of linearity on the order of a few hundred gauss. The probe with the maximum sensitivity with the given range of linearity in the commercial market was found to be Model A3515 from Allegro Microsystems (Figure 2-3). This model probe features a range of linearity of +/- 500 G and sensitivity of 5 mV/G. Because the quiescent output voltage and sensitivity are functions of the input power voltage, the input voltage must be continuously monitored to get the correct field value from the output. In addition, the quiescent voltage and sensitivity at the nominal input voltage of 5 V must be calibrated for each sensor since these values will be slightly different from one sensor to another. The measured field can be written in terms of the output and input voltages as follows:

$$B = \frac{V_0 - V_{OQ(VCC)}}{Sens_{(VCC)}} \tag{2.8}$$

$$= \frac{1}{\beta}\left(\frac{V_0}{V_{CC}} - \alpha\right) . \tag{2.9}$$

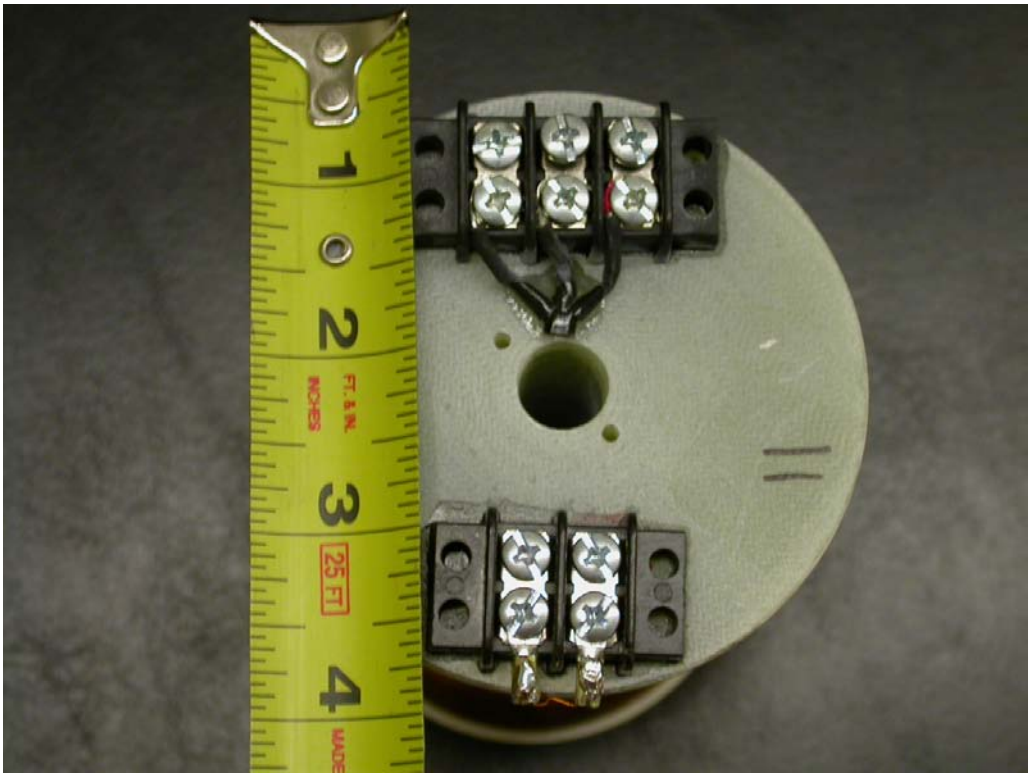

Figure 2-3: A Hall-probe attached to the top of a B_p coil.

In the above, V_0 is the output voltage, V_{CC} is the input voltage, and $V_{OQ(VCC)}$ and $Sens_{(VCC)}$ are the quiescent output voltage and sensitivity, respectively, when the input voltage is V_{CC}. The parameters α and β are to be calibrated using the following ratiometric relations:

$$\alpha \equiv \frac{V_{OQ(5V)}}{5V} = \frac{V_{OQ(VCC)}}{V_{CC}} \tag{2.10}$$

$$\beta \equiv \frac{Sens_{(5V)}}{5V} = \frac{Sens_{(VCC)}}{V_{CC}} \ . \tag{2.11}$$

Hence, α and β can be deduced by measuring the quiescent output voltage and sensitivity at a given input voltage V_{CC}. In actuality, the sensitivity and quiescent output voltage are also functions of the ambient temperature, but the effect is very small for the ambient temperature range we expect in the experimental cell. The details of the calibration procedure will be discussed in the next section.

2.1.2 Sensors for Fluctuation Measurement

The only set of magnetic sensors used for fluctuation measurements is Mirnov coils. Mirnov coils are structurally identical to B_p coils, but there are some important differences. As stated earlier, these sensors must go inside the vessel, so they need to be made of appropriate materials. Also, the coils must be sufficiently small to minimize their effect on the plasma. Although the physical principle of operation of Mirnov coils is the same as that of B_p coils (i.e. Faraday's Law), Mirnov signals are not integrated and only amplified to preserve all the details of the fluctuations. As such, an output from a Mirnov coil retains the time derivative factor,

$$V = GNA\frac{dB}{dt} \ , \tag{2.12}$$

where N is the number of turns, A is the cross-sectional area, and G is the amplifier gain.

Again, the goal is to design the coils to give an output on the order of a few volts under typical plasma conditions. Unfortunately, an equilibrium reconstruction program cannot predict the levels of magnetic fluctuations that can occur since fluctuations are inherently transient events. However, data from another dipole confinement

experiment at Columbia called the Collisionless Terrella Experiment (CTX) helped to estimate the expected fluctuation levels to be on the order of 100 μG/μs. Hence, GNA must be on the order of 100. The effective area NA should be maximized without making the probes too large or sacrificing their time resolution to maximize their sensitivity. The recurring theme of the competition between the various merits of the probes is once again apparent [28].

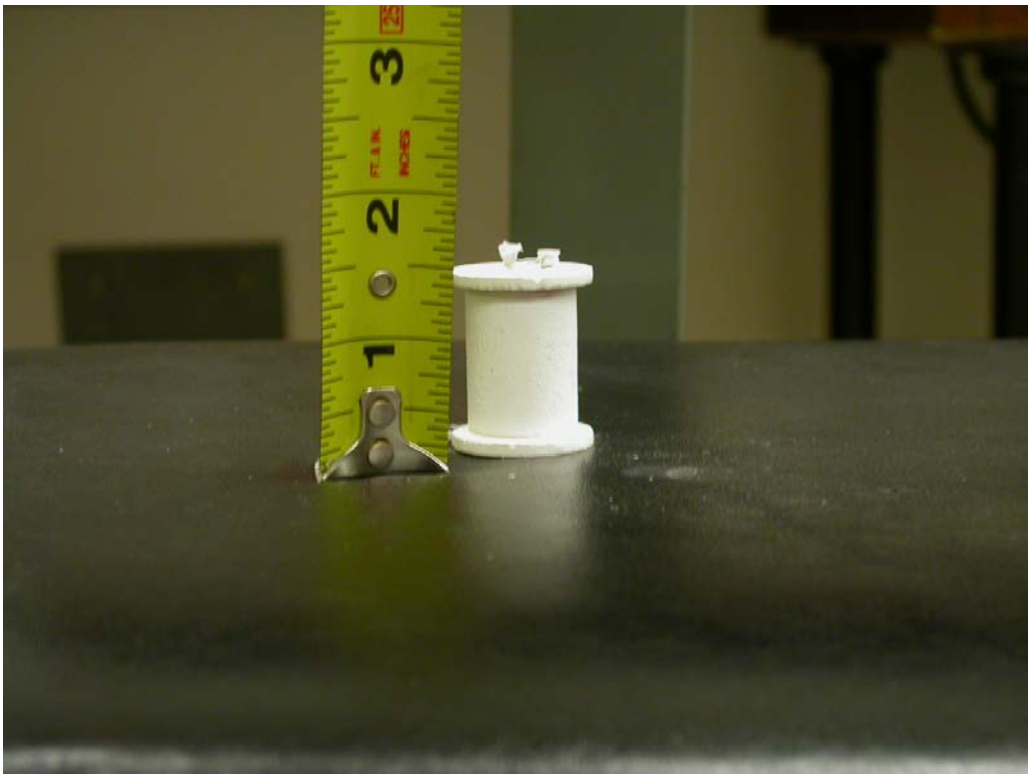

Figure 2-4: A Mirnov coil.

Without further analysis, the Mirnov coils have been designed with $N = 200$ and $A = 3$ cm^2 giving $NA = 0.06$ m^2 (Figure 2-4). The coil mandrels are made of boron nitride, which is both heat resistant and vacuum compatible, with 1.9 cm (0.75") diameter and 3.4 cm (1 1/3") length. The same 30 AWG magnet wire is used as the conductor, but its surface is coated with heat resistant boron nitride spray to protect the insulation coating. These coils are connected to dual stage amplifier boards (also from C-Mod) with the gains set at around 1600 to give $\sim$ 1 V level signals. The

calculated inductance of the coils is about 400 μH, and the corresponding $\frac{L}{R_0}$ time is 200 ps when connected to the amplifiers with a 2 MΩ input impedance. Of course, 200 ps is not the actual temporal resolution of the coils when they are wired to the amplifiers through transmission lines, because capacitive effects of the whole system must be considered. Nevertheless, it is enough to ensure that the coil inductance will not be the limiting parameter in their time response. The coils are encased in tiny stainless steel boxes to prevent direct contact with the plasma. This also ensures that they do not pick up unwanted electrical noises on the probe leads. The stainless steel shieldings are thin enough (0.01") that signals slower than 3 MHz are not significantly attenuated. The shielding boxes are also small enough to ensure minimal perturbation of the plasma, but they can still limit the plasma at a maximum of 1" from the wall. This is not expected to have much impact on the characteristics of the plasma.

2.2 Calibration of the Electronics and Diagnostics

2.2.1 Electronics Calibration

The integrator and amplifier boards have been tested and calibrated using a standard signal generator and an oscilloscope. The parameter to be calibrated in both of these electronics is their gain. The amplifier gain is just a unitless multiplicative factor, but the integrator gain is the reciprocal of its RC time constant. Although the right resistance and capacitance (only for the integrators) values have been selected to produce the desired gain, the resistors and capacitors have a tolerance of 1 % and 10 %, respectively, and hence it is good practice to calibrate the gain using a known input signal.

A 60 Hz sinusoidal signal is used as the input to measure the gain of the integrators and amplifiers. Both the integrators and amplifiers output an amplified sinusoid at the same frequency. Notice that the integral of a sinusoid is a phase shifted sinusoid attenuated by its angular frequency. The integrators therefore output a sinusoid that is amplified by a factor of $\frac{1}{\omega\tau}$. The time constant can be found by inverting

the product of the angular frequency and the amplification factor. The gain of an amplifier channel is simply its amplification factor. The calibration data for the integrators and amplifiers is summarized in Table 2.1.

2.2.2 Diagnostics Calibration

Every magnetic diagnostic has been calibrated with a pair of Helmholtz coils. These coils are different from and much smaller than the H-coils on the machine. The radius of the coils is 30.5 cm, and each has 100 turns. It is straightforward to calculate the field at the center of the pair for a given current and goes as follows:

$$B[G] = 2.95I[A] \ . \tag{2.13}$$

To measure the NA values of the B_p and Mirnov coils, one only needs to measure the RMS output voltage from the coils and the RMS of the time derivative of the imposed field as calculated from the RMS current in the Helmholtz coils,

$$\begin{aligned} B &= B_0 \sin(\omega t) && (2.14)\\ \frac{dB}{dt} &= \omega B_0 \cos(\omega t) && (2.15)\\ \left.\frac{dB}{dt}\right|_{RMS} &= \omega B_{RMS} = 2\pi f B_{RMS} \ . && (2.16) \end{aligned}$$

Therefore,

$$\begin{aligned} V^{out} &= NA\frac{dB}{dt} && (2.17)\\ NA &= \frac{V^{out}_{RMS}}{\left.\frac{dB}{dt}\right|_{RMS}} = \frac{V^{out}_{RMS}}{2\pi f B_{RMS}} \ . && (2.18) \end{aligned}$$

The B_p and Mirnov coils have been calibrated at 500 Hz at 3 G and 980 Hz at 2 G, respectively. Because Mirnov coils have a small NA, the product fB_{RMS} was maximized for their calibration to get the maximum possible signal.

Hall probe calibration requires finding two independent parameters, α and β, that have already been defined. Finding α is a simple matter of measuring the quiescent output voltage (output voltage at zero field) at a given input power voltage. Finding β involves measuring the output voltage at at least one field. The can be done with

I.D. #	Amp Gain	Gain S.D.	Int. Time (s)	Time S.D. (s)
1A	2.06	0.001	0.000996	0.000003
1B	2.06	0.001	0.000999	0.000011
1C	2.06	0.002	0.00100	0.00001
1D	2.06	0.001	0.00101	0.00001
2A	2.06	0.002	0.0009750	0.0000092
2B	2.06	0.001	0.00103	0.00001
2C	2.06	0.002	0.0009861	0.0000086
2D	2.06	0.002	0.00102	0.00001
3A	2.06	0.002	0.0009858	0.0000078
3B	2.06	0.001	0.00102	0.00001
3C	2.06	0.001	0.00102	0.00001
3D	2.06	0.003	0.000992	0.000007
4A	2.06	0.001	0.00103	0.00001
4B	2.06	0.0004	0.000990	0.000013
4C	2.06	0.0004	0.0009896	0.0000072
4D	2.06	0.002	0.0009791	0.0000068
5A	2.06	0.002	0.0009928	0.0000060
5B	2.06	0.001	0.0009780	0.0000045
5C	1592	12	0.00103	0.00001
5D	1563	63	0.00100	0.00001
6A	1573	28	0.0009897	0.0000068
6B	1573	28	0.00103	0.00001
6C	1583	32	0.00102	0.00001
6D	1596	1	0.00100	0.00001
7A			0.000983	0.000032
7B	1582	9	0.00101	0.00002
7C	1610	32	0.00103	0.00001
7D	0.103		0.00101	0.00002

Table 2.1: Calibration data for amplifier and integrator boards.

either AC or DC, but using an AC field is a bit easier since it does not require the measurement of the quiescent voltage (i.e. AC quiescent voltage is zero). With these measurements, α and β can easily be calculated through their definitions.

The β parameters have been calibrated at both 500 Hz at 3 G and 20 Hz at 9 G. Although only a single field measurement is necessary to find β, the two field measurement allows to check for linearity, albeit in the small field range. The specced bandwidth of the probes is 30 kHz, so measuring the sensitivity at the two frequencies should not be an issue.

Lastly, since the output voltage from the flux loops depends only on the measured flux and the integrator time constant, there is no calibration associated with the loops themselves.

The diagnostics calibration results are shown in Tables 2.2 and 2.3.

2.3 Future Improvements to the Magnetic Diagnostics System

A lot has been accomplished in the development and installation of the magnetic diagnostics on LDX. Needless to say, there are certain improvements and additions that would doubtlessly further their utility. This section deals with some suggested improvements to the magnetic diagnostics that can possibly be undertaken by a fortunate student who may happen to adopt them for his / her thesis work.

The B_p coils and flux loops are connected to integrator circuits that suffer from signal drifts. The drift is aggravated as their gains increase. Currently, the gains are set to a level that gives a typical output voltage of a less than a volt for typical plasma shots. Ideally, we want to have an output voltage between 1 V and 10 V to fully take advantage of the bit resolution of the digitizer. The integrator circuits currently in use are of a relatively rudimentary design, and more sophisticated circuits could possibly be used to ameliorate the drift. A typical LDX shot today is on the order of ten seconds, but we may want to study much longer shots in the future.

I.D. #	$B_p\ NA$ (m^2)	NA S.D. (m^2)	α	α S.D.	β (G^{-1})	β S.D. (G^{-1})
1N	5.22	0.04	0.5014	0.0004	0.0011	0.00003
1P	5.45	0.02	0.5005	0.0017	0.0011	0.0001
2N	5.06	0.01	0.5035	0.0003	0.0010	0.00005
2P	4.92	0.004	0.5153	0.0005	0.0010	0.00001
3N	5.07	0.003	0.5028	0.0005	0.0011	0.00003
3P	5.01	0.02	0.5012	0.0004	0.0011	0.0001
4N	5.07	0.003	0.5046	0.0001	0.0011	0.00005
4P	5.24	0.01	0.5020	0.0001	0.0012	0.0001
5N	5.21	0.02	0.5138	0.00003	0.0010	0.0001
5P	5.20	0.02	0.5159	0.0004	0.0010	0.00004
6N	5.22	0.002	0.5041	0.0003	0.0011	0.00003
6P	5.26	0.001	0.5019	0.0004	0.0011	0.00003
7N	5.07	0.005	0.5057	0.0004	0.0010	0.00005
7P	4.98	0.004	0.5099	0.0003	0.0011	0.0001
8N	5.21	0.01	0.5078	0.0003	0.0010	0.00001
8P	5.31	0.01	0.5060	0.0003	0.0010	0.0001
9N	5.32	0.01	0.5048	0.0010	0.0011	0.0001
9P	4.99	0.004	0.5055	0.0002	0.0011	0.0001

Table 2.2: Calibration data of B_p coils and Hall probes.

I.D. #	Mirnov NA (m^2)	NA S.D. (m^2)
1	0.046	0.001
2	0.059	0.002
3	0.054	0.002
4	0.057	0.003
5	0.056	0.003
6	0.057	0.002
7	0.061	0.002
8	0.056	0.001
9	0.064	0.002

Table 2.3: Calibration data of Mirnov coils.

After all, one of the selling points of LDX is its steady-state operation, and it is only natural that we want to study the equilibrium on a long time scale, perhaps on the order of minutes. The current integrators are definitely not capable of integrating for such a long time, and it would become mandatory to eradicate the drift if we want to study long plasma shots.

Another improvement that would be helpful is to reduce the noise on the Hall probe signals. Despite the Hall probes having their own preamplifiers mounted onto the chip, there is substantial noise in their signals by the time they reach the digitizer. It may be the way the power is fed to these chips or it may just be the way the wiring is done, but a cleaner Hall probe signal would be beneficial in complementing the signals obtained from the B_p coils. The noise in the Hall probe signals currently prevents us from using them to measure the plasma current; instead, they are solely used to measure the floating coil current, which is 1000 times greater than a typical diamagnetic current. Because the Hall probes are actually mounted at the very end of the B_p coils, they can give us field measurements at additional, albeit proximal, locations, providing more constraints to the pressure profile parameters.

Finally, the current set of Mirnov coils can be upgraded in several ways. One of the

chief concerns of the current system is the sensitivity to electrostatic noise. Although the coils are well shielded, they may still be susceptible to high frequency noise that can creep through the small openings. One remedy would be to completely rebuild the coils to incorporate a center tap. This would preferentially block all electrostatic signals while maintaining the magnetic signals. Another possible improvement would be in the wiring of the transmission line and modifying the amplifier circuit. The current system suffers from a low frequency roll-off that prevents us from measuring the details of the evolution of high frequency signals (Figure 2-5). It may be good to incorporate some or all of these improvements before we enter the third phase of the experiment, in which the plasma is thermalized to study Maxwellian plasmas that are susceptible to MHD modes.

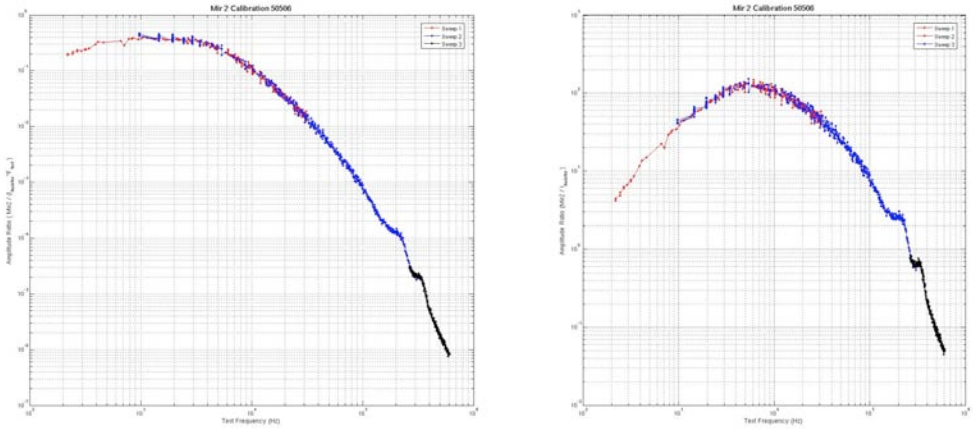

(a) (b)

Figure 2-5: (a) The transfer function (to within a multiplicative factor) of a Mirnov coil as installed and (b) the transfer function multiplied by frequency.

Chapter 3

Sensor location optimization

In conducting any kind of diagnostic measurements, an important question must be answered. Where should the sensors be placed? The answer to the question may depend on several factors, including available space, vacuum and plasma compatibility, ease of access, and sensitivity. Since the LDX magnetic diagnostics for equilibrium measurements are placed outside the vacuum vessel where space and ease of access are not an issue, the real question boils down to where the sensors should be placed to maximize their sensitivities to various plasma parameters. There are various ways to address this question, and a particularly simple method that has been used to choose the sensor positions in LDX will be discussed in this chapter.

3.1 Mathematical formulation

The optimization method presented here is inspired by B. J. Braams' work on function parametrization [3] and is based on the establishment of a functional relationship between measurements from different sensors at different locations and plasma parameters,

$$\boldsymbol{m} = \boldsymbol{F}(\boldsymbol{p}) \ , \tag{3.1}$$

where

> $\boldsymbol{m}$ is an m-dimensional vector of different types of measurements
> at different positions.

$\boldsymbol{p}$ is an n-dimensional vector of plasma parameters.

$\boldsymbol{F} : \mathbf{R}^n \to \mathbf{R}^m$ is the response function.

The goal here is to find the response function so that the sensitivity matrix, $(\boldsymbol{\nabla}_p \boldsymbol{F})^T \equiv (\frac{d\boldsymbol{F}}{d\boldsymbol{p}})^T = (\frac{d\boldsymbol{m}}{d\boldsymbol{p}})^T$, can be calculated. Notice that if we Taylor expand the response function about some point $\boldsymbol{p}_0$ in the parameter space, the sensitivity matrix comes out naturally in the first order term,

$$\boldsymbol{F}(\boldsymbol{p}) \approx \boldsymbol{F}(\boldsymbol{p}_0) + (\boldsymbol{\nabla}_p \boldsymbol{F})^T|_{\boldsymbol{p}=\boldsymbol{p}_0} \cdot (\boldsymbol{p} - \boldsymbol{p}_0) \equiv \boldsymbol{k} + \boldsymbol{R} \cdot \boldsymbol{p} \ , \tag{3.2}$$

where all the constant terms have been lumped into $\boldsymbol{k}$, and $\boldsymbol{R} \equiv (\boldsymbol{\nabla}_p \boldsymbol{F})^T|_{\boldsymbol{p}=\boldsymbol{p}_0}$. The sensitivity matrix $\boldsymbol{R}$ has elements of the form $\frac{\partial m_i}{\partial p_j}$ that give the sensitivities of measurements i to parameters j.

Because the sensitivity matrix has $m \times n$ independent elements and the constant vector has m independent components, we need to have $m(n+1)$ independent equations to specify them. By running the equilibrium code with $\boldsymbol{p}$ as the input and $\boldsymbol{m}$ as the output, we can produce m independent equations in the elements and components. Therefore, we need $n+1$ different equilibria to produce $n+1$ pairs ($\boldsymbol{m}$, $\boldsymbol{p}$) and $m(n+1)$ independent equations. In other words, we need $n+1$ equilibria to completely determine $\boldsymbol{R}$. It may be instructive to look at this problem from a mathematical perspective. The Taylor expansion of the response function $\boldsymbol{F}$ and keeping up to the first order term is equivalent to approximating the m hypersurfaces of $\boldsymbol{F}$ by m hyperplanes whose linear coefficients are rows of $\boldsymbol{R}$ in m $(n+1)$-dimensional spaces. Specifying the hyperplanes for a mapping from n dimensions to m dimensions requires knowing $n+1$ points on them, because if we know one point on the hyperplanes, we also need to know the derivatives in each of the n directions to completely specify them. This is precisely the reason we need to compute $n+1$ equilibria to find $\boldsymbol{R}$ (and $\boldsymbol{k}$).

There are two important points to be extracted from the mathematical picture given above. The first is that the $n+1$ equilibria needed to compute $\boldsymbol{R}$ must not

be too far apart in the parameter space. Mathematically, $||\boldsymbol{p}^i - \boldsymbol{p}^j|| < \epsilon \ \forall \ i, j \in 1, 2, 3, ..., n+1$. The value of ϵ depends on various factors, such as the values of higher derivatives of $\boldsymbol{F}$ at the expansion point, but it usually suffices to keep it as small as practically possible. The proximity condition of equilibrium points basically says that the points used to define hyperplanes that are approximations to the hypersurfaces at $\boldsymbol{p}_0$ must be close to $\boldsymbol{p}_0$. Otherwise, the hyperplanes would not be good approximations to the hypersurfaces at $\boldsymbol{p}_0$. A corollary to this is that hyperplanes are good approximations to the hypersurfaces if we are concerned with points in small neighborhoods of $\boldsymbol{p}_0$. The message here is that the sensitivity matrix $\boldsymbol{R}$ calculated about a point $\boldsymbol{p}_0$ is valid only in a small neighborhood of the point. We therefore need to calculate many sensitivity matrices corresponding to different regions in the parameter space. In other words, we are approximating the response function with many different sensitivity matrices (plus constant vectors) in a piecewise linear fashion. The second point to be understood is that the $n+1$ points needed to define $\boldsymbol{R}$ in a particular region in the parameter space must reflect deviations in all the n directions from a given point on the hyperplanes. After all, it would not be possible to define a hyperplane without knowing its derivatives in all the directions. The $n+1$ points must be wisely chosen to ensure that the necessary information is contained in them.

3.2 Application to LDX Magnetic Diagnostics

Now that the theoretical groundwork has been laid out, we can apply the concept to determine where the magnetic diagnostics should be placed. The strategy goes as follows:

1. Choose x possible locations on the vacuum vessel where the sensors can be placed.

2. Define $\boldsymbol{m}$ by having as its components the measurements of the y different sensors at x different locations. Hence, the dimension of $\boldsymbol{m}$ is $m = xy$.

3. Define $\boldsymbol{p}$ by incorporating the plasma parameters relevant to magnetic reconstruction.

4. Choose z points in the parameter space to obtain z sensitivity matrices.

5. Invoke an averaging scheme over the z sensitivity matrices to evaluate which of the x locations have the highest average sensitivity for each sensor type.

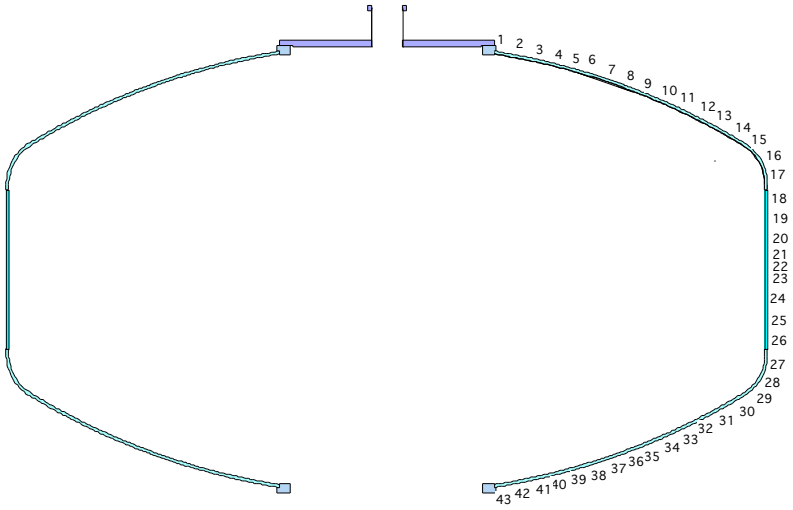

Figure 3-1: Forty-three possible positions to install the sensors.

Forty-three positions have been chosen along the vacuum vessel on a poloidal plane as possible sites for the diagnostics (Figure 3-1). The diagnostics in question are the B_p coils and flux loops. The B_p coils themselves have been divided into two distinct diagnostics depending on whether they are oriented normally or tangentially to the vacuum vessel. With this setup, the dimension of $\boldsymbol{m}$ is 129. The plasma parameters

have been chosen accordingly to the most likely pressure model to be used in the reconstruction process. The pressure model has three free parameters and is of the following form:

$$P(\psi;\psi_{peak},P_{edge},g)=\begin{cases} P_{edge}[\frac{V_{edge}}{V(\psi)}]^g & \text{for } \psi>\psi_{peak} \\ P_{edge}[\frac{V_{edge}}{V(\psi)}]^g \sin^2[\frac{\pi}{2}(\frac{\psi}{\psi_{peak}})^2] & \text{for } \psi<\psi_{peak} \end{cases}, \tag{3.3}$$

where $V \equiv \frac{dVol}{d\psi} = \oint \frac{dl}{B}$ is the differential flux tube volume per differential flux. This and other pressure models will be discussed in more detail in Chapter 6. For now it suffices to understand that the model has the following three free parameters: ψ_{peak} (flux at the pressure peak), P_{edge} (pressure at the plasma edge), and g (the adiabatic parameter that gives the slope of the pressure fall and is equal to $\frac{5}{3}$ in a 3-D collisional gas). The three parameters give three dimensions to $\boldsymbol{p}$. When written out, Eq. 3.2 looks like the following:

$$\begin{bmatrix} m_{BN1} \\ \vdots \\ m_{BN43} \\ m_{BT1} \\ \vdots \\ m_{BT43} \\ m_{\psi 1} \\ \vdots \\ m_{\psi 43} \end{bmatrix} = \begin{bmatrix} k_1 \\ \vdots \\ k_{129} \end{bmatrix} + \begin{bmatrix} \frac{\partial B_{N1}}{\partial P_{edge}} & \frac{\partial B_{N1}}{\partial R_{peak}} & \frac{\partial B_{N1}}{\partial F_{crit}} \\ \vdots & \vdots & \vdots \\ \frac{\partial B_{N43}}{\partial P_{edge}} & \frac{\partial B_{N43}}{\partial R_{peak}} & \frac{\partial B_{N43}}{\partial F_{crit}} \\ \frac{\partial B_{T1}}{\partial P_{edge}} & \frac{\partial B_{T1}}{\partial R_{peak}} & \frac{\partial B_{T1}}{\partial F_{crit}} \\ \vdots & \vdots & \vdots \\ \frac{\partial B_{T43}}{\partial P_{edge}} & \frac{\partial B_{T43}}{\partial R_{peak}} & \frac{\partial B_{T43}}{\partial F_{crit}} \\ \frac{\partial \psi_1}{\partial P_{edge}} & \frac{\partial \psi_1}{\partial R_{peak}} & \frac{\partial \psi_1}{\partial F_{crit}} \\ \vdots & \vdots & \vdots \\ \frac{\partial \psi_{43}}{\partial P_{edge}} & \frac{\partial \psi_{43}}{\partial R_{peak}} & \frac{\partial \psi_{43}}{\partial F_{crit}} \end{bmatrix} \cdot \begin{bmatrix} P_{edge} \\ R_{peak} \\ F_{crit} \end{bmatrix}. \tag{3.4}$$

The parameters ψ_{peak} and g have been replaced by R_{peak} (midplane radius at the pressure peak) and $F_{crit} = \frac{3}{5}g$, respectively, so that their physical meanings are elucidated. Following the specifications of $\boldsymbol{m}$ and $\boldsymbol{p}$, a domain that covers the most likely operational regime of LDX is defined. The domain is a cube in the parameter space constructed as,

$$\begin{array}{lcccl} 0.1 \text{ Pa} & \leq & P_{edge} & \leq & 10.0 \text{ Pa} \\ 0.50 \text{ m} & \leq & R_{peak} & \leq & 0.90 \text{ m} \\ 0.5 & \leq & F_{crit} & \leq & 3.0 \end{array}$$

The cube contains 332 points about which the expansion of the response function is performed. At each point, the sensitivity matrix is found by solving the equations,

$$\boldsymbol{m}^1 = \boldsymbol{k} + \boldsymbol{R} \cdot \boldsymbol{p}^1 \tag{3.5}$$

$$\boldsymbol{m}^2 = \boldsymbol{k} + \boldsymbol{R} \cdot \boldsymbol{p}^2 \tag{3.6}$$

$$\boldsymbol{m}^3 = \boldsymbol{k} + \boldsymbol{R} \cdot \boldsymbol{p}^3 \tag{3.7}$$

$$\boldsymbol{m}^4 = \boldsymbol{k} + \boldsymbol{R} \cdot \boldsymbol{p}^4 \ . \tag{3.8}$$

Notice that because $n = 3$, we need four points in the parameter space (as indicated by the superscripts) to specify $\boldsymbol{R}$. One of the four points is the expansion point. Upon eliminating the constant vector $\boldsymbol{k}$ and concatenating the remaining equations into a single system, we obtain,

$$\begin{bmatrix} \boldsymbol{m}^1 - \boldsymbol{m}^4 \\ \boldsymbol{m}^2 - \boldsymbol{m}^4 \\ \boldsymbol{m}^3 - \boldsymbol{m}^4 \end{bmatrix} = \begin{bmatrix} \boldsymbol{R} & & \\ & \boldsymbol{R} & \\ & & \boldsymbol{R} \end{bmatrix} \cdot \begin{bmatrix} \boldsymbol{p}^1 - \boldsymbol{p}^4 \\ \boldsymbol{p}^2 - \boldsymbol{p}^4 \\ \boldsymbol{p}^3 - \boldsymbol{p}^4 \end{bmatrix} \ . \tag{3.9}$$

This system can be solved for $\boldsymbol{R}$ straightforwardly. Each $\boldsymbol{R}$ orders the 43 locations from best to worst for each diagnostic in terms of its sensitivity to the three parameters. Because we have 332 sensitivity matrices corresponding to 332 different points in the parameter space, we need to invoke an averaging scheme over them to find the best overall positions for each diagnostic.

Rather than performing a numerical averaging, which can be sensitive to outliers, over the 332 sensitivity matrices, a tabulation scheme has been employed here to ensure that the results are not influenced by outliers. The scheme goes as follows:

1. For each $\boldsymbol{R}$, choose 9 locations each with the highest sensitivity to each of the three parameters for each sensor. For example, for the flux loops and given $\boldsymbol{R}$, we would tabulate 9 locations with the highest sensitivity to P_{edge}, 9 locations with the highest sensitivity to R_{peak}, and 9 locations with the highest sensitivity to F_{crit}.

2. After tabulating over all 332 sensitivity matrices, each of the 43 locations will have three numbers associated to it for each sensor type; the first number counts

the number of times the location is chosen for the top 9 sensitivity with respect to P_{edge}, the second counts the number of times it is chosen for the top 9 sensitivity with respect to R_{peak}, and the third counts the number of times it is chosen for the top 9 sensitivity with respect to F_{crit}.

3. The resulting histograms (Figures 3-2, 3-3, 3-4) for each sensor type elucidate its most sensitive locations with respect to the three parameters.

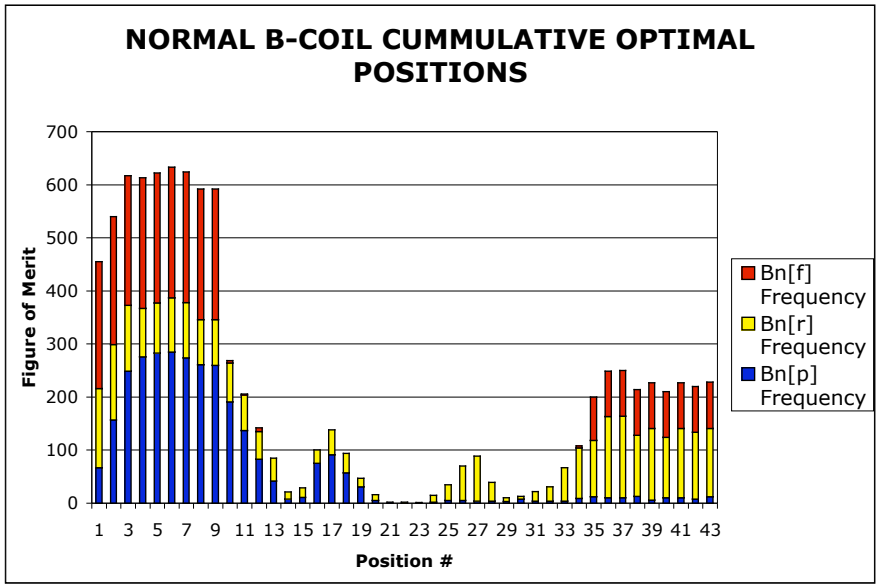

Figure 3-2: A histogram showing the most sensitive positions for normal B_p coils.

Because we are optimizing each sensor type to each of the three parameters without discrimination, it makes sense to place one third of the sensors where the P_{edge} sensitivity is maximized, one third where the R_{peak} sensitivity is maximized, and one

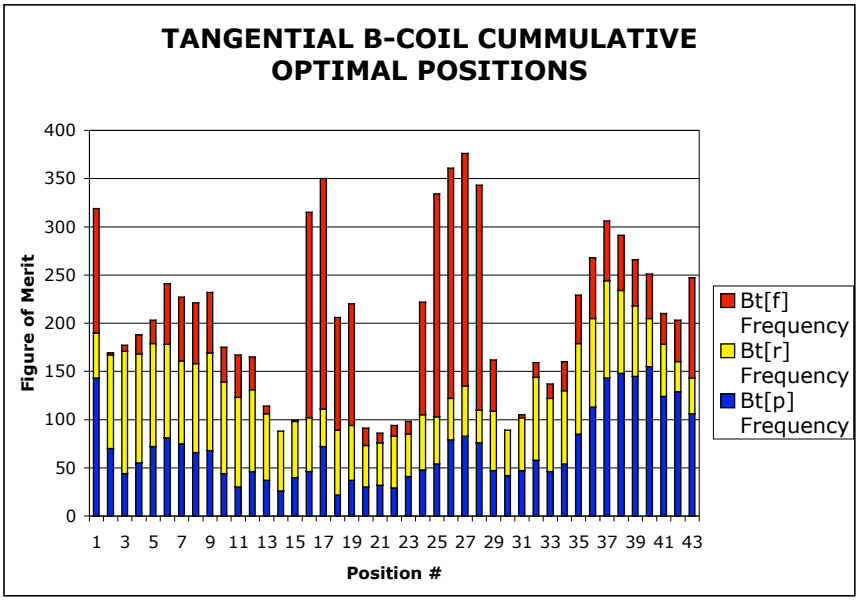

Figure 3-3: A histogram showing the most sensitive positions for tangential B_p coils.

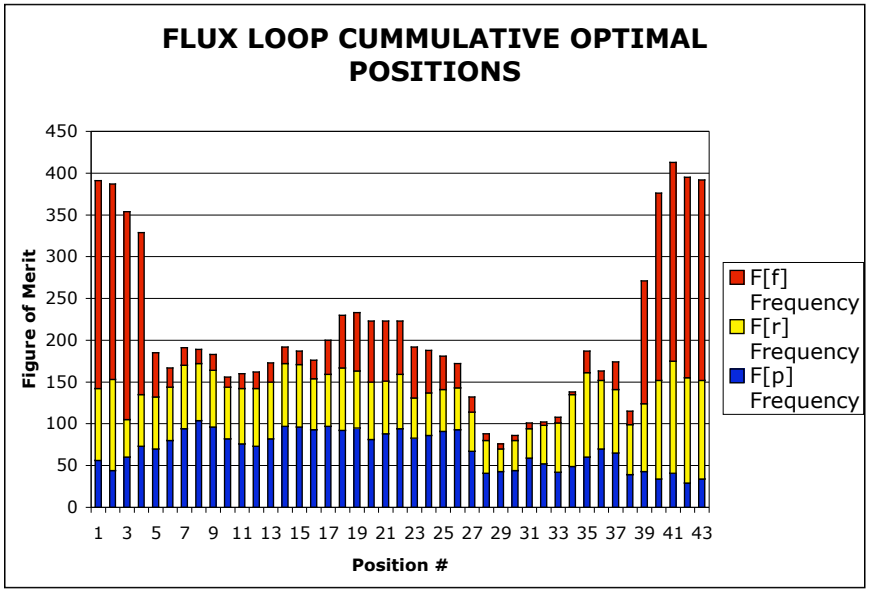

Figure 3-4: A histogram showing the most sensitive positions for flux loops.

third where the F_{crit} sensitivity is maximized. The blue, yellow, and red portions of the above graphs represent the sensitivities of the sensors to these three parameters in respective order. Looking at the graph for normal B_p coils, we should have about five located between positions 1 and 9, one located between positions 16 and 28, and three located between positions 35 and 43. As for tangential B_p coils, we want three located between 1 and 12, one located between 16 and 19, two between 25 and 28, and three between 37 and 42. Finally, we need three flux loops between positions 1 and 4, three between 14 and 26, and three between 39 and 43. The preceding assignment of the different sensors to the said locations adheres to the strategy of giving each parameter an equal opportunity to be sensed. Below is a picture that summarizes the optimal sensor locations (Figure 3-5).

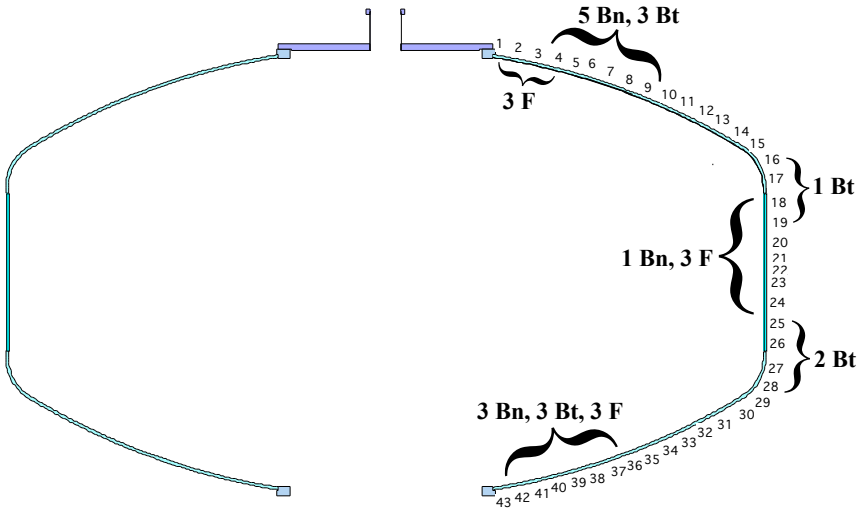

Figure 3-5: A picture of where the different sensors should be placed.

Following the above recommendations, the B_p coils and flux loops have been installed as shown in Table 3.1. Table 3.2 shows the coordinates and angles for the Hall probes. Notice that the coordinates are offset by about 7.6 cm compared to those of the B_p coils since the Hall probes are attached at the ends of the coils. Also, the angles are offset by 180 degrees for some of the probes, because a coil and the probe attached to it have different polarities in some cases. A schematic picture of the coil and loop positions is shown in Figure 3-6, and Figure 3-7 shows the actual "as installed" pictures.

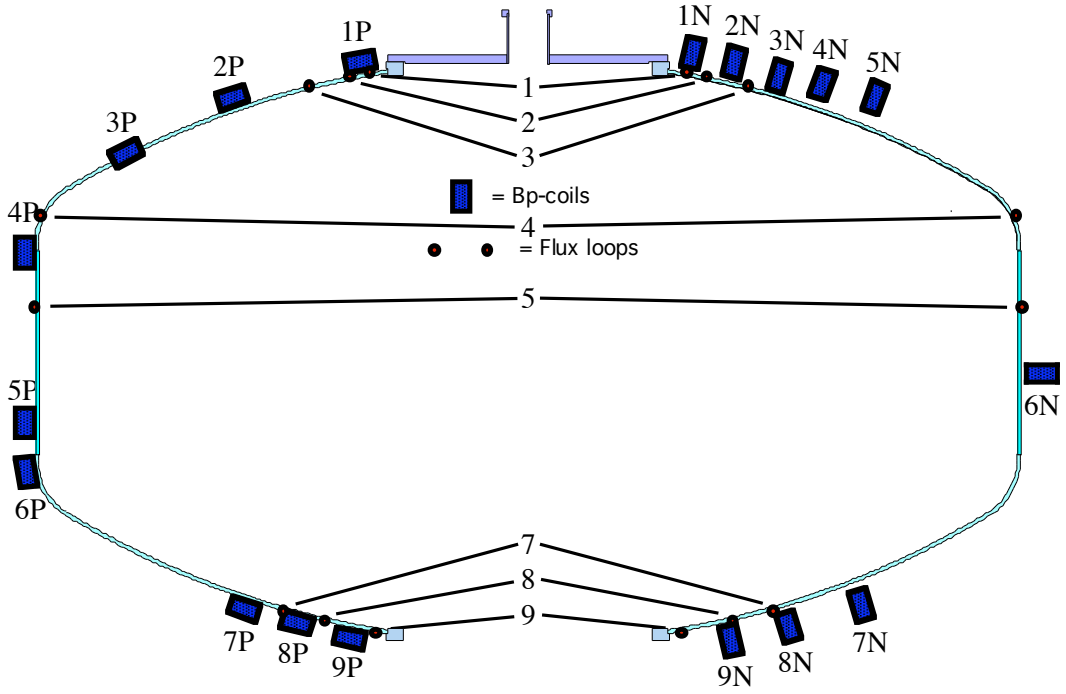

Figure 3-6: A schematic of the sensor locations as installed. The normal and parallel B_p coils are installed on the same poloidal plane although the picture depicts otherwise for clarity.

I.D. #	X (cm)	X Error (cm)	Z (cm)	Z Error (cm)	Θ (deg)	Θ Error (deg)
1N	83.8	1	152.7	1	192	1
1P	86.4	1	148.2	1	280	1
2N	104.8	1	147.6	1	195	1
2P	150.5	1	129.8	1	289	1
3N	127.6	1	141.3	1	197	1
3P	205.1	1	102.3	1	117	1
4N	149.9	1	137.4	1	199	1
4P	257.2	1	51.5	1	180	1
5N	177.2	1	129.8	1	21	1
5P	257.2	1	-36.2	1	180	1
6N	262.3	1	-11.5	1	90	1
6P	255.9	1	-61.0	1	188	1
7N	169.6	1	-128.6	1	342	1
7P	144.8	1	-131.1	1	72	1
8N	133.4	1	-140.0	1	344	1
8P	118.1	1	-138.1	1	254	1
9N	102.9	1	-147.0	1	167	1
9P	91.5	1	-145.7	1	78	1
F1	80.7	1	142.5	1		
F2	91.5	1	140.6	1		
F3	111.8	1	136.2	1		
F4	248.6	1	69.9	1		
F5	251.5	1	22.9	1		
F7	125.1	1	-132.4	1		
F8	104.2	1	-136.8	1		
F9	78.1	1	-142.5	1		

Table 3.1: The (X, Z, Θ) coordinates and their estimated errors of the B_p coils and flux loops. The (X, Z) coordinates are measured from the center of the vacuum vessel, and the angles are measured clockwise from the vertical. In the above, N stands for "normal" (as in normal to the vessel) and P stands for "parallel." The flux loops are designated by F.

I.D. #	X (cm)	X Error (cm)	Z (cm)	Z Error (cm)	Θ (deg)	Θ Error (deg)
1N	85.4	1	160.1	1	12	1
1P	78.9	1	149.6	1	280	1
2N	106.8	1	155.0	1	15	1
2P	143.3	1	132.3	1	289	1
3N	129.9	1	148.5	1	17	1
3P	198.4	1	105.7	1	297	1
4N	152.4	1	144.6	1	19	1
4P	257.2	1	59.1	1	0	1
5N	179.9	1	136.9	1	21	1
5P	257.2	1	-28.6	1	0	1
6N	269.9	1	-11.5	1	90	1
6P	257.0	1	-53.4	1	8	1
7N	171.9	1	-135.8	1	162	1
7P	152.0	1	-128.7	1	72	1
8N	135.5	1	-147.3	1	164	1
8P	125.4	1	-136.0	1	74	1
9N	104.6	1	-154.4	1	167	1
9P	98.9	1	-144.1	1	78	1

Table 3.2: The (X, Z, Θ) coordinates and their estimated errors of the Hall probes.

Figure 3-7: Actual pictures of the B_p coils and flux loops as installed at the top (top right), side (left), and bottom (bottom right) of the vessel.

Chapter 4

Error analysis

Before proceeding to presenting experimental data, a thorough analysis of errors associated with measured and calculated quantities is needed. Errors can come from several sources and be of various types; there may be a precision error in measuring the position of a sensor or a random error in its calibration, for example. Precision and random errors are facts of experiments and cannot be eradicated. Another type of error is systematic error, in which the error is not distributed symmetrically about the "true" value and is biased in either direction. Systematic errors come from systemic problems that somehow shift the measured value from the "true" value. Systematic errors can often be calibrated away or eradicated by identifying the source of the bias. A good experimenter would identify all causes of systematic errors and make sure that they do not distort the measurements. Because all systematic errors can potentially be isolated and eliminated, this chapter will focus on precision and random errors, which are ubiquitous in all experiments.

4.1 Precision errors

Precision errors are not as prominent as random errors, because random errors often dominate over precision errors. However, when a measurement is done using a very simple instrument, like a ruler, then there is minimal source of random errors, and precision errors become the main source of the total error.

In conducting magnetic measurements of plasmas, knowing the precise locations and orientations of the sensors becomes very important. Magnetic sensors measure the plasma current from which the pressure is deduced, so an inaccurate measurement of the sensor locations or orientations could inevitably lead to an inaccurate pressure profile. Once the locations and orientations are measured to the best of our abilities, we need to know the accuracies to within which they are measured. These estimated errors of the locations and orientations will be added to the field or flux measurement error to estimate the errors in the parameters of the pressure profile and other derived quantities such as plasma current and beta by propagating the total error through the equilibrium program.

The locations of LDX magnetic sensors have been measured using a simple ruler. Although the ruler is delineated to $\frac{1}{16}$", the actual resolution of the measurements was $\frac{1}{4}$", giving a uniformly distributed error of about $\pm$ 3 mm. However, taking into account the accuracy of the placement of the ruler itself, the estimated error becomes about 1 cm as noted in Table 3.1. Similarly, the angular orientations of the B_p coils and Hall probes have been measured using a simple protractor. By using a liquid level and a pair of eyes, the angles were measured to about a degree error.

4.2 Random errors

The calibrations of the sensors and their associated electronics have been done with more complicated instruments than a ruler, and random errors consequently dominate the total error. Chapter 2 described how the sensors and electronics were calibrated. This section will discuss how the errors in each calibrated quantity combine to give a comprehensive error in the field or flux measurement.

4.2.1 Errors in the B_p coil and flux loop measurements

Equations 2.6 and 2.7 describe the output voltages of a B_p coil and flux loop, respectively, when they are connected to integrator circuits. The measured field and flux

values can be obtained by simply inverting these equations,

$$\Delta B = \frac{\tau}{NA} V_{out} \tag{4.1}$$

$$\Delta\psi = \tau V_{out} \ . \tag{4.2}$$

Each term on the right hand side has an associated error, and we can write the errors in ΔB and $\Delta\psi$ as functions of the errors on the right hand side,

$$\sigma_{\Delta B} = \sqrt{\frac{V_{out}^2}{(NA)^2}\sigma_\tau^2 + \frac{\tau^2 V_{out}^2}{(NA)^4}\sigma_{NA}^2 + \frac{\tau^2}{(NA)^2}\sigma_{Vout}^2} \tag{4.3}$$

$$\sigma_{\Delta\psi} = \sqrt{V_{out}^2\sigma_\tau^2 + \tau^2\sigma_{Vout}^2} \ . \tag{4.4}$$

The errors in τ and NA can be approximated by their standard deviations in the calibration data, as shown in Tables 2.1 and 2.2. The error in V_{out} is the greater of the bit noise or bit resolution. Everything else in the above equations is known from the calibration data except for V_{out} itself. Since V_{out} is dependent on the actual shot, the same goes for $\sigma_{\Delta B}$ and $\sigma_{\Delta\psi}$. However, for the purpose of estimating $\sigma_{\Delta B}$ and $\sigma_{\Delta\psi}$, we can use a "typical shot" to get V_{out} for each sensor. Because calculating $\sigma_{\Delta B}$ and $\sigma_{\Delta\psi}$ for every shot becomes cumbersome, we will use their "typical shot" values for every shot unless we need to analyze the plasma at a time when the actual V_{out} is significantly different from $V_{out}^{typical}$ for a given sensor.

The "typical" $\sigma_{\Delta B}$ and $\sigma_{\Delta\psi}$ are calculated using shot 50318014. Table 4.2.1 shows the appropriately propagated errors. Because the errors in τ, NA, and V are mostly less than a percent, the propagated errors in ΔB and $\Delta\psi$ are mostly within a percent

I.D. #	NA (m^2)	NA Error (m^2)	τ (s)	τ Error (s)	V_{out} (V)	V_{out} Error (V)	$\Delta B, \psi$
1N	5.22	0.04	0.00498	0.00002	-0.2166	0.0002	-0.000
1P	5.45	0.02	0.000999	0.000011	-0.5360	0.0004	-0.000
2N	5.06	0.01	0.0100	0.0001	-0.0898	0.0002	-0.000
2P	4.92	0.004	0.00202	0.00002	-0.3082	0.0002	-0.000
3N	5.07	0.003	0.009750	0.000092	-0.0779	0.0002	-0.000
3P	5.01	0.02	0.00514	0.00005	0.0966	0.0002	0.0000
4N	5.07	0.003	0.009861	0.000086	-0.0620	0.0002	-0.000
4P	5.24	0.01	0.00203	0.00002	0.1261	0.0002	0.0000
5N	5.21	0.02	0.009858	0.000078	0.0423	0.0002	0.0000
5P	5.20	0.02	0.00508	0.00004	0.0623	0.0002	0.0000
6N	5.22	0.002	0.00510	0.00004	-0.0073	0.0002	-0.000
6P	5.26	0.001	0.00496	0.00004	0.0575	0.0002	0.0000
7N	5.07	0.005	0.0103	0.0001	0.0415	0.0002	0.0000
7P	4.98	0.004	0.00495	0.00007	-0.1506	0.0002	-0.000
8N	5.21	0.01	0.009896	0.000072	0.0821	0.0002	0.0001
8P	5.31	0.01	0.004895	0.000034	0.1526	0.0002	0.0001
9N	5.32	0.01	0.009928	0.000060	-0.1151	0.0002	-0.000
9P	4.99	0.004	0.001956	0.000009	-0.3178	0.0002	-0.000
F1			0.00514	0.00003	-0.1111	0.0002	-0.000
F2			0.00501	0.00003	0.1409	0.0002	-0.000
F3			0.004949	0.000034	0.2175	0.0002	-0.001
F4			0.0207	0.0001	0.1109	0.0002	-0.002
F5			0.0203	0.0002	0.1205	0.0002	-0.002
F7			0.00983	0.00032	0.1369	0.0002	-0.001
F8			0.0101	0.0002	-0.1002	0.0002	-0.001
F9			0.00514	0.00005	0.1125	0.0002	-0.000

as well.

The errors of each factor to calculate the field and flux values are propagated to estimate the field and flux errors.

4.2.2 Errors in the Hall probe measurements

The output voltage of a Hall probe and the field it measures is related by Eq. 4.5,

$$\begin{aligned} B &= \frac{V_0 - V_{OQ(VCC)}}{Sens_{(VCC)}} \\ &= \frac{1}{\beta}(\frac{V_0}{V_{CC}} - \alpha) \ . \end{aligned}$$

Connecting the output to the calibrated amplifier adds a gain factor G to the above,

$$B = \frac{1}{\beta}(\frac{V_0}{GV_{CC}} - \alpha) \ . \tag{4.5}$$

Again, we can propagate the error in each of the terms on the right hand side to obtain the error in the measured field,

$$\sigma_B = \sqrt{\frac{1}{\beta^4}(\frac{V_0}{GV_{CC}} - \alpha)^2\sigma_\beta^2 + (\frac{1}{\beta GV_{CC}})^2\sigma_{V0}^2 + (\frac{V_0}{\beta GV_{CC}^2})^2\sigma_{Vcc}^2 + (\frac{V_0}{\beta G^2 V_{CC}})^2\sigma_G^2 + \frac{1}{\beta^2}\sigma_\alpha^2} \ . \tag{4.6}$$

The errors in α, β, and G can be approximated by their standard deviations in the calibration data (Tables 2.1 and 2.2). The errors in V_0 and V_{CC} are the greater of their bit noise or bit resolution. As with the previous case, everything else in the above is known except for the output voltage V_0, which is dependent on the actual shot. Because the Hall probes measure the absolute magnetic field, V_0 is actually most dependent on the floating coil current. Hence, in order to find the upper bound on the measured field error, it suffices to use the output voltage values at the maximum floating coil current. We will use this maximum error as the measurement error for each Hall probe.

To date, the 50701 shot series has had the highest floating coil current (equivalent to a 400 A charge of the charging coil). Shot 50701005 will be used to represent the series. Table 4.2.2 lists the relevant parameter values and their errors for this shot.

I.D. #	α	α Error	β (G^{-1})	β Error (G^{-1})	Gain	Gain Error	V_{CC} (V)	V_{CC} Error (V)	V_0 (V)	V_0 Error (V
1N	0.5014	0.0004	0.0011	0.00003	2.06	0.001	5.0310	0.0002	6.2518	0.0002
1P	0.5005	0.0017	0.0011	0.0001	2.06	0.001	5.0310	0.0002	4.2983	0.0002
2N	0.5035	0.0003	0.0010	0.00005	2.06	0.002	5.0310	0.0002	6.2876	0.0002
2P	0.5153	0.0005	0.0010	0.00001	2.06	0.001	5.0310	0.0002	4.6382	0.0002
3N	0.5028	0.0005	0.0011	0.00003	2.06	0.002	5.0310	0.0002	5.8419	0.0002
3P	0.5012	0.0004	0.0011	0.0001	2.06	0.001	5.0310	0.0002	4.6757	0.0002
4N	0.5046	0.0001	0.0011	0.00005	2.06	0.002	5.0310	0.0002	5.6894	0.0002
4P	0.5020	0.0001	0.0012	0.0001	2.06	0.002	5.0310	0.0002	4.9782	0.0002
5N	0.5138	0.00003	0.0010	0.0001	2.06	0.002	5.0310	0.0002	5.5571	0.0002
5P	0.5159	0.0004	0.0010	0.00004	2.06	0.001	5.0310	0.0002	5.1048	0.0002
6N	0.5041	0.0003	0.0011	0.00003	2.06	0.001	5.0310	0.0002	5.1935	0.0002
6P	0.5019	0.0004	0.0011	0.00003	2.06	0.003	5.0310	0.0002	4.9564	0.0002
7N	0.5057	0.0004	0.0010	0.00005	2.06	0.001	5.0310	0.0002	4.9850	0.0002
7P	0.5099	0.0003	0.0011	0.0001	2.06	0.0004	5.0310	0.0002	4.6070	0.0002
8N	0.5078	0.0003	0.0010	0.00001	2.06	0.0004	5.0310	0.0002	4.7479	0.0002
8P	0.5060	0.0003	0.0010	0.0001	2.06	0.002	5.0310	0.0002	4.4443	0.0002
9N	0.5048	0.0010	0.0011	0.0001	2.06	0.002	5.0310	0.0002	4.3624	0.0002
9P	0.5055	0.0002	0.0011	0.0001	2.06	0.001	5.0310	0.0002	4.3739	0.0002

The parameter values and their errors used to calculate the field and its error for each sensor for shot 50701005.

4.3 The effect of the sensor position error on the field / flux measurement error

The error in the determination of the sensor positions will add to the error in the actual field or flux measurements to give a comprehensive error. In fact, the position errors can be represented as measured field errors for a given shot. By doing so, the comprehensive error can be written as an appropriate sum of the field error due to the position error and the field error due to the sensor itself. We will use this comprehensive error as the total measurement error for each sensor.

4.3.1 Comprehensive error in the Hall probe measurement

The magnetic field measurement of a Hall probe at a supposed position and angle (X_0, Z_0, Θ_0) can be written as,

$$B = B_{meas} + \delta B(X_0, Z_0, \Theta_0) \ , \tag{4.7}$$

where $\delta B(X, Z, \Theta) = B(X, Z, \Theta) - B(X_0, Z_0, \Theta_0)$. Although $\delta B(X_0, Z_0, \Theta_0)$ itself is zero, its error is nonzero for nonzero errors in X_0, Z_0, and/or Θ_0. The error in δB, which we will write as σ_{pos}, can be written as follows:

$$\sigma_{pos} = \sqrt{\left(\frac{\partial B}{\partial X}\right)^2 \sigma_{X0}^2 + \left(\frac{\partial B}{\partial Z}\right)^2 \sigma_{Z0}^2 + \left(\frac{\partial B}{\partial \Theta}\right)^2 \sigma_{\Theta 0}^2} \ . \tag{4.8}$$

The partial derivatives in the above expression can be found for a particular shot. For the purpose of estimating σ_{pos} (and in keeping with the spirit of the previous section), we will again use shot 50701005. Once σ_{pos} is found for each sensor, the total error in the field measurement is easily calculated as follows:

$$\sigma_{tot} = \sqrt{\sigma_{meas}^2 + \sigma_{pos}^2} \ , \tag{4.9}$$

where σ_{meas} is the measurement error of the sensor itself, as given in Table 4.2.2. Table 4.1 tabulates σ_{meas}, σ_{pos}, and σ_{tot} for each sensor. The table shows that the field measurement error due to the position error contributes minimally to the total measurement error for most sensors. The total error ranges from a few percent to about ten percent for all sensors except for sensor 6N, for which the error is about 20 %.

4.3.2 Comprehensive errors in the B_p coil and flux loop measurements

Similarly to the Hall probes, the field and flux measurements of the coils and loops at position and angle (for the B_p coils) (X_0, Z_0, Θ_0) can be written as,

$$\Delta B = \Delta B_{meas} + \delta \Delta B(X_0, Z_0, \Theta_0) \tag{4.10}$$

$$\Delta \psi = \Delta \psi_{meas} + \delta \Delta \psi(X_0, Z_0) \ , \tag{4.11}$$

where $\delta \Delta B(X, Z, \Theta) = \Delta B(X, Z, \Theta) - \Delta B(X_0, Z_0, \Theta_0)$ and $\delta \Delta \psi(X, Z) = \Delta \psi(X, Z) - \Delta \psi(X_0, Z_0)$. Just like for the Hall probes, we will call the error in $\delta \Delta B$ and $\delta \Delta \psi$

I.D. #	σ_{meas} (G)	σ_{pos} (G)	σ_{tot} (G)
1N	3	1	3
1P	7	2	7
2N	5	1	5
2P	1	1	1
3N	2	1	2
3P	3	0.3	3
4N	2	1	2
4P	1	0.3	1
5N	1	1	2
5P	1	0.1	1
6N	0.4	0.4	0.6
6P	1	0.2	1
7N	1	1	1
7P	5	1	5
8N	1	1	1
8P	5	1	5
9N	7	1	7
9P	7	2	7

Table 4.1: The total measurement errors of the Hall probes and the measurement and position errors that contribute to them.

$\sigma^{pos}_{\Delta B}$ and $\sigma^{pos}_{\Delta\psi}$, respectively. These errors are expressed as,

$$\sigma^{pos}_{\Delta B} = \sqrt{\left(\frac{\partial \Delta B}{\partial X}\right)^2 \sigma^2_{X0} + \left(\frac{\partial \Delta B}{\partial Z}\right)^2 \sigma^2_{Z0} + \left(\frac{\partial \Delta B}{\partial \Theta}\right)^2 \sigma^2_{\Theta 0}} \tag{4.12}$$

$$\sigma^{pos}_{\Delta\psi} = \sqrt{\left(\frac{\partial \Delta\psi}{\partial X}\right)^2 \sigma^2_{X0} + \left(\frac{\partial \Delta\psi}{\partial Z}\right)^2 \sigma^2_{Z0}}\ . \tag{4.13}$$

To get the typical values for the partial derivatives, we will use shot 50318014 as before. The measurement and position errors add in quadrature again to produce the total error for each detector. The results are tabulated in Table 4.2. The total errors in ΔB range from a few percent to about 10 % of the typical diamagnetic field measurements given in Table 4.2.1. Unlike for the Hall probes, the position error contributes slightly more than the sensor measurement error to the total measurement error for most of the B_p coils and flux loops.

4.4 Error in the determination of the floating coil current due to the errors in the Hall probe measurements

The Hall probes are primarily used to measure the floating coil current, hence the errors in their measurements directly translate to an error in the current measurement. The F-coil current is found by scanning its current in the equilibrium program with zero pressure (i.e. vacuum condition) and finding the best fit to the Hall probe measurements. Because the coil current is not directly a function of the probe measurements, the current error cannot be expressed as a function of the errors in the field measurements. However, the current error can be estimated by propagating the field measurement errors through the equilibrium program.

The magnetic field measurements are inputs to the equilibrium program, which outputs the best fit current. By varying each field measurement accordingly to a normal distribution with a mean of the measured value and standard deviation of the measurement error, the best fit current will be varied as well. We can estimate

I.D. #	σ_{meas} (T, Wb)	σ_{pos} (T, Wb)	σ_{tot} (T, Wb)
1N	0.000002	0.000008	0.000008
1P	0.0000012	0.0000148	0.0000148
2N	0.000002	0.000008	0.000008
2P	0.000001	0.000008	0.000008
3N	0.000001	0.000008	0.000008
3P	0.0000010	0.0000032	0.0000034
4N	0.000001	0.000008	0.000008
4P	0.0000005	0.0000032	0.0000032
5N	0.0000007	0.0000072	0.0000072
5P	0.0000005	0.0000024	0.0000025
6N	0.0000002	0.0000048	0.0000048
6P	0.0000004	0.0000028	0.0000028
7N	0.0000007	0.0000080	0.0000080
7P	0.000002	0.000008	0.000008
8N	0.000001	0.000008	0.000008
8P	0.000001	0.000012	0.000012
9N	0.000001	0.000008	0.000008
9P	0.000001	0.000016	0.000016
F1	0.000004	0.000016	0.000016
F2	0.000005	0.000016	0.000017
F3	0.000007	0.000020	0.000021
F4	0.00002	0.000012	0.00002
F5	0.00002	0.000016	0.00003
F7	0.00004	0.000020	0.00004
F8	0.00002	0.000020	0.00003
F9	0.000006	0.000016	0.000017

Table 4.2: The total measurement errors of the B_p coils and flux loops and the measurement and position errors that contribute to them.

Best fit current (A)	χ^2	I_{mean} (A)	I_{SD} (A)
1167000	47	Unperturbed	
1168750	67		
1161250	58		
1146250	85		
1164500	73		
1149500	64		
1149000	85		
1160750	71		
1155250	89	1160000	9250
1165500	55		
1173750	56		
1165750	31		
1173750	56		
1159000	53		
1144500	70		
1155750	73		

Table 4.3: Variations of the best fit current due to random variations in the measured fields.

the error in the current due to the errors in the field measurement by the standard deviation of the distribution of the best fit currents. The result for shot 50701005 is shown in Table 4.3.

A total of 15 perturbed and one unperturbed runs have been performed. The standard deviation of the 16 runs was about 9250 A, which is less than one percent of the coil current. This gives us some confidence that with the field measurement errors we have, we can measure the floating coil current to within a percent or so. It is noteworthy to mention that the estimated error in the deduced coil current is much less than the average measurement error of the Hall probes. This is an attribute and

Equilibrium quantity	Unperturbed	Average	S.D.
Plasma current (A)	3360.71	3401.94	415.36
Current centroid (m)	0.922744	0.920595	0.020000
Plasma volume (m^3)	28.39	28.39	0.012
Peak beta (%)	9.485	9.584	1.192
Average beta (%)	0.823819	0.822412	0.043108
Stored energy (J)	218.197	218.169	1.332

Table 4.4: Variations of the equilibrium quantities due to random variations in the measured diamagnetic fields and fluxes.

the essence of the fitting scheme; it mitigates the errors associated with each sensor and gives a relatively robust result.

4.5 Equilibrium quantity errors due to the errors in the B_p coil and flux loop measurements

Given the floating coil current obtained from the Hall probe measurements, the B_p coil and flux loop measurements roughly provide the equilibrium plasma current. This current is related to pressure through equilibrium reconstruction, and equilibrium quantities are subsequently found. Consequently, the errors in the B_p coil and flux loop measurements lead to errors in the determination of the equilibrium quantities such as plasma current and beta.

Like for the Hall probes, the B_p coil and flux loop measurements are varied accordingly to appropriate Gaussian distributions, and the errors in the equilibrium quantities are estimated. Eleven perturbed and one unperturbed runs have been conducted on shot 50701013, as shown in Table 4.4. Most of the equilibrium quantities have errors, as estimated by their standard deviations, ranging from less than a percent to about 10 %. Although the errors may have been somewhat underestimated due to the resolution of the varied parameters, a few percent error in a given

equilibrium quantity is definitely satisfactory.

Chapter 5

Equilibrium and Stability of LDX Plasma

A plasma confined in a dipole magnetic geometry exhibits unique equilibrium and stability properties that are not seen in tokamaks or other magnetic confinement devices. However, the dipole geometry has certain similarities with hardcore z-pinches and mirror machines, and there consequently is some overlap in the physics principles of these apparatus. For example, the stability of a hardcore z-pinch greatly depends on the plasma pressure gradient and the plasma pressure can be highly anisotropic in a mirror machine, both properties of which are observed in LDX. In fact, a hardcore z-pinch is approximately a very high aspect ratio LDX, in which the curvature of the internal coil is taken to be zero, and its stability properties have been studied extensively to give insight into the stability properties of LDX [23].

The Levitated Dipole Experiment is not the first experiment to study plasma confinement in a dipolar field. The Collisionless Terrella Experiment (CTX) at Columbia University has been operating long before LDX to study plasma fluctuations and transport in a supported dipole [26, 29, 30]. The University of Tokyo is a host to several supported and levitated dipole experiments including Proto-RT (supported) [42, 43], mini-RT (levitated), and RT-1 (levitated). RT-1, which has just recently started operation earlier this year, is a larger version of mini-RT but still much smaller than LDX. Before the existence of laboratory dipole confinement devices, much of the

experimental studies of dipolarly confined plasmas had been conducted on planetary magnetospheres [13, 4]. Accordingly, basic equilibrium and stability properties of plasmas in a dipole field had been developed long before the first laboratory apparatus was ever built.

5.1 Plasma equilibrium in LDX

The equilibrium of LDX plasma is described by the ideal MHD theory. Although the equilibrium can also be described by kinetic or single particle theories, MHD provides the essence of the macroscopic picture. The relevant equations are,

$$\boldsymbol{\nabla} \cdot \boldsymbol{B} = 0 \tag{5.1}$$

$$\boldsymbol{\nabla} \times \boldsymbol{B} = \mu_0 \boldsymbol{J} \tag{5.2}$$

$$\boldsymbol{\nabla} P = \boldsymbol{J} \times \boldsymbol{B} \ . \tag{5.3}$$

The first two equations are two of Maxwell's equations, and the third is the MHD momentum balance equation. The momentum balance equation in the above form assumes an isotropic pressure, but it can be recast in an anisotropic form by substituting $\boldsymbol{\nabla} \cdot \boldsymbol{P}$ for $\boldsymbol{\nabla} P$, where $\boldsymbol{P}$ is the pressure tensor. The above three equations can be combined to derive the Grad-Shafranov equation [8],

$$\Delta^* \psi = -\mu_0 R^2 \frac{dP}{d\psi} - F \frac{dF}{d\psi} \ . \tag{5.4}$$

In the above, $\Delta^* \equiv R^2 \boldsymbol{\nabla} \cdot \left(\frac{\boldsymbol{\nabla}}{R^2} \right)$ is an elliptic differential operator, and $F \equiv R B_\phi$ is a function of ψ. Because there is no toroidal field in LDX, the second term is identically zero. The G-S equation without the second term is what the equilibrium program solves to obtain $P(\psi)$ given the external magnetic measurements.

The magnetic field in LDX is provided by the floating coil and plasma current. Because the plasma current flows in the same direction as the floating coil current and is typically less than 1% of the floating coil current, the equilibrium field is well approximated by the vacuum field. The field of a dipole decreases as $\frac{1}{R^3}$ on the equatorial plane. Unlike in a tokamak, there is no driven plasma current in LDX;

the plasma current consists only of diamagnetic current and is a consequence of the pressure gradient,

$$\boldsymbol{J} = -\frac{\boldsymbol{\nabla} P \times \boldsymbol{B}}{B^2} \ . \tag{5.5}$$

The above relation shows that a purely poloidal vacuum field gives rise to a purely toroidal diamagnetic current, which in turn adds to the poloidal field. Constant ψ contours for a typical LDX equilibrium is shown in Figure 5-1.

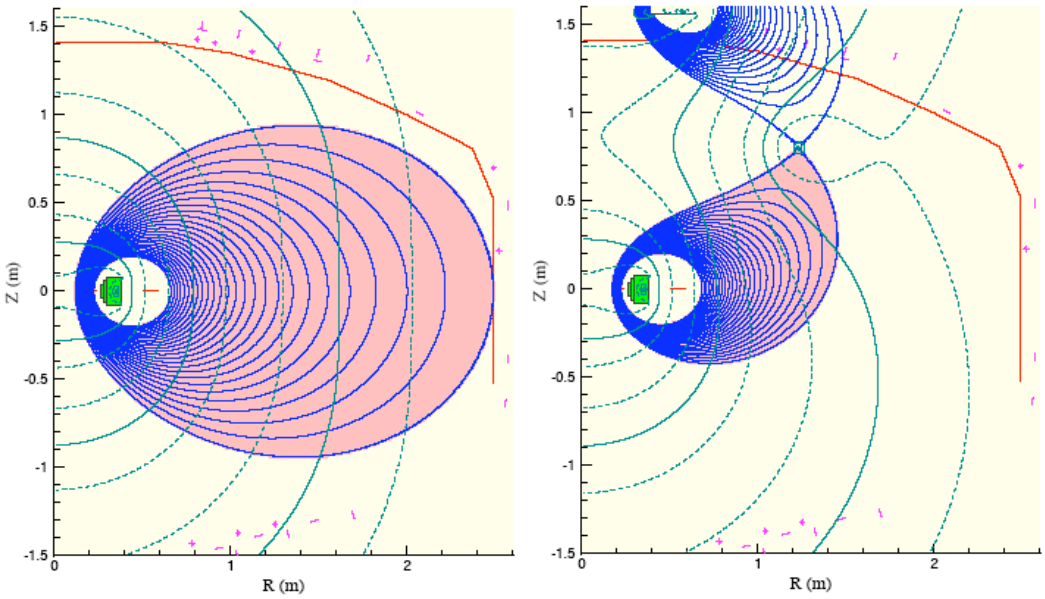

Figure 5-1: Constant ψ contours for a typical LDX equilibrium (a) without the levitation coil current and (b) with the levitation coil at its nominal current.

An important quantity in the dipole magnetic geometry is the differential flux tube volume per differential flux, defined as the following:

$$V \equiv \frac{dVol}{d\psi} = \oint \frac{dl}{B} \ . \tag{5.6}$$

The closed line integral on the right hand side is taken along a field line. Because B decreases and $\oint dl$ increases as one moves away from the dipole, the flux tube volume per unit flux increases rapidly as R increases. In fact, $B \sim R^{-3}$ and $\oint dl \sim R$, so $V \sim \frac{R}{R^{-3}} = R^4$. In the next section, we will see that the condition $PV^\gamma = \text{const.}$ is the marginal stability criterion for MHD interchange modes. If we maximize the pressure gradient at the marginal stability limit, the pressure dependence on the equatorial radius can be found,

$$P \sim V^{-\gamma} \sim R^{-4\gamma} = R^{-\frac{20}{3}} , \tag{5.7}$$

where we have assumed a γ value of $\frac{5}{3}$ for a 3-D collisional gas. Hence, at marginal stability, the maximum attainable pressure is strongly dependent on the edge pressure and and peak pressure position; the greater the edge pressure and closer the peak position to the floating coil, the greater the peak pressure and beta. In other words, the edge condition and the heating location will strongly influence the energy characteristics of the plasma. Figure 5-2 shows a sample pressure profile.

5.2 Interchange instabilities

LDX plasmas are susceptible to two types of interchange instabilities, one driven by the pressure gradient of the bulk electrons and the other driven by a population of hot electrons. As mentioned in Ch. 1 and 2, the first phase of operation involves a significant population of hot electrons that carry most of the pressure. Accordingly, the interchange instability caused by hot electrons, or the hot electron interchange instability (HEI), is the dominant instability in this phase of operation. By the third phase of operation, when a more Maxwellian population of electrons is produced, the dominant instability is expected to shift from HEI to the MHD interchange mode.

5.2.1 MHD Pressure Driven Interchange

MHD instabilities can be broadly classified into two categories. The first is the current driven modes, and the second is the pressure driven modes. Current driven modes, or

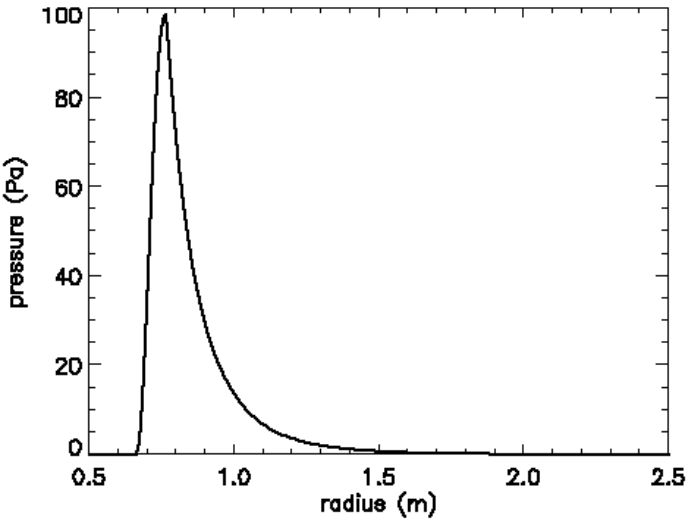

Figure 5-2: A sample pressure profile with $P_{edge} = 0.025$ Pa and $R_{peak} = 0.76$ m. The marginal stability gradient of $P \sim R^{-\frac{20}{3}}$ was used.

kink modes, are a consequence of currents flowing parallel to the magnetic field. Kink modes are absent in LDX since the diamagnetic current always flows perpendicularly to the magnetic field by definition. Therefore, we only need to worry about pressure driven modes.

Microscopic picture of an interchange

Before discussing the macroscopic fluid picture of the interchange mode, it is instructive to consider what goes on at the particle level during an interchange event. Consider a perturbation to the plasma as depicted in Figure 5-3. The picture is a top view of the LDX plasma, looking down along the poloidal field. The field lines are not bent by this perturbation since its direction is perpendicular to the field line direction. Assume that the dipole is located to the left of the picture so that the magnetic curvature and field gradient point to the left. Also, the density to the left of the perturbation is greater than that to the right. Given this geometry and perturbation, $\boldsymbol{\nabla} B$ and curvature drifts drive the ions upward and electrons downward on each side of the perturbation. The resulting charge separation induces local electric fields around the perturbation. Finally, these electric fields interact with the magnetic field to drive local $\boldsymbol{E} \times \boldsymbol{B}$ flows that increase the perturbation.

This instability can be suppressed if there is sufficient flux volume expansion to allow for a density decrease as the perturbation moves into a lower density area, and vice versa. Then the charge separation will be eliminated, and the electric field driving the perturbation will be quenched. The condition for this sufficient flux volume expansion is discussed next in the context of the macroscopic picture.

Fluid picture of an interchange

The energetics of an interchange motion of a magnetized plasma was first studied by Rosenbluth and Longmire [41]. The 1957 paper considered how the magnetic and internal energies of a plasma changed when two flux tubes were interchanged as in Figure 5-4. It was shown that the magnetic energy remained constant if both the flux tubes contained the same amount of flux, and the internal energy changed as the

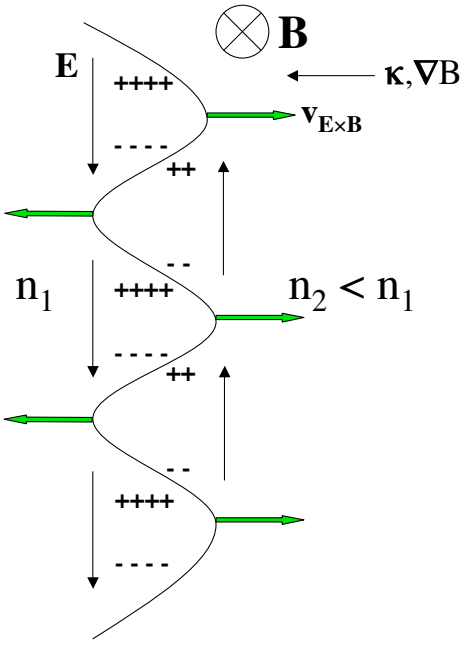

Figure 5-3: A particle picture of an interchange event. Different particle drifts collude to drive the perturbation.

following:

$$\Delta E_p = V^{-\gamma}\delta(PV^{\gamma})\delta V \ . \tag{5.8}$$

Stability was ensured for $\Delta E_p > 0$. Hence, in going from the pressure peak to the plasma edge, stability meant $\delta(PV^{\gamma}) > 0$ since $\delta V > 0$. The marginal stability condition was given by $PV^{\gamma} = \text{const}$. The marginal condition allowed the steepest pressure gradient before the plasma became unstable to interchange.

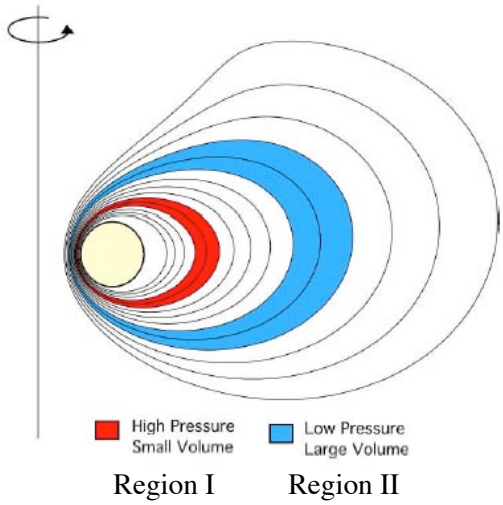

Figure 5-4: If the interchange of Region I and Region II results in a lower energy state, then the plasma is unstable to this interchange.

The Energy Principle

The energy principle, as described in [8], is a powerful tool to analyze the stability of a magnetic plasma confinement device. Because the principle is based on the

linearization of the MHD equations, it does not describe the evolution of an instability. Instead, it is used to answer whether a given magnetic configuration can be unstable to a given mode, and under what conditions can stability be maintained. The following expression serves as the kernel of the energy principle:

$$\delta W_F = \frac{1}{2}\int_P d\boldsymbol{r}\left[\frac{|\boldsymbol{Q}_\perp|^2}{\mu_0} + \frac{B^2}{\mu_0}|\boldsymbol{\nabla}\cdot\boldsymbol{\xi}_\perp + 2\boldsymbol{\xi}_\perp\cdot\boldsymbol{\kappa}|^2 + \gamma P|\boldsymbol{\nabla}\cdot\boldsymbol{\xi}|^2 - 2(\boldsymbol{\xi}_\perp\cdot\boldsymbol{\nabla}P)(\boldsymbol{\kappa}\cdot\boldsymbol{\xi}_\perp^*) - J_\parallel(\boldsymbol{\xi}_\perp^*\times\boldsymbol{b})\cdot\boldsymbol{Q}_\perp\right] . \quad (5.9)$$

In the above, $\boldsymbol{Q}\equiv\boldsymbol{\nabla}\times(\boldsymbol{\xi}\times\boldsymbol{B})$, $\boldsymbol{\kappa}\equiv\boldsymbol{b}\cdot\boldsymbol{\nabla}\boldsymbol{b}$ is the magnetic curvature, and $\boldsymbol{\xi}$ is the displacement vector.

The energy principle states that $\delta W > 0$ for all possible displacements is a necessary and sufficient condition for stability. Although δW consists of three terms corresponding to the plasma, surface, and vacuum energies, the plasma energy term (Eq. 5.9) is the most important since it is the only term with destabilizing terms. By inspection, we can see that there are two potentially destabilizing terms; one of them depends on $\boldsymbol{\nabla}P$ and $\boldsymbol{\kappa}$ while the other depends on $J_\parallel$. Naturally, the first one is associated with pressure driven modes and the second one with current driven modes. Each of these terms is destabilizing when the quantity on the right of the minus sign is positive. As mentioned before, LDX equilibrium does not have parallel currents, so current driven modes are immaterial. However, the LDX geometry makes it susceptible to pressure driven modes in certain regions in the plasma.

A closer inspection of the pressure term reveals that it is destabilizing when $\boldsymbol{\nabla}P\cdot\boldsymbol{\kappa} > 0$. In LDX, magnetic curvature always points towards the dipole, so the plasma between the pressure peak and the wall can potentially be unstable (Figure 5-5). This instability manifests itself as either an interchange mode or ballooning mode.

The pressure driven modes can be stabilized by the stabilizing terms in the energy expression. Each of the stabilizing terms have a physical interpretation. The first term represents the energy needed to bend field lines, the second is the field compression energy, and the third is the plasma compression energy. The plasma compression energy, or compressibility, can often be set to zero in tokamaks to look for the most unstable states, but the closed field line topology of LDX necessarily makes it positive

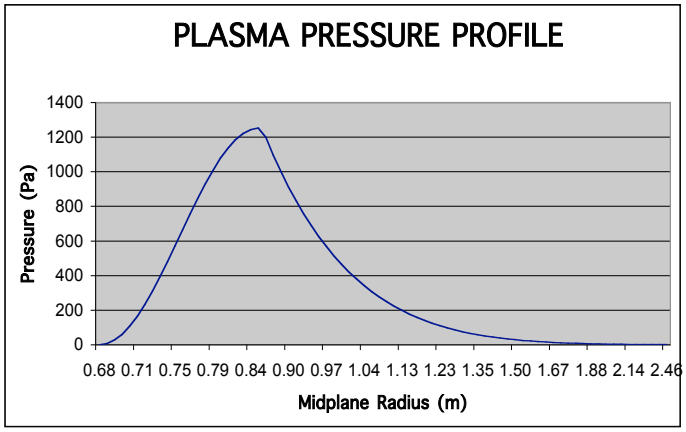

Figure 5-5: The plasma region outside of the pressure peak has the magnetic curvature and pressure gradient pointing in the same direction and thus can be unstable.

and stabilizing. The implication is that modes that do not bend or compress magnetic field lines can be stabilized by this term. In fact, compressibility is the dominant stabilizing term that stabilizes the pressure driven modes in LDX.

As discussed earlier, interchange modes in LDX are stabilized if $\delta(PV^{\gamma}) > 0$. This condition is equivalent to the compressibility term overpowering the destabilizing pressure driven term in the plasma region between the pressure peak and the wall for all allowable interchange motions. However, for ballooning modes, the pressure driven term can locally become very large, and the field line bending energy becomes an important stabilizing term. Garnier shows in [11] that if an equilibrium is stable to interchange modes, then it is also stable to high-n ballooning modes. Because high-n modes are the most unstable of the ballooning modes, we can see that $\delta(PV^{\gamma}) > 0$ is a necessary and sufficient condition for MHD stability.

Anisotropic Effect

The energy principle discussed above must be slightly altered when anisotropic pressure effects are incorporated. In particular, the stabilizing plasma compressibility term has to be derived using kinetic theory, resulting in the Krukal-Oberman form of the energy principal. A rather simple expression, much like the expression in the isotropic case, for interchange stability can be derived if we assume that the ratio of $P_{\perp}$ to $P_{\parallel}$ is constant throughout the plasma, $\frac{P_{\perp}}{P_{\parallel}} = 1 + 2p$, where p is the anisotropy parameter. When the appropriate minimizations are done via the energy principle, the following criterion is obtained [45]:

$$\frac{\widehat{\gamma}\widehat{V}'}{\widehat{V}} + \frac{\widehat{P}'}{\widehat{P}} < 0 \ , \tag{5.10}$$

where $\widehat{\gamma} \equiv \gamma\left(\frac{1+\frac{4}{5}p}{1+\frac{4}{3}p}\right)$, $\widehat{P} \equiv P(\psi)\left[\frac{B_0(\psi)}{B^*}\right]^{2p}$, and $\widehat{V} \equiv \oint \frac{dl}{B}\left(\frac{B^*}{B}\right)^{2p}$. Also, B_0 is the magnetic field on the midplane, B^* is a constant reference magnetic field, and $' \equiv \frac{d}{d\psi}$. As will be seen in the next chapter, pressure becomes a function of both ψ and B when it is anisotropic; $\widehat{P}$ is the part of pressure that is dependent only on ψ,

$$P_{\parallel}(\psi, B) = \widehat{P}(\psi)\left(\frac{B^*}{B}\right)^{2p} \ . \tag{5.11}$$

Also,

$$P_{\parallel}(\psi, B_0) = P(\psi) \ . \tag{5.12}$$

The form of the stability criterion for anisotropic pressure is identical to that for isotropic pressure, but now the quantities are dependent on the anisotropy parameter, p. To see how anisotropy affects the pressure gradient limit, we need to isolate $\frac{P'}{P}$ in the above expression. After some algebra, the criterion becomes,

$$\left.\frac{P'}{P}\right|_{\text{anisotropic}} < -\frac{\widehat{\gamma}\widehat{V}'}{\widehat{V}} - 2p\frac{B_0'}{B_0} \ . \tag{5.13}$$

The criterion in the isotropic case is equivalent to the above with $p = 0$,

$$\left.\frac{P'}{P}\right|_{\text{isotropic}} < -\frac{\gamma V'}{V} \ . \tag{5.14}$$

The right hand side of the anisotropic criterion can be numerically evaluated and compared to the right hand side of the isotropic criterion. The result shows that adding anisotropy affects the gradient limit by a mere 4 %,

$$\left.\frac{P'}{P}\right|_{\text{anisotropic}} \lesssim -1.04\frac{\gamma V'}{V} \ . \tag{5.15}$$

5.2.2 Hot Electron Interchange

When there is a significant fraction of hot electrons in the plasma, such as in LDX, hot electron interchange mode becomes a relevant potential instability. Because hot electrons violate the high collisionality assumption of ideal MHD, they do not strictly adhere to MHD stability laws. A kinetic analysis must be performed to characterize interchange modes of hot electrons. The reader can refer to [21, 1, 9], for example, for the derivation and observation of the hot electron interchange (HEI) mode. General characteristics of the HEI are described here.

The stability condition for the HEI is given as follows:

$$-\frac{d\ln\bar{n}_h}{d\ln V} < 1 + \frac{m_\perp^2}{24}\frac{\omega_{dh}}{\omega_{ci}}\frac{\bar{n}_i}{\bar{n}_h} \ . \tag{5.16}$$

In the above, $m_\perp$ is the perpendicular wave number, $\bar{n}_h$ is the flux-tube averaged hot electron density, $\bar{n}_i$ is the flux-tube averaged ion density, ω_{dh} is the hot electron

curvature drift frequency, and ω_{ci} is the ion cyclotron frequency. Unlike the MHD interchange mode, the HEI imposes a gradient limit on the density rather than on the pressure. This means that the hot electron pressure gradient can exceed the MHD limit without being unstable. The additional stability comes from the interaction of the hot electrons with the background ions. Stability to the HEI is enhanced by increasing the right hand side of the inequality. Because ω_{dh} is proportional to the hot electron energy, the hotter hot electrons can sustain a steeper density gradient than the cooler ones. Also, too much hot electron in the plasma can seriously degrade its stability by limiting the density gradient at a low level. This situation can arise when there are not enough neutrals to collide with the hot electrons during plasma startup in the presence of ECRH heating.

5.3 Summary of LDX Equilibrium and Stability

The equilibrium of LDX has a very simple configuration with a purely poloidal field and a purely toroidal current. The current is naturally driven by the pressure gradient (i.e. diamagnetic) and does not need an external driving source. It is interesting to note that the cause and effect of the diamagnetic current and the pressure gradient is a classical chicken or the egg conundrum. In the light of the MHD momentum balance, we know that there needs to be a pressure gradient in order for the diamagnetic current to exist, and vice versa. What is not obvious is whether one causes the other or they come to coexist simultaneously.

The two relevant instabilities for LDX plasmas are the MHD and hot electron interchange modes. The MHD interchange stability criterion can be derived by considering the energy involved in interchanging two flux tubes (fluid elements) in the plasma. An equivalent, and perhaps more sophisticated, derivation is done by writing down the different potential energy terms of the plasma as a function of a perturbation and minimizing them. This so-called energy principle and the energy consideration of exchanging two flux tubes give the marginal pressure gradient criterion, $PV^{\gamma} = \text{const.}$ The effective value of γ slightly increases when pressure anisotropy is included. The

MHD interchange criterion roughly applies to the cold background electrons, but the ECRH heated hot electrons follow a kinetic analog of the MHD interchange called the hot electron interchange mode. The HEI puts a restriction on the hot electron density gradient rather than on the pressure gradient. The hot electrons can therefore attain pressure gradients that exceed the MHD limit.

Chapter 6

Equilibrium Reconstruction

Equilibrium reconstruction is a process by which magnetic and possibly other measurements are used to find key equilibrium parameters. Because plasma equilibrium is most often described by MHD, the physics that relates magnetic measurements to equilibrium quantities is governed by MHD equations. The Grad-Shafranov equation encompasses the key physics that plays a principal role in the reconstruction process. However, the G-S equation, and MHD theory for that matter, lacks one physics detail that is needed to carry out the reconstruction. The equation (Eq. 5.4) has a $\frac{dP}{d\psi}$ term on the right hand side, and MHD indeed shows that pressure is a function of magnetic flux. What MHD does not provide is the actual function $P(\psi)$. Without knowing the functional form of P, the G-S equation cannot be solved. Hence, some kind of a pressure model must be developed to enable the process. The model will typically have free parameters that get adjusted during reconstruction to fit the magnetic data. While the quality, or validity, of the chosen model is given by the goodness of fit parameter χ^2, its particular choice may have a significant effect on the reconstruction result.

Reconstruction is a very machine dependent process, and different experimental apparatus will have their own idiosyncrasies. LDX is no exception. The goal of this chapter is to give an expose of some of the unique features of LDX equilibrium reconstruction and provide potential solutions to overcome them if they happen to be problems that impede the process.

6.1 Reconstruction procedure

The reconstruction procedure begins with determining the floating coil current using the Hall probe measurements. The current is found by a least-squares fit method; a parameter called χ^2 that measures the deviation of the measured fields from the fields calculated for a given current is minimized,

$$\chi^2 = \sum_{i=0}^{18} \frac{(B_i^{meas} - B_i^{calc})^2}{\sigma_i^2} \ , \tag{6.1}$$

where σ_i^2 is the total measurement error of the i-th probe. The minimum χ^2 gives the best fit current, which is subsequently used to calculate the vacuum field. The Hall probe measurements are taken before the plasma is produced to isolate the vacuum field.

The next step is to choose the time at which the plasma is to be reconstructed. Once the time is chosen, the diamagnetic field and flux measurements from the B_p coils and flux loops are obtained. The diamagnetic field and flux are added to the vacuum field and flux at each sensor location to find the total field and flux in the presence of the plasma. As simple as it seems, this step actually warrants a closer inspection.

6.1.1 Conservation of the floating coil flux

Because the LDX floating coil is a superconductor, the flux linked to it must stay constant. This implies that the floating coil current must *decrease* when the plasma is created, because the plasma diamagnetic current is in the same direction as the floating coil current and therefore adds to its flux. Now, the B_p coils and flux loops measure the change in the fields and fluxes from the vacuum field to the plasma field. This means that they measure the sum of the field and flux change due to the floating coil current decrease and the field and flux change due to the production of the plasma current,

$$\Delta B = \Delta B_{f-coil} + \Delta B_{plasma} \tag{6.2}$$

$$\Delta \psi = \Delta \psi_{f-coil} + \Delta \psi_{plasma} \ . \tag{6.3}$$

The total field and flux in the presence of the plasma is,

$$B_{total} = B_{vac} + \Delta B_{f-coil} + \Delta B_{plasma} = B_{vac} + \Delta B \tag{6.4}$$

$$\psi_{total} = \psi_{vac} + \Delta\psi_{f-coil} + \Delta\psi_{plasma} = \psi_{vac} + \Delta\psi \ . \tag{6.5}$$

Hence, adding the field and flux values measured by the B_p coils and flux loops to the vacuum field and flux values still give us the total field and flux with the plasma. However, when the equilibrium code is run to reconstruct the plasma, the decrease in the floating coil current must be taken into account. In other words, the current we ascribe to the floating coil during plasma reconstruction is *less* than that found via the best fit algorithm.

A potential problem arises here. We need to know the plasma current profile to find the mutual inductance between the plasma and the floating coil and thus the current decrease, but we also need to know the current decrease to find the correct floating coil current to use in the reconstruction of the plasma current profile. This circle must be broken somewhere to resolve the issue.

The flux conservation requirement is given as the following:

$$L_f I_f = L_f(I_f + \Delta I_f) + M_{fp} I_p \tag{6.6}$$

$$\Rightarrow \Delta I_f = -\frac{M_{fp}}{L_f} I_p \ , \tag{6.7}$$

where the f and p subscripts designate floating coil and plasma, respectively. The self-inductance of the floating coil is known from its geometry, but the mutual inductance between the floating coil and the plasma and the plasma current are unknown before the reconstruction. The mutual inductance can be roughly estimated by calculating the mutual between the floating coil and a current ring at a plausible radius, giving $L_f \sim 3$–$5 M_{fp}$. With a typical diamagnetic current ~ 2.5 kA and a typical floating coil current ~ 1 MA, we get $\frac{\Delta I_f}{I_f} \sim -\frac{500 \text{ A}}{1 \text{ MA}} = -0.05$ %. Although the floating coil current decrease is a tiny fraction of the floating coil current, it can lead to ascribing significantly more current to the plasma and therefore changing the reconstruction results.

A more accurate calculation of the floating coil current decrease is done by defining

the mutual inductance between the coil and the plasma as [33, 34],

$$M_{fp} \equiv \frac{1}{I_p} \sum_{i=1}^{N} \int \int M_i(x,z) J_p(x,z) dx dz \ . \tag{6.8}$$

Eq. 6.8 assumes that the floating coil consists of N current loops, and $M_i(x,z)$ is the mutual inductance between a current filament at (x,z) and the i-th loop of the floating coil. As stated before, we do not know $J_p(x,z)$ *a priori*, but we can find it to within a given tolerance by iterating through the reconstruction procedure. First, assume that the B_p coil and flux loop measurements are of the diamagnetic current only (i.e. $\Delta I_f = 0$). Next, carry out the reconstruction with this assumption to find the diamagnetic current. Finally, use the obtained plasma current distribution to find ΔI_f, and repeat until the desired tolerance is reached. The good news is that this procedure converges quickly and can be accomplished without carrying out the full plasma reconstruction. The problem is purely electromagnetic and involves no plasma physics, so there is absolutely no need to waste time solving the Grad-Shafranov equation. Instead of iterating through the full reconstruction procedure, both the plasma current distribution and the decrease in the floating coil current can be found by iterating through a current filament code much like MFIT used in tokamaks.

6.1.2 DFIT: The Dipole Current Filament Code

A current filament code that allows for a fast reconstruction of the plasma current has been developed by Prof. Mike Mauel of Columbia University [38]. The code is purely electromagnetic and does not have the capability of reconstructing plasma parameters besides the current distribution. Because the code does not have to solve a PDE like the full reconstruction code, it is extremely fast and ideal for monitoring the plasma current on a shot by shot basis. Part of its speed comes from using only two current filaments to model the plasma; the obvious downside to the simplicity is that the current profile it can deduce is very coarse. The code, however, does an excellent job finding integrated quantities of the current profile such as the total current, its

centroid, its dipole moment, and the mutual inductance between the floating coil and the plasma.

The DFIT code works by changing the magnitude and location of the two current filaments and finding the best fit to the magnetic data. Technically, there are a total of six free parameters (current magnitude, x position, and z position times two filaments) to be adjusted, but the assumption of up-down symmetry allows us to constrain the z positions to the midplane (i.e. $z = 0$). This, however, cannot be done when the levitation coil is activated since the up-down symmetry will be broken.

The real merit of the DFIT code is that it has the capability of holding the floating coil flux constant while the best fit is found. This allows us to forgo the iterative process needed to find the floating coil current decrease and the diamagnetic current. The floating coil current decrease obtained from DFIT can be used to find the actual floating coil current in the presence of the plasma, which is a required input to the reconstruction program.

6.2 Reconstruction methods

6.2.1 Full Reconstruction

The standard reconstruction method involves iteratively solving the Grad-Shafranov equation to obtain the best fit equilibrium parameters for the chosen pressure model. Different parameters may depend on the model to different degrees. The characteristics of different pressure models will be discussed in the next section. The iterative process actually consists of an inner loop, in which ψ is varied to solve the equation for fixed parameter values, and an outer loop, in which the parameter values are varied. The inner loop is solved by using the Green's function approach along with the Picard iteration scheme [25, 24]. The outer loop can be solved either by a brute force method or by employing an intelligent minimization scheme. The G-S equation can be written in the following form to designate the iterative process (showing only

the inner loop):

$$\Delta^* \psi^{k+1} = -\mu_0 R^2 P'(\psi^k, \alpha_n^k) \tag{6.9}$$

$$P'(\psi^k, \alpha_n^k) = \sum_{n=1}^{N_p} \alpha_n^k \Theta_n(\psi^k) \ , \tag{6.10}$$

where $P' \equiv \frac{dP}{d\psi}$, α's are the free parameters associated with the pressure model, and P' has been written as a general expansion of basis functions Θ's. In general, choosing a pressure model means choosing the Θ's. Once the pressure model is chosen, we can proceed with the iteration algorithm.

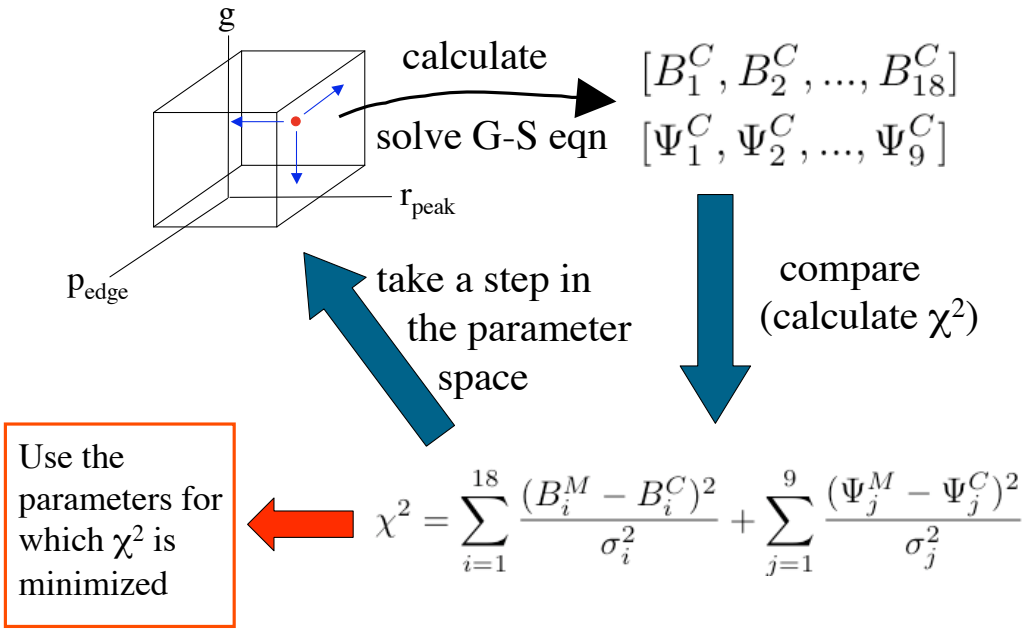

Figure 6-1: A flowchart of the reconstruction algorithm. The free parameters are varied until the best fit, designated by the minimum χ^2, is found. The C and M in the superscript stands for calculated and measured, respectively. The pressure model introduced in Ch. 3 is used as an example.

Figure 6-1 shows how the best fit pressure parameters are found. The free parameters are varied in the parameter space until the best agreement between the calculated fields and fluxes and measured fields and fluxes is found. The degree of the agreement is quantified by a merit function called χ^2,

$$\chi^2 = \sum_{i=1}^{18} \frac{(B_i^M - B_i^C)^2}{\sigma_i^2} + \sum_{j=1}^{9} \frac{(\psi_j^M - \psi_j^C)^2}{\sigma_j^2} \ . \tag{6.11}$$

The difference between the measured and calculated values for each detector is normalized by its measurement error. Hence, a χ^2 value of less than the total number of detectors would designate a very good fit.

Upon finding the best fit pressure parameters, various equilibrium quantities may be found fairly easily. The solution to the G-S equation using the best fit parameters gives us $\psi(R,Z)$, from which $\boldsymbol{B}(R,Z)$ can be obtained by taking its gradient and crossing it with a unit vector in the toroidal direction. The magnetic flux itself gives us the plasma shape and position. The pressure profile $P(R,Z)$ is found simply by plugging in the best fit parameter values to the pressure model and using $\psi(R,Z)$. Knowing both the field and pressure profiles allows us to find the beta profile, $\beta(R,Z) = \frac{2\mu_0 P(R,Z)}{B^2(R,Z)}$. Peak and average betas are easily calculated from $\beta(R,Z)$. The current profile can be calculated from either $\psi(R,Z)$ using Ampere's law or $P(\psi)$ using the G-S relation,

$$J_\phi = -\frac{1}{\mu_0 R}\Delta^*\psi = R\frac{dP}{d\psi} \ . \tag{6.12}$$

The G-S equation has to be solved multiple times for each outer iteration, and the process can consequently become computationally intensive. The brute force method of finding the set of parameters that minimizes χ^2 is to systematically scan the parameter space within a plausible domain and choose the set that yields the minimum χ^2. If the range of parameter α_n is R_n and its resolution r_n, the number of steps in the outer iteration would be $\prod_{n=1}^{N_p}(\frac{R_n}{r_n}+1)$, which can be quite large. Without having a general knowledge of the operational regime in the parameter space, the resolution of each parameter must be kept coarse to cover a wide range without expending too much computing time. Once the likely operational regime is discovered (through experience), the resolution can be refined to pinpoint the best fit. As cumbersome as

this method is, it is very useful in grasping the trend of χ^2 as different parameters are varied. Because χ^2 is evaluated at every point on the domain grid, defined by the range and resolution of each parameter, the χ^2 hypersurface is mapped out in an $(N_p + 1)$-dimensional space. This kind of mapping is very helpful in studying the characteristics of a pressure model.

A more sophisticated approach to finding the minimum χ^2 is to use some kind of an intelligent minimization scheme. There are a myriad of such schemes, like the singular value decomposition method [25, 40], grid search method, and gradient search method [2], and each method has its advantages and disadvantages. A particularly easy routine to implement with the existing reconstruction code is called the downhill simplex method, otherwise known as the amoeba method [40]. The amoeba method has the advantage that it does not require the computation of the derivatives, but it requires more function evaluations than some of the other methods. As with all intelligent minimization schemes, this method is susceptible to converging to a local minimum. This is especially true if the initial starting point is chosen close to such a minimum and the scope of the search is limited to a small neighborhood around it. The problem can usually be overcome by widening the domain of the search. For this and other reasons, it is a good idea to perform some reconstructions using the brute force method to get a feel for the behavior of χ^2, especially when a new pressure model is used or when a different operational regime is reached.

6.2.2 Vacuum Reconstruction

As seen in the previous subsection, the full reconstruction method can become cumbersome and computationally demanding. LDX has a unique magnetic field structure that allows us to forgo the proper computation and obtain accurate equilibrium results using vacuum field calculations [32]. This fortuitous situation is a direct consequence of the plasma current structure in the dipole geometry. Not only is the plasma current in the same direction as the dipole current, its magnitude is typically less than 0.5 % of the dipole current magnitude. Consequently, the magnetic flux in the presence of the plasma closely resembles the vacuum flux. In fact, for a plasma current of about

3.5 kA with a reasonable distribution and a dipole current of about 1.2 MA, the difference between the plasma and vacuum fluxes is less than 3 % at every point. This allows us to forgo the G-S equation and simply use the vacuum flux to calculate the plasma current, from which the fields and fluxes at the sensor locations are calculated to find the best fit,

$$J_\phi = R\frac{dP}{d\psi} \approx R\frac{dP}{d\psi^{vac}} \ . \tag{6.13}$$

Although the vacuum approximation brings about a small inconsistency since $\Delta^*\psi^{vac} = 0$, it is legitimate as long as the plasma current does not exceed about 1 % of the dipole current.

The procedure to find the best fit pressure parameters now becomes very computationally facile, involving only integrals and derivatives. Once the vacuum field is found and pressure model chosen, the free parameters are varied to find the minimum χ^2. The algorithm looks identical to Figure 6-1 except for substituting "solve G-S eqn" with "evaluate $R\frac{dP}{d\psi^{vac}}$ and use Ampere's law to calculate B and ψ." Being able to use the vacuum approximation in reconstructing LDX plasmas gives us the ability to reconstruct plasmas in real time without having to go through a fancy code like rtEFIT [7, 12].

6.3 Pressure models

The pressure models are the crux of the reconstruction process. They incorporate the physics of plasma transport and wave absorption. Although plausible forms of pressure models for a given confinement device may be found by doing extensive transport studies, more often than not some set of basis functions is just chosen . By definition, basis functions span the function space, so any set of basis functions can technically represent any pressure profile. What distinguishes a good choice of basis functions from a bad choice is the number of terms required to adequately represent the pressure profile. For example, if the pressure profile contains a decaying asymptote, the set of polynomials would require more terms than the set of hyperbolic functions. Amongst other reasons, having too many number of terms should be

avoided since it can under-constrain the minimization process to the point where there will be multiple minima of which merit cannot be distinguished. It is therefore wise to carefully choose the pressure model based on the expected shape and form of the pressure profile.

6.3.1 Isotropic models

Pressure models can be isotropic or anisotropic. Obviously, isotropic models are simpler because there is no distinction between $P_\perp$ and $P_\parallel$. Three isotropic models that have been used in reconstructing LDX plasmas are discussed in this section.

The first model called the DipoleEq profile is the one that was introduced in Ch. 3 and is the most frequently used,

$$P(\psi;\psi_{peak},P_{edge},g)=\begin{cases} P_{edge}\left[\frac{V_{edge}}{V(\psi)}\right]^g & \text{for } \psi>\psi_{peak} \\ P_{edge}\left[\frac{V_{edge}}{V(\psi)}\right]^g \sin^2\left[\frac{\pi}{2}\left(\frac{\psi}{\psi_{peak}}\right)^2\right] & \text{for } \psi<\psi_{peak} \end{cases} . \quad (6.14)$$

Having discussed the marginal MHD stability criterion in Ch. 5, it is quite easy to see why a pressure model in the above form is suitable to describe LDX plasmas. The marginal criterion sets the maximum slope of the pressure profile according to $PV^\gamma = P_{edge}V_{edge}^\gamma$ between the pressure peak and the wall ($\psi > \psi_{peak}$). If we assume that the plasma is heated quickly enough that it is always in the vicinity of the marginal limit, then the profile should fit the model quite well. Even if the plasma is not close to the marginal limit, the slope parameter g is left free to be constrained by magnetic measurements so that the profile can nevertheless be fitted to the model satisfactorily. The region between the floating coil edge and the pressure peak is modeled so that the profile rises sinusoidally from the coil edge to the peak and continuously transitions to the profile on the other side of the peak. One noticeable flaw of this model is that the first derivative of the profile is discontinuous at the pressure peak. This makes the profile unrealistically cuspy at the peak, potentially giving spurious peak and average beta values. However, the model correctly gives a finite pressure at both the inner limiter (the floating coil) and outer limiter (the vessel wall). In fact the MHD stability of LDX plasmas depends on the fact that there is

finite pressure at the outer wall.

One may ask if this pressure model based on the MHD stability criterion is still suitable for LDX plasmas with a significant fraction of hot electrons. As was discussed in Ch. 5, hot electrons are not subject to the MHD criterion. Hot electrons will still adhere to profile shapes that are generally consistent with those given by the model. It is also of interest to see by how much hot electrons can exceed the MHD gradient limit by finding their best fit g parameter.

The second isotropic model, which we call the "no edge pressure profile," is very simple and has been used only once for comparison purposes,

$$P(\psi; a, b, g) = \frac{a}{V^g}(\psi_{max} - \psi)^b(\psi - \psi_{min})^c \ . \tag{6.15}$$

The model has the familiar V^{-g} factor, but there also are two factors in the numerator that make the pressure go to zero at the inner and outer limiters. A closer inspection of the form of the model reveals that it is actually a polynomial model of degree $4g+b+c$ with repeated free parameters (i.e. the coefficients of different terms depend on each other). The coefficients of the polynomial are set up so that the pressure vanishes at the limiters. The unphysicality of the vanishing pressure at the edges is somewhat compensated by the more physically realistic continuity of the first derivative at the pressure peak.

The third and final isotropic model that has been used is called the "smooth adiabatic profile." This model is an attempt to retain the stability dependent profile of the first model while eradicating its unphysical cusp at the pressure peak,

$$P(\psi; \psi_{peak}, P_{peak}, g) = P_{peak}\left(\frac{\psi - \psi_{f-coil}}{\psi_{peak} - \psi_{f-coil}}\right)^{\alpha}\left(\frac{\psi}{\psi_{peak}}\right)^{4g} \ , \tag{6.16}$$

where $\alpha \equiv 4g(|\frac{\psi_{f-coil}}{\psi_{peak}}| - 1)$. The stability dependent V^{-g} factor is hidden in the ψ^{4g} factor. Although this model still makes the pressure vanish at the inner limiter, the smoothness of the pressure peak potentially makes us to believe it the most realistic of all.

6.3.2 An anisotropic model

Plasmas in LDX are heated by electron cyclotron resonance heating (ECRH), as mentioned in Ch. 1. Because ECRH preferentially accelerates electrons in the direction perpendicular to the field lines, they naturally gain more kinetic energy in the perpendicular direction than in the parallel direction. This leads to the plasma having an anisotropic pressure with $P_\perp > P_\parallel$. To capture the physics of the anisotropic pressure, a pressure model that incorporates the anisotropy must be employed in the reconstruction process. Before we can discuss a specific anisotropic pressure model, MHD equilibrium must be revisited to understand how the current-pressure relationship changes due to the anisotropy. The treatment of anisotropic equilibria is given in many books, including the one by Hazeltine and Meiss [17].

The only relevant equation that is altered in the MHD model to account for the anisotropy is the momentum equation,

$$\boldsymbol{\nabla} P = \boldsymbol{J} \times \boldsymbol{B} \quad \Longrightarrow \quad \boldsymbol{\nabla} \cdot \boldsymbol{P} = \boldsymbol{J} \times \boldsymbol{B} \ , \tag{6.17}$$

where $\boldsymbol{P}$ is the pressure tensor. With this modification, the current becomes,

$$\boldsymbol{J} = \frac{\boldsymbol{B} \times \nabla \cdot \boldsymbol{P}}{B^2} = \frac{\boldsymbol{B} \times \nabla P_\perp}{B^2} + \frac{\boldsymbol{B} \times \boldsymbol{\kappa}}{B^2}(P_\parallel - P_\perp) \ , \tag{6.18}$$

where $\boldsymbol{\kappa} = \boldsymbol{b} \cdot \nabla \boldsymbol{b}$ is the magnetic curvature. When compared to the isotropic case, an extra term that depends on the anisotropy of the pressure is present. In the low beta (or vacuum) approximation, Eq. 6.18 can be rewritten as [35],

$$J_\phi = R\frac{\partial P_\perp}{\partial \psi} + R(P_\parallel - P_\perp)\frac{\partial \ln B}{\partial \psi} \ , \tag{6.19}$$

where the chain rule $\frac{\partial}{\partial \psi} \equiv |\nabla \psi|^{-2} \nabla \psi \cdot \nabla$ and the vacuum curvature approximation $\kappa \approx \frac{\nabla_\perp B}{B}$ have been used. Notice that $P_\perp > P_\parallel$ everywhere in the ECRH heated plasma and $\frac{\partial \ln B}{\partial \psi} > 0$ outside the pressure peak. The second term of J_ϕ is therefore negative. This is a significant result because for a given measurement of J_ϕ, the anisotropic model predicts a larger $\frac{\partial P_\perp}{\partial \psi}$ than the isotropic model. Accordingly, the anisotropic model gives a higher beta for a given measured current. To find an anisotropic equilibrium, one needs only to apply the desired pressure model to the above equation.

The anisotropic model that has been developed for anisotropic pressure reconstruction is a modification of the "smooth adiabatic profile."[36] Now that the pressure is anisotropic, it is not only a function of ψ but is a function of B as well,

$$P_\perp = G(\psi;\psi_{peak},P_{peak},g)H[B(\psi,\chi);p] \tag{6.20}$$

$$G(\psi) \equiv P_{peak}\left(\frac{\psi-\psi_{f-coil}}{\psi_{peak}-\psi_{f-coil}}\right)^{\alpha}\left(\frac{\psi}{\psi_{peak}}\right)^{4g} \tag{6.21}$$

$$H(B) \equiv \left(\frac{B_0}{B}\right)^{2p} . \tag{6.22}$$

This model was originally developed by Connor and Hastie [5, 22, 45] and incorporates the anisotropy parameter $p \equiv \frac{P_\perp - P_\parallel}{2P_\parallel}$. In the model, χ is the magnetic scalar potential ($\boldsymbol{\nabla}\chi = \boldsymbol{B}$) which serves as the "angular" component of the magnetic coordinate system, and $B_0 \equiv B(\psi,\chi=0)$ is the minimum field strength on a field-line. The function $G(\psi)$ is precisely the "smooth adiabatic profile," and the anisotropy is incorporated by multiplying this by a function $H(B)$ that depends on B and p only. The H function's role is to progressively localize the pressure to the midplane as it becomes more anisotropic. Physically, the electrons become more deeply trapped and confined near the midplane as their pressure becomes more anisotropic and the ratio $\frac{v_\perp}{v_\parallel}$ increases. The anisotropy parameter p generally varies in space, but it is kept spatially uniform in the Connor-Hastie model to make the analysis more tractable.

6.4 Sensitivity of the magnetic measurements to the lowest order moment

6.4.1 Evidence

Magnetic field in a current-free region can be written as a gradient of the scalar potential [38],

$$\boldsymbol{B} = -\boldsymbol{\nabla}\eta \ , \tag{6.23}$$

where η is the magnetic scalar potential. Furthermore, the scalar potential can be expanded as a sum of Legendre polynomials, or equivalently, spherical harmonics as

follows:

$$\eta = \sum_l A_l r^{-(l+1)} Y_{l0}(\theta) \ . \tag{6.24}$$

The 2^l-pole moment is represented by A_l, and $r^{-(l+1)}$ gives its radial dependence (in spherical coordinates). It is evident that the higher order moments quickly vanish as one moves away from the current source. Because $A_0 = 0$ (no monopole), the dipole moment dominates at large distances.

As mentioned earlier in the chapter, equilibrium reconstruction is heavily dependent on the characteristics of the machine. One unwanted but inevitable feature of the magnetic diagnostics in LDX is that the external sensors are located far away from the plasma. The large vacuum chamber is designed to confine a relatively small plasma, so the external sensors are necessarily distant from the current source. In the context of the previous paragraph, this means that the sensors may not have sufficient sensitivity to measure anything beyond the dipole moment of the plasma current.

In addition to the sensors being far from the plasma, the measurement of the next lowest moment—the quadrupole moment—is dominated by the contribution from the floating coil. As discussed earlier, the B_p coils and flux loops pick up the sum of the plasma current and the floating coil current decrease. Because the plasma current and the current decrease are in opposite directions, it contributes significantly to the total quadrupole moment. In conjunction with the far distance of the detectors, measuring the plasma quadrupole moment becomes an arduous, if not impossible, task. Capturing the higher order moments is even more difficult.

One key evidence that the magnetic sensors are sensitive only to the plasma dipole moment comes from studying the results from the DFIT code. Given a plasma shot, DFIT finds the best fit magnitudes and locations of the two current filaments. Figure 6-2 shows a contour plot of chi-squared as a function of the current magnitudes of the two filaments at fixed positions for shot 50318014. The black dot designates where the minimum chi-squared contour (not shown) is. The blue line that intersects the dot is a contour of a fixed dipole moment. The significance of this plot is that the contour of the fixed dipole moment approximately overlays the contour of minimum

chi-squared. In other words, the magnetic sensors cannot distinguish between different combinations of currents in the two filaments if they have the same dipole moment.

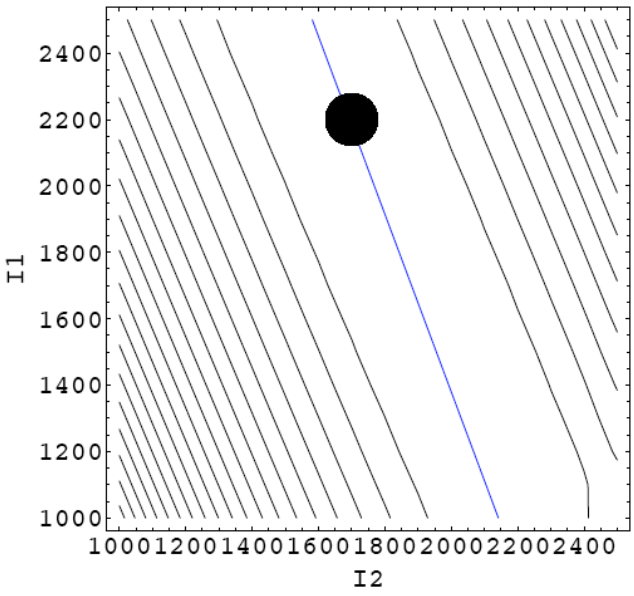

Figure 6-2: A contour plot of chi-squared as the currents in the two filaments are varied. The contour of minimum chi-squared is not shown but should be where the black dot is. Instead, a contour of a fixed dipole moment is shown in its place. The fact that the two contours roughly overlay each other shows that the magnetic sensors are sensitive only to the dipole moment.

The magnetic diagnostics' sensitivity to the dipole moment is also corroborated from reconstruction results using the first pressure model described in the chapter. The model has edge pressure, peak position, and profile slope as the free parameters. The behavior of chi-squared has been studied as the parameters are varied. It has

been found that for a fixed peak position ψ_{peak}, there is a definite absolute minimum of chi-squared as a function of P_{edge} and g (Figure 6-3). However, if all these minima for different peak positions are plotted as a function of ψ_{peak}, there does not seem to be a trend from which a definite minimum can be extracted. Of course, there is an absolute minimum, but the absolute minimum does not seem to have any more merit than the other minima for different peak positions.

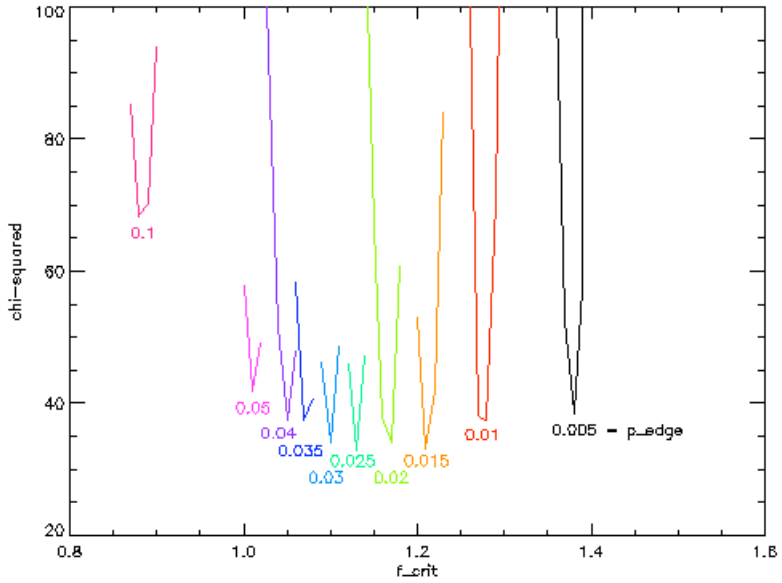

Figure 6-3: Plots of chi-squared as a function of P_{edge} and $g = \frac{5}{3} f_crit$ with a fixed ψ_{peak}. For each P_{edge}, there is a g that minimizes chi-squared. Plotting these minima vs. P_{edge} gives an absolute minimum of chi-squared as a function of the two variables.

It has been found that for a fixed peak position, the dipole moment is unique for a unique combination of P_{edge} and g. That is, the function $M(P_{edge}, g)$, where M is the

dipole moment, is an injection (one-to-one). However, if the third parameter ψ_{peak} is included as another variable, M is no longer one-to-one. Furthermore, if P^I_{edge} and g^I minimize χ^2 for $\psi_{peak} = \psi^I_{peak}$, and P^{II}_{edge} and g^{II} minimize χ^2 for $\psi_{peak} = \psi^{II}_{peak}$, and $[\chi^2]^I \approx [\chi^2]^{II}$, then

$$M(P^I_{edge}, g^I, \psi^I_{peak}) \approx M(P^{II}_{edge}, g^{II}, \psi^{II}_{peak}) \ . \tag{6.25}$$

Again, it seems like the magnetic measurements have a difficult time deciphering between different sets of parameters that have the same dipole moment.

A simulation has been conducted using phantom data to see if putting internal sensors—flux loops located close to the plasma—can help in resolving different sets of parameters with the same dipole moment [19]. The anisotropic model with $p = 2$ and a constant P_{peak} is used, and chi-squared is mapped as ψ_{peak} and g are varied. Figure 6-4 shows the results with and without the internal flux loops. It is clear that the external sensors alone cannot produce a minimum in the (ψ_{peak}, g) plane, but adding the internal loops creates a minimum. Hence, the addition of internal sensors may be required to measure current profile details beyond the dipole moment.

6.4.2 Using x-ray data to help constrain the parameters

X-ray emissivity data can be used to constrain the peak pressure location [19]. Figure 6-5 shows the pressure contours superimposed on a horizontal view of the plasma and the floating coil for 2.45 GHz only and 6.4 GHz only heating. The images from the x-ray camera [46] showing the line integrated emissivity are also superimposed on the visible light pictures. Since the pressure results almost entirely from energetic trapped electrons, the x-ray image is expected to be well correlated with the peak pressure profile. Abel inversion of the x-ray images as well as the light emission during the afterglow period (after the microwave power has been switched off) are consistent with the pressure peak located at the fundamental cyclotron resonance of the injected microwaves.

The pressure contours are centered about the pressure peak location. The peak pressure occurs closer to the floating coil when only 6.4 GHz heating is applied com-

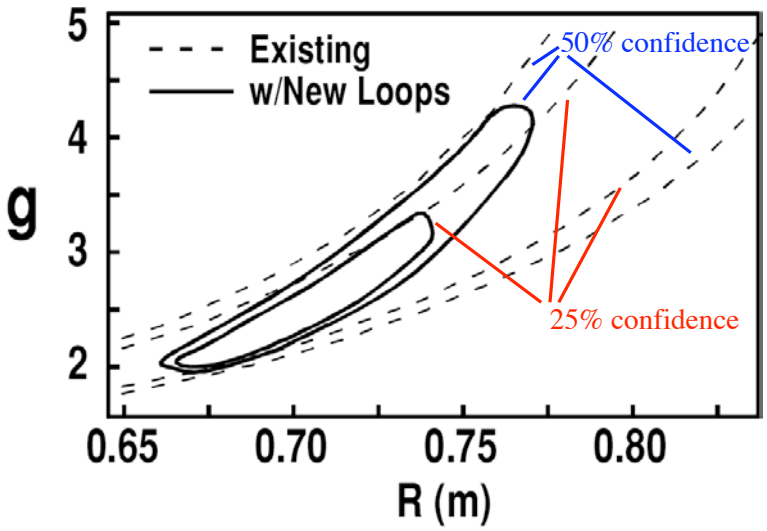

Figure 6-4: Chi-squared contours in the (ψ_{peak}, g) plane. The dotted lines are the contours for the external sensors only, and the solid lines are the contours for the external sensors plus internal flux loops. The x-axis of the figure (R) designates the radius of the pressure peak, which is qualitatively equivalent to the flux at the pressure peak (ψ_{peak}). The minimum is unambiguous only when the internal loops are present.

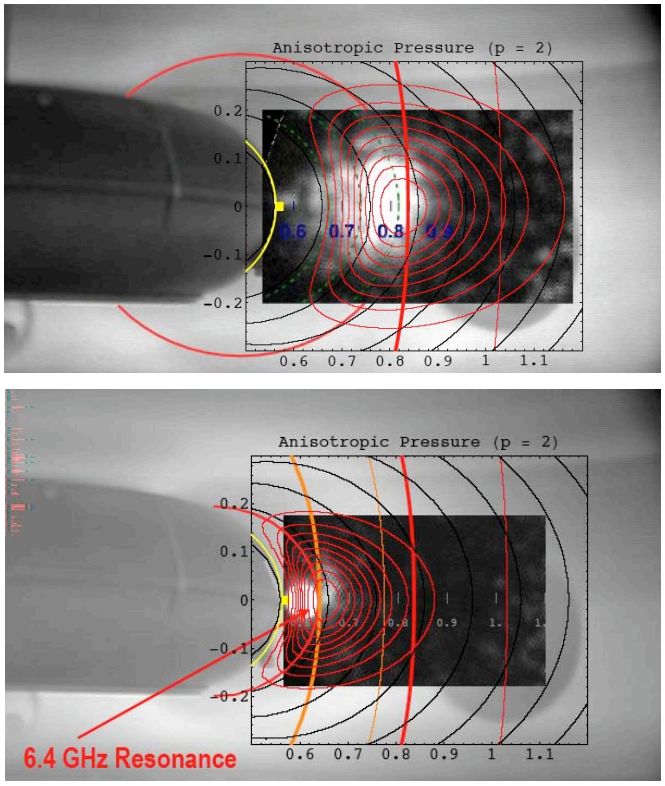

Figure 6-5: Contours of the reconstructed pressure profiles superimposed onto the x-ray images measured during (top) 2.45 GHz heating and (bottom) 6.4 GHz heating.

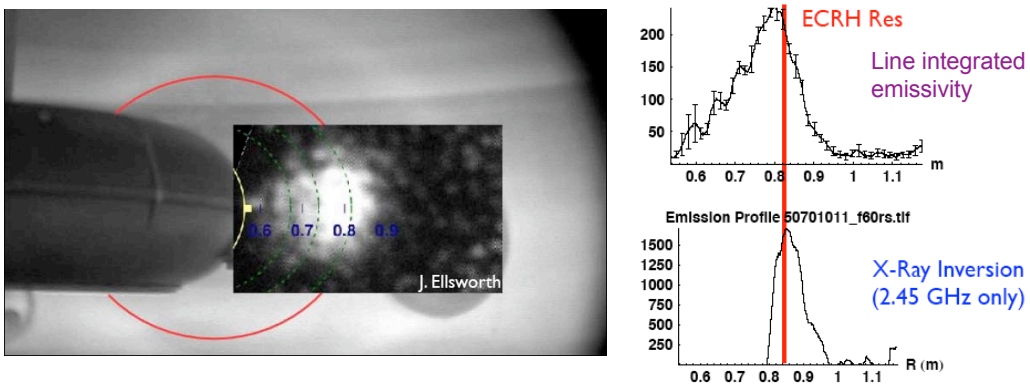

Figure 6-6: An x-ray image for 2.45 GHz only heating (left), its line integrated emissivity (right top), and its Abel inversion (right bottom).

pared to when only 2.45 GHz is used (Figure 6-6). When the two frequencies are combined, the pressure peaks in between the two fundamental resonance locations. Since the pressure model constrains the plasma to have a single pressure peak, it is unclear whether there is a single peak in between the two resonance locations or a local peak at each location. It is interesting to note that χ^2 for the combined heating case is about twice that for the single frequency heating case. It may be that the single peak model is inadequate for describing an LDX plasma heated by more than one frequency.

The effect of anisotropic pressure is also evident in these contour pictures. The pressure contours do not coincide with flux contours, and the pressure becomes more localized to the midplane as it becomes more anisotropic. This is in stark contrast to an isotropic pressure, whose magnitude is independent of the magnetic angular coordinate χ.

Once the peak pressure location is constrained by the Abel inverted x-ray emissivity, chi-squared can be minimized without any equivocality. Equivalently, the plasma current can be resolved beyond its dipole moment by deducing it from the pressure using MHD relations. Using kinetic data, such as temperature and pressure measurements, in conjunction with magnetic data is a common practice in better constraining pressure parameters.

Chapter 7

Typical Shots

This chapter describes the typical LDX plasma shots. Although every shot is unique to some degree, there are a lot of commonalities that are shared amongst all the shots. Specifically, most of the shots have three distinct plasma regimes that are clearly distinguished by the measurements from different diagnostics. The three regimes will be described in detail throughout the chapter. Also, magnetic data will be used to reconstruct some shots using the different pressure models described in the previous chapter.

7.1 Characterization of the three regimes

A typical LDX discharge is shown in Figure 7-1. In this shot, 2.5 kW each of 2.45 and 6.4 GHz microwaves is used to heat the plasma. The figure shows measurements from some of the key diagnostics installed on the machine. The discharge is divided into three time intervals, each interval corresponding to a different plasma regime [9]. The first time period from 0 to about 0.25 sec is called the low density regime. The middle interval from about 0.25 to 4 sec is referred to as the high beta regime. The final interval from 4 sec to infinity is the after-glow regime. Each of these regimes will be explained in the following subsections.

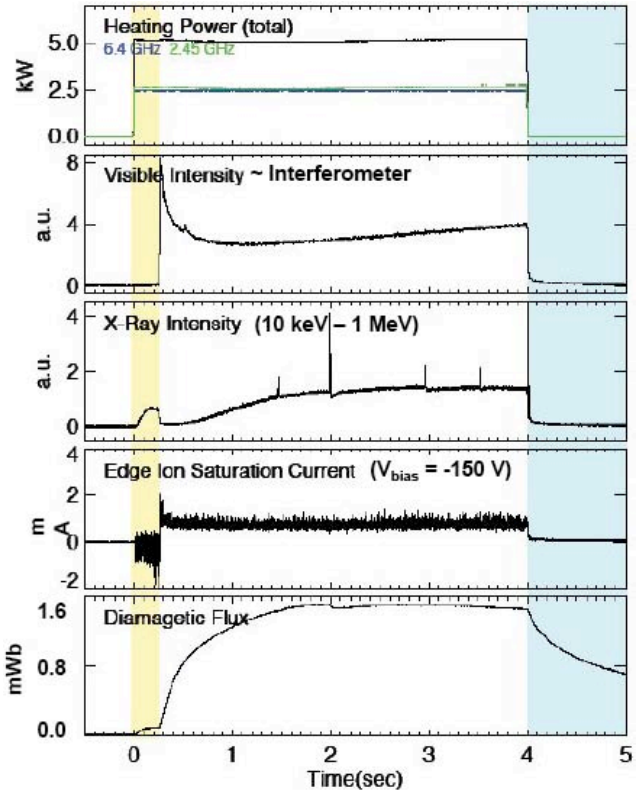

Figure 7-1: Signals from various diagnostics showing the evolution of a typical LDX discharge (shot 50317014). The three plasma regimes are marked by different colors. The pale yellow region is the low density regime, white is the high beta regime, and the light blue region is the after-glow regime.

7.1.1 Low density regime

Most plasma shots in LDX start off with the low density regime. As its name implies, the regime is characterized by low bulk plasma density. Hot electrons are rapidly created by ECRH heating, but they have not had enough time to collide with neutrals to produce a significant population of bulk electrons. The visible light intensity is roughly proportional to the bulk plasma density, and the visible light detector does not register any signal during this period. The line-averaged electron density is about 2×10^{16} m^{-3} as measured by the single chord interferometer.

The plasma is highly unstable during the low density regime. As seen in Ch. 5, the plasma can become unstable to the hot electron interchange mode when $\frac{\bar{n}_i}{\bar{n}_h}$ gets too low. The evidence of the instability is most lucidly manifested in the edge ion saturation current measurement during this period. Despite the probe being negatively biased at -150 V, it measures a significant negative current, which is consistent with outward bursts of energetic electrons. The NaI detector, which has a radial view that includes the floating coil, sees bursts of x-rays that are most likely due to hard target Bremmstrahlung from inward moving electrons hitting the coil. When the instability bursts become intense, sparks can be seen on the video camera caused by energetic electrons removing dust and debris from the floating coil and other solid structures (Figure 7-2). Visible light images show a small, localized plasma surrounding the floating coil. The small plasma cannot support enough diamagnetic current to give a significant flux, as indicated by the low reading on the flux loop.

7.1.2 High beta regime

The low density regime transitions to the high beta regime when the neutral pressure exceeds a critical value which depends on the microwave heating power and the outer shape of the plasma. The bulk density climbs rapidly to nearly ten times that during the low density regime, and the HEI is consequently quelled. The suppression of the HEI is evidenced by the cessation of target x-ray signals and the acquiring of a positive ion saturation current by the edge probe. The increase in the bulk density

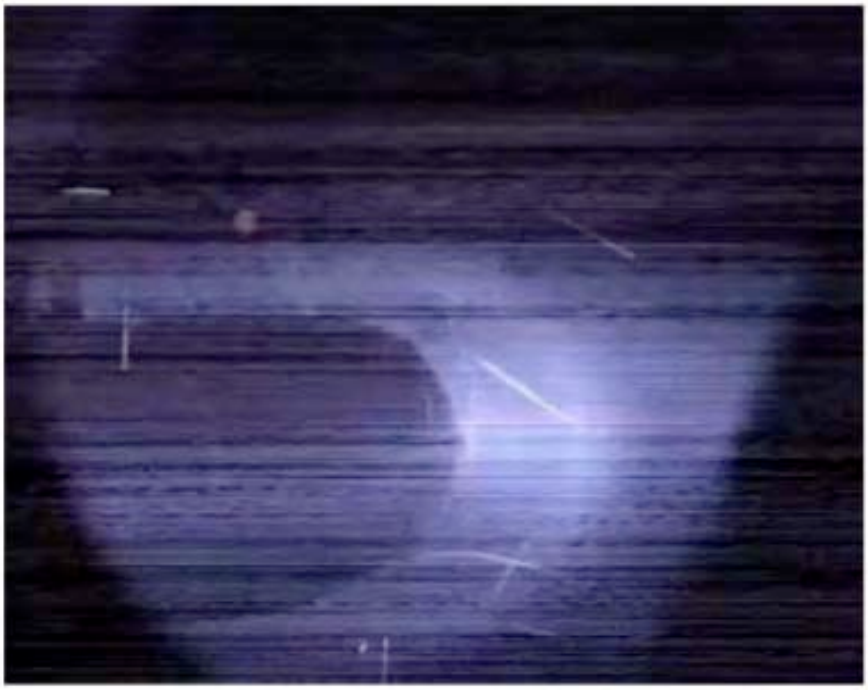

Figure 7-2: A video image showing flying debris caused by energetic electrons hitting solid structures during the low density regime.

allows the hot electron population to build up as well. The DFIT reconstruction shows that the current centroid moves outward (Figure 7-3) as the plasma transitions from the low density to high beta regime, indicating a growth in the plasma volume. As shown by the flux loop signal, there is a rapid increase in the diamagnetism, which is a rough measure of the pressure and beta. Broad low frequency fluctuations can be seen on the Mirnov and edge probes throughout the period indicating some sort of MHD activities (Figure 7-4).

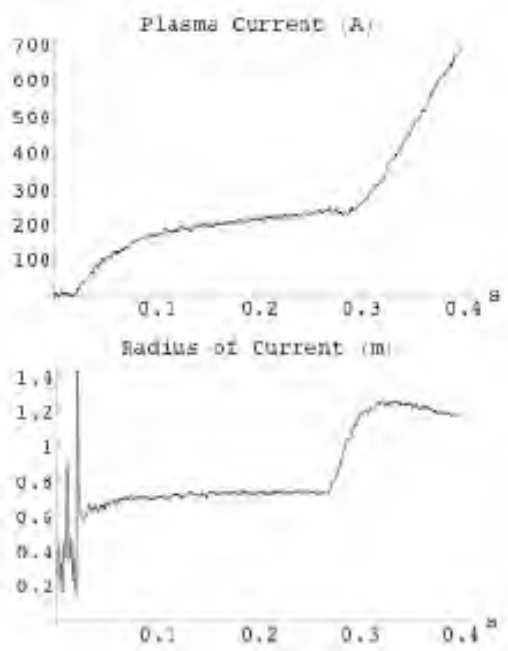

Figure 7-3: The DFIT code result showing the current centroid moving outwards as the plasma transitions from the low density to high beta regime.

Although the high beta regime is relatively quiescent, periodic relaxation events are observed a few times a second on the flux loop measurement. The relaxation events consist of beta dumps accompanied by spikes in the x-ray signal. There usually

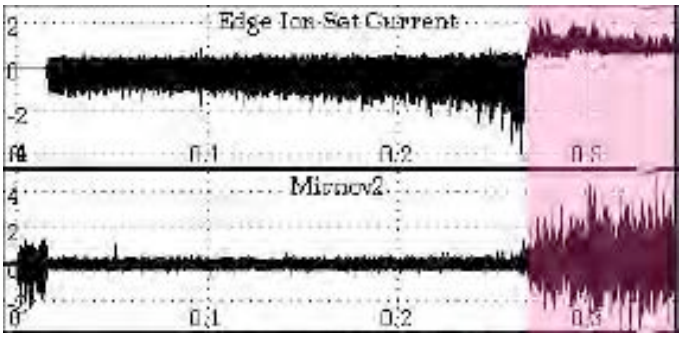

Figure 7-4: An increase in broad spectrum fluctuations can be seen on the Mirnov and edge probe signals as the plasma enters the high beta regime. The edge probe clearly acquires a positive current after the transition.

is an outward movement of the current ring during these events as well. They are believed to be HEI's caused by exceeding the marginal density gradient. The plasma temporarily relaxes its profile, but the continual heating causes the profile to steepen again until the next event happens. The relaxation events are minor in this typical shot example, but they can be fully disruptive depending on the neutral fueling and heating power. LDX is the first experiment to observe the HEI in a high beta dipole plasma.

A video image of the high beta regime is shown in Figure 7-5. The image shows a stable and quiescent plasma, which is in stark contrast to the tumultuous plasma of the low density regime. Table 7.1 lists some key equilibrium parameters during a typical high beta regime.

7.1.3 Afterglow regime

The afterglow regime follows the high beta regime and occurs subsequent to the turnoff of the RF power. The bulk electrons are quickly lost, and the diamagnetism decays slowly over many seconds. The hot electrons persist for a while, creating a halo around the floating coil. The afterglow regime can be susceptible to the HEI since the bulk population is lost much more quickly than the hot electrons. An HEI event during the afterglow regime almost always leads to a complete annihilation of the plasma. A picture of the afterglow regime is shown in Figure 7-6.

7.2 Equilibrium reconstruction of the typical shot

This section goes through the procedure discussed in Ch. 6 to reconstruct the shot (50317014) shown in Figure 7-1 during the high beta regime. The full reconstruction technique using the G-S solver is demonstrated. The DipoleEq (isotropic) pressure model is employed in the code.

The first step is to obtain the best fit floating coil current from the Hall probe measurements. The best fit current is found by using the G-S solver with zero pressure, which effectively reduces the code to a Biot-Savart solver. The best fit current

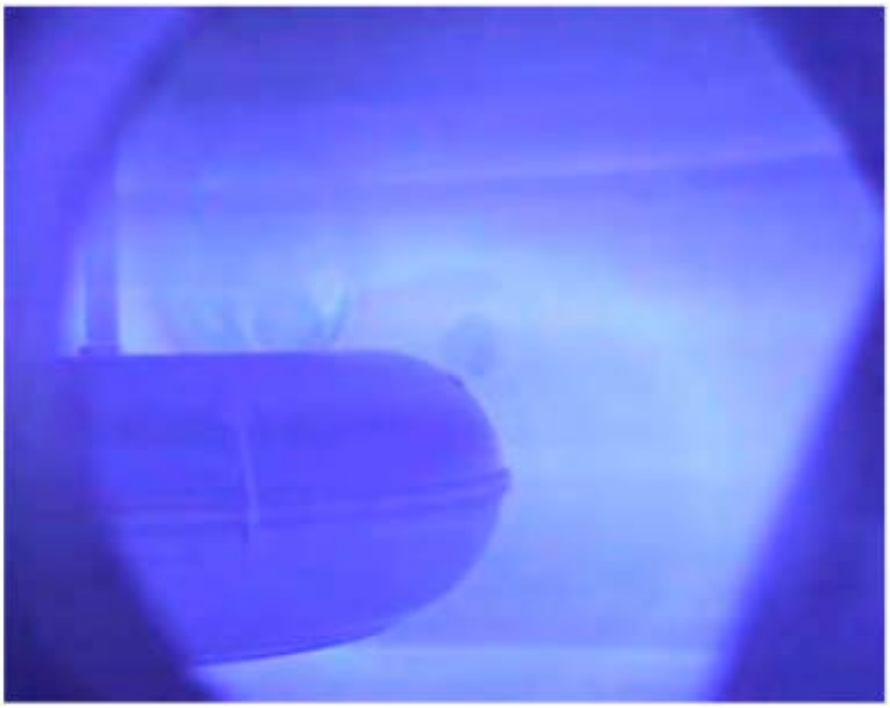

Figure 7-5: A video image of the high beta regime plasma. The plasma is much more tranquil compared to that during the low density regime.

Equilibrium parameters	Value
Dipole current (MA)	0.93
2.45 GHz power (kW)	2.5
6.4 GHz power (kW)	2.5
Plasma stored energy (J)	330
Plasma volume (m^3)	29
Plasma current (kA)	3.5
Current centroid (m)	1.2
Plasma dipole moment ($kA \cdot m^2$)	4.8
Dipole current change (kA)	-0.80
Pressure peak location, R_{peak} (m)	0.72
Adiabatic profile parameter, g	2.8
Anisotropy, p	2
Peak beta (%)	21
Average beta (%)	1.7
Peak perpendicular pressure (Pa)	750
Hot electron temperature (keV)	100 - 250
Hot electron density (10^{16} m^{-3})	2 - 4
Line density (10^{19} m^{-2})	1.8
Edge electron temperature (eV)	10
Edge density (10^{16} m^{-3})	0.6 - 1.0

Table 7.1: Key equilibrium parameters during a typical high beta regime.

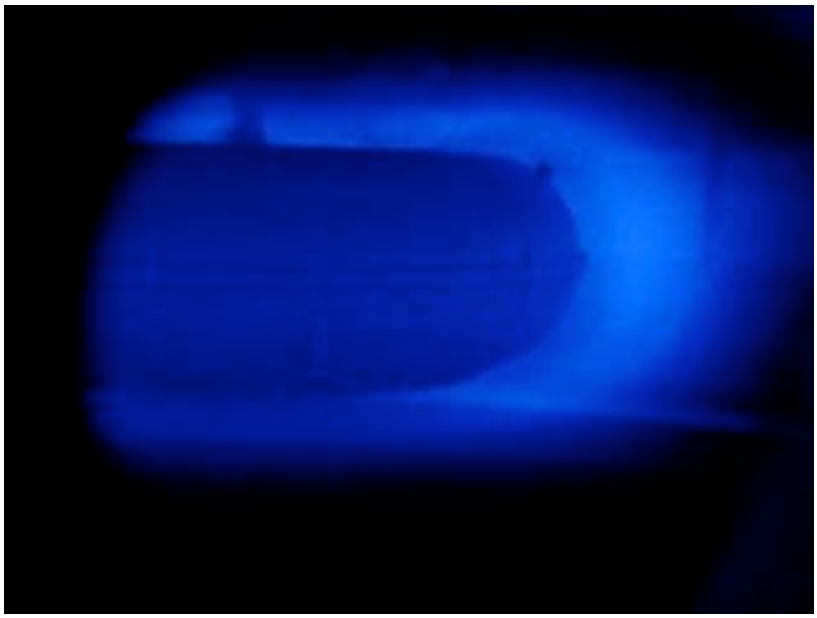

Figure 7-6: A video image of the afterglow regime. A bright halo of hot electrons is clearly visible around the floating coil.

Equilibrium parameters	Value
Pressure peak location (m)	0.77
Steepness parameter ($\times\frac{5}{3}$)	1.05
Peak pressure (Pa)	162
Peak beta (%)	6.4
Volume averaged beta (%)	1.4
Total stored energy (J)	121
Plasma volume (m^3)	28
Plasma current (kA)	2.1
Current centroid (m)	1.02
Plasma dipole moment ($kA \cdot m^2$)	7.5
Change in F-coil current (kA)	-1.0

Table 7.2: The equilibrium parameters of shot 50317014 calculated from the best fit pressure profile.

is 894000 A with $\chi^2 = 39$. Using this information, the vacuum field is calculated, and the total field or flux at each sensor position is found by adding the measurements from the B_p coils and flux loops to the vacuum field and flux.

Upon invoking the amoeba minimization scheme on the G-S solver, the minimum is attained for $R_{peak} = 0.77$ m, $P_{edge} = 0.030$ Pa, and $g = 1.06 \times\frac{5}{3}$ with $\chi^2 = 26$. Two of the detectors have been eliminated from the best fit since their measurements seem to read spurious values. The peak pressure location, R_{peak}, has been set to the location of peak x-ray emissivity, as discussed in Ch. 6, prior to the minimization, so the minimization has been done over the other two parameters. Table 7.2 lists the equilibrium parameter values calculated from the best fit, and Figure 7-7 shows the current, pressure, and beta profiles. The equilibrium flux contours are displayed in Figure 7-8.

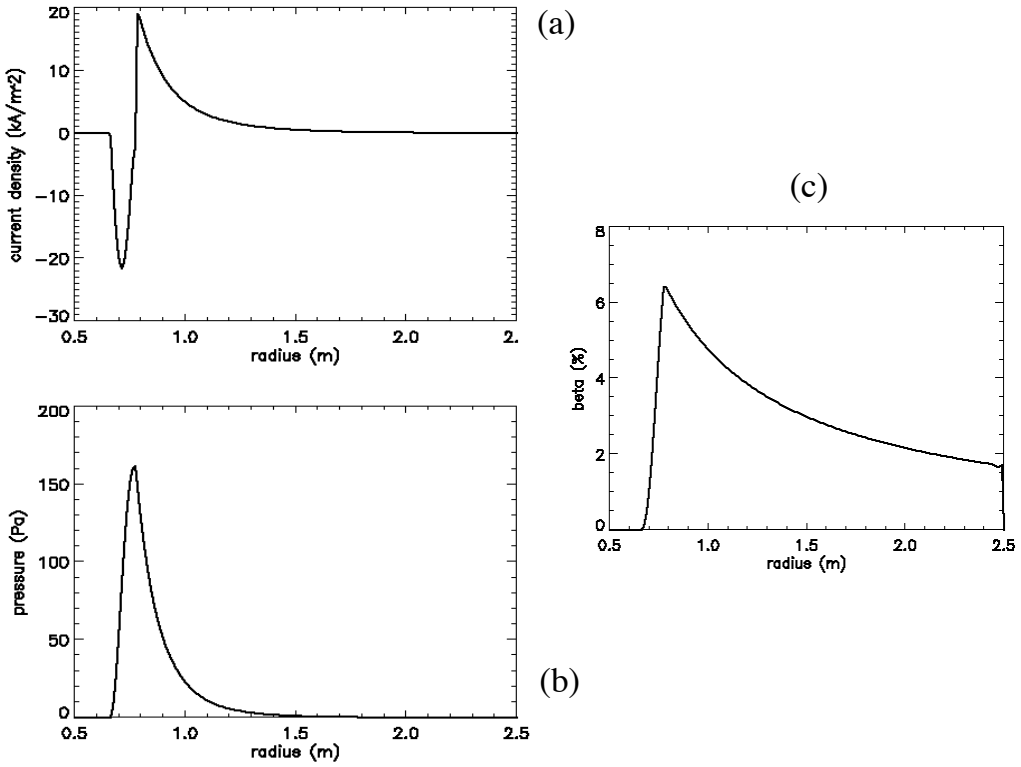

Figure 7-7: The best fit (a) current and (b) pressure profiles, and the resulting (c) beta profile.

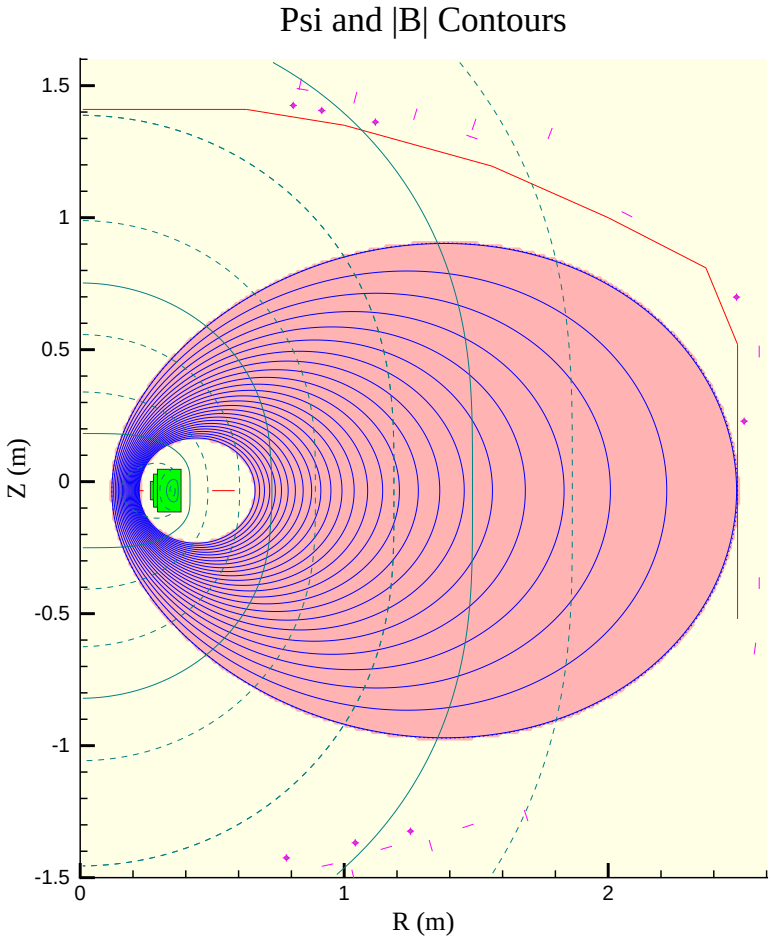

Figure 7-8: The equilibrium flux contours showing the shape of the plasma.

7.3 Comparison of the different pressure models

An example shot (50318014) has been reconstructed using the different pressure models discussed in Ch. 6 to compare the results. The vacuum reconstruction technique is used here. Figure 7-9 summarizes the results. The energy related values (such as average beta) and quantities related to the current profile are pretty comparable. In light of the argument that the magnetic sensors are sensitive only to the plasma dipole moment, the similarity in the current magnitude and centroid values amongst the three models may have been a slight coincidence. It would have been a plausible result for one of the models to have a larger (smaller) magnitude and smaller (larger) centroid than the other models as long as the dipole moments were comparable. The similarities in the energy values are a good result since they mean that the differences in the details of the profiles do not affect the integrated quantities like total energy and volume averaged beta too much. Although there is considerable variability in the peak pressure values, the peak beta values are reasonably (and surprisingly) close. It seems like the higher the peak pressure for a model is, the closer the peak is to the floating coil (where the field is higher). The importance of the peak beta value is open for debate, but it is reassuring that different models predict roughly similar values.

Parameters \ Model Type	**DipoleEq**	**No Edge Pressure**	**Smooth Adiabatic**
Peak pressure (Pa)	310	647	162
Peak beta (%)	11	9.5	8.4
Volume averaged beta (%)	1.6	1.2	1.3
Total stored energy (J)	290	236	247
Plasma current (kA)	3.3	3.0	3.1
Current centroid (m)	0.93	0.97	0.97
Change in F-coil current (kA)	-0.87	-0.76	-0.77

Figure 7-9: Comparison of the equilibrium parameters from three different pressure models.

Chapter 8

Special Shots

LDX has three different types of "knobs" that can alter the plasma in different ways. The first knob is the control of the microwave sources [14]. LDX plasma is heated by a 2.45 GHz magnetron and a 6.4 GHz klystron, and both of their powers can be adjusted up to 3 kW. The second knob is the control of the gas fueling. Different amounts of gas can be puffed into the chamber before and during plasma formation. The third and the final knob is the pair of Helmholtz coils, described in Ch. 1. The coils can impose different magnitudes of vertical field on the plasma and alter its size and shape. This chapter deals with the different effects "turning" these knobs have on the properties of the plasma.

8.1 ECRH Control

Electron cyclotron heating provides an effective way to produce plasmas in a dipole field. The microwaves are expected to be absorbed most strongly where the fundamental cyclotron frequency equals the wave frequency ($\omega = \omega_{ce}$) and $|\boldsymbol{B}|$ is tangent to $\boldsymbol{B}$, and there will be some absorption at the first harmonic ($\omega = 2\omega_{ce}$) location as well. Consequently, microwaves at different frequencies will preferentially heat at different locations, and there is a hope of achieving some degree of profile control by using different heating frequencies.

LDX is equipped with the two aforementioned heating frequencies. The 2.45

GHz has the fundamental resonance at 0.088 T and the 6.4 GHz has it at 0.229 T, neglecting relativistic effects. The corresponding locations on the midplane are 75 cm and 58 cm, respectively, at a floating coil current of about 900 kA. When the floating coil current is about 1.17 MA, which is the highest current achieved to date, the fundamental locations move outward to 81 cm and 62 cm, respectively. The first harmonic locations are 93 cm and 69 cm at 900 kA and 101 cm and 75 cm at 1.17 MA. The first harmonic locations of 6.4 GHz are always closer to the floating coil than the fundamental locations of 2.45 GHz. The field line at the fundamental location of 6.4 GHz at either floating coil current is actually intercepted by the inner surface of the floating coil, but the hot electrons are deeply mirror trapped and effective heating is nevertheless possible at the fundamental location.

An obvious experiment to perform to study the effects of different heating frequencies on the plasma is to modulate the power of one frequency while keeping the power of the other fixed. By performing two shots in which one frequency is modulated in the first and the other frequency is modulated in the second, all three possible scenarios (2.45 GHz only, 6.4 GHz only, and combined) may be explored. Shots 50318009 and 50318010 have been reconstructed for this purpose. Figures 8-1 and 8-2 show the ECRH powers and the signal from one of the flux loops for shots 50318009 and 50318010, respectively. The 6.4 GHz power is modulated in shot 50318009 whereas the 2.45 GHz power is modulated in shot 50318010. Qualitative differences in the flux loop response are evident for the two modulations. The 2.45 GHz power increases the flux more quickly than 6.4 GHz, but it seems to saturate at a somewhat lower level for 2.45 GHz. It is clear that the current for 2.45 GHz only (t = 0-2 sec) has saturated by the time 6.4 GHz comes on in shot 50318009, but that for 6.4 GHz only (t = 0-2 sec) has not saturated by the time 2.45 GHz comes on in shot 50318010. Also, the current quickly saturates when 2.45 GHz comes on (at t = 2 sec) in shot 50318010, whereas it does not reach saturation when 6.4 GHz comes on (at t = 2 sec) in shot 50318009 before it is turned off at t = 4 sec. The difference in the rate of current rise is evident for the two frequencies, but the difference in the flux saturation level may be due to the difference in the current centroid locations rather than the difference

in the current magnitudes.

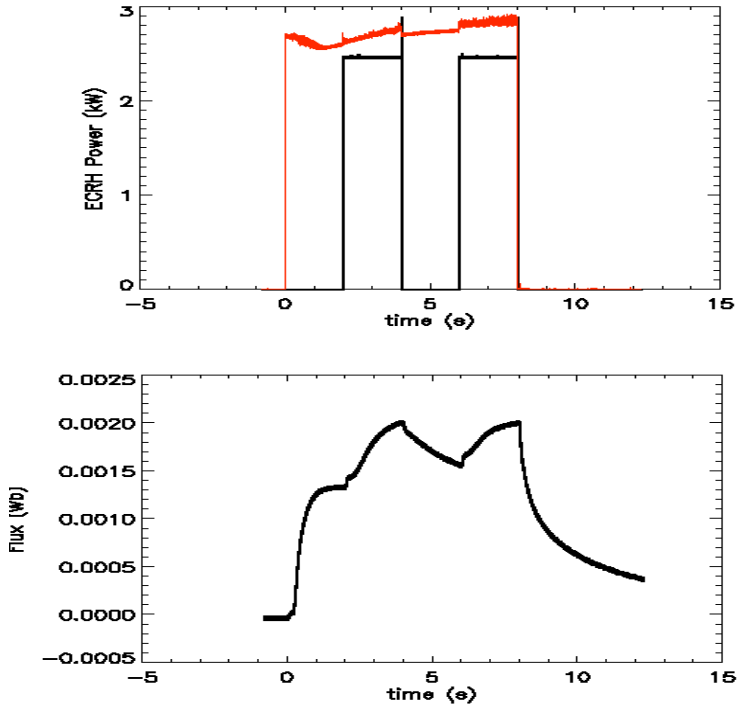

Figure 8-1: The ECRH signals (top) and the corresponding signal from a flux loop (bottom) for shot 50318009. The 2.45 GHz signal is shown in red and the 6.4 GHz signal is shown in black.

The reconstructed pressure profiles at t = 2, 8 sec are shown for both shots in Figure 8-3. Both heating sources are on at t = 8 sec for either shot. As expected, the pressure profiles are more or less similar for both shots at t = 8 sec. However, there are distinct differences between the profiles for shots 50318009 and 50318010 at t = 2 sec, when only one source is on. The profile is much more broad and much less peaked when only 2.45 GHz is present compared to when only 6.4 GHz is present. The heating may be more distributed when only 2.45 GHz is present since waves absorbed at both the fundamental and first harmonic locations can effectively heat

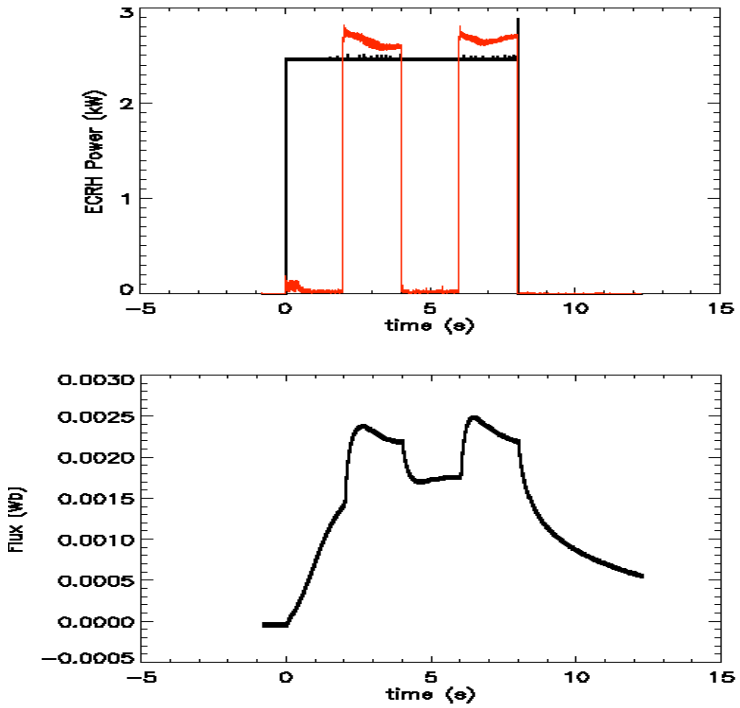

Figure 8-2: The ECRH signals (top) and the corresponding signal from a flux loop (bottom) for shot 50318010. The 2.45 GHz signal is shown in red and the 6.4 GHz signal is shown in black.

the plasma. However, there may not be enough first harmonic absorption in the 6.4 GHz only case, and the heating may be largely concentrated at the midplane of the fundamental location. Heating at a single location rather than at two locations could lead to a more peaked profile. Some equilibrium parameters for the two shots at the two times are listed in Table 8.1.

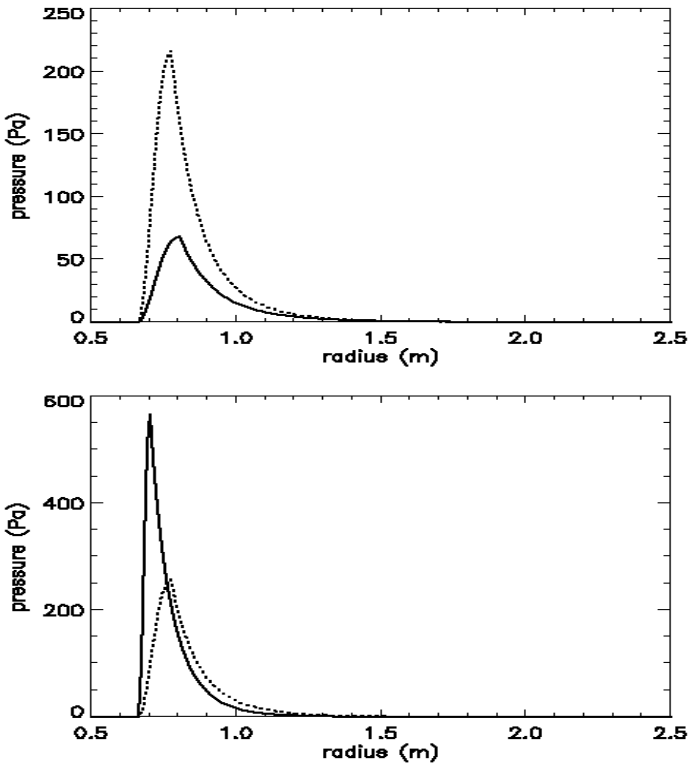

Figure 8-3: The best fit pressure profiles for shots 50318009 (top) and 50318010 (bottom) at t = 2 sec (solid) and 8 sec (dotted).

As a comparison to the current magnitudes and centroids obtained from the best fit pressure profiles, Figure 8-4 shows the corresponding parameters obtained from DFIT as a function of time. Although there may be some numerical discrepancies between the DFIT and the full reconstruction results, their trends are consistent with the magnetic sensors being sensitive to the plasma dipole moment. When DFIT

Equilibrium parameters	2.45 GHz only	6.4 GHz only	Both (50318009)	Both (50318010)
Pressure peak location (m)	0.80	0.70	0.77	0.77
Steepness parameter ($\times\frac{5}{3}$)	0.94	1.37	1.13	1.17
Peak pressure (Pa)	68	566	216	256
Peak beta (%)	3.5	12.0	9.0	10.8
Volume averaged beta (%)	1.5	0.4	1.3	1.3
Total stored energy (J)	74	115	149	170
Plasma current (kA)	1.31	2.75	2.55	2.89
Current centroid (m)	1.10	0.85	0.99	0.98
χ^2	11	11	29	29

Table 8.1: The equilibrium parameters of shots 50318009 and 50318010 at t = 2, 8 sec calculated from the best fit pressure profiles.

overestimates the current compared to the full reconstruction, it underestimates the current centroid; inversely, when DFIT underestimates the current, it overestimates the centroid. The DFIT results show that the magnetic sensors can actually decipher a bit more than the dipole moment. Even though the numerical values may be somewhat off, DFIT, which is not constrained by x-ray emissivity data, correctly predicts the direction of change of the current magnitude and centroid as the two ECRH sources are modulated.

The pressure model used in the above reconstructions is the DipoleEq profile that was discussed in Ch. 6. It is worth mentioning the chi-squared (figure of merit) values obtained for the above reconstructions for the different combinations of heating frequencies. When either 2.45 GHz or 6.4 GHz was on solo, $\chi^2 \approx 11$. In contrast, when both sources were on for either shot, $\chi^2 \approx 29$. The trend of having a lower chi-squared when only one source is on is seen for other shots and pressure models as well. Perhaps, the single-peak pressure models are not adequate to describe LDX plasmas that are heated by the two frequencies simultaneously due to the possible presence of two pressure peaks.

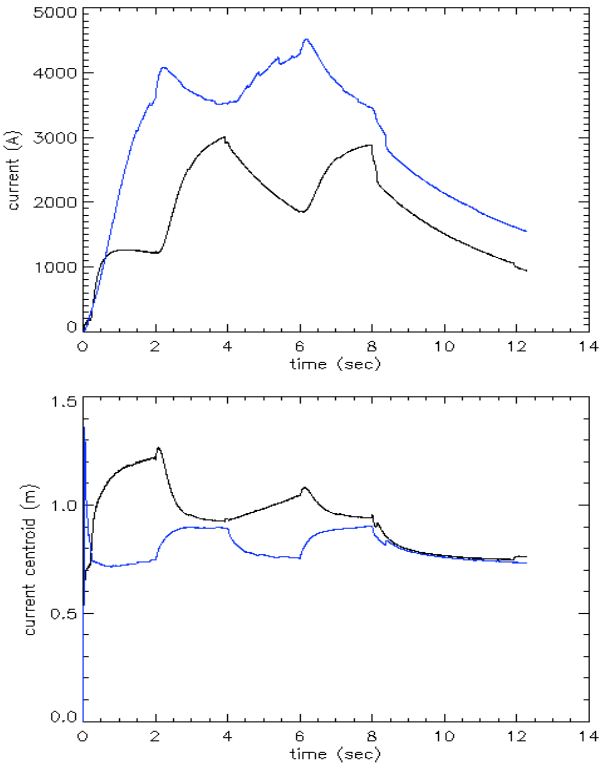

Figure 8-4: The current magnitudes (top) and centroids (bottom) from DFIT for shots 50318009 (black) and 50318010 (blue) as a function of time.

8.2 Gas Fueling Control

The control of gas fueling in LDX is an important tool to study the properties of the hot electron interchange mode. The initial amount of gas can determine the evolution of the plasma throughout a shot. Successive puffing can control the plasma in real time during the shot. The gas puffing example to be discussed in this section gives an insight into the characteristics of the HEI.

Figure 8-5 shows the signals from the ion gauge and one of the flux loops for a shot in which the gas is puffed periodically throughout the shot. The flux loop signal shows the plasma vacillating between the low density regime (HEI unstable) and the high beta regime (HEI stable). As discussed in Ch. 5, the plasma becomes susceptible to the HEI when the neutral pressure falls below a critical value. The plots show that this critical pressure is different from the critical pressure needed to go from the low density regime to the high beta regime; the critical pressure in going from the low density regime to the high beta regime is higher than that in going from the high beta regime to the low density regime. Hence, there is a clear hysteresis in the gas required to stabilize the HEI.

Although the previous example shows the need for maintaining sufficient neutral pressure to keep the plasma in the high beta regime, excessive fueling can kill the plasma. Figure 8-6 shows a shot in which the plasma is overfueled. The five large gas puffs from 2.5 to 3.5 sec almost destroys the plasma. For optimal plasma performance, the fueling must be sufficient to keep the plasma in the high beta regime but not excessive such that the amount of neutral gas overwhelms the heating power.

8.3 Vertical Field Control

LDX is equipped with a pair of Helmholtz coils that can impose a semi-uniform vertical field of up to 300 G in the plasma. This field is sufficient to substantially reduce the size of the plasma. To study the effects of the vertical field on the plasma, equilibrium reconstructions have been performed at four different Helmholtz coil currents.

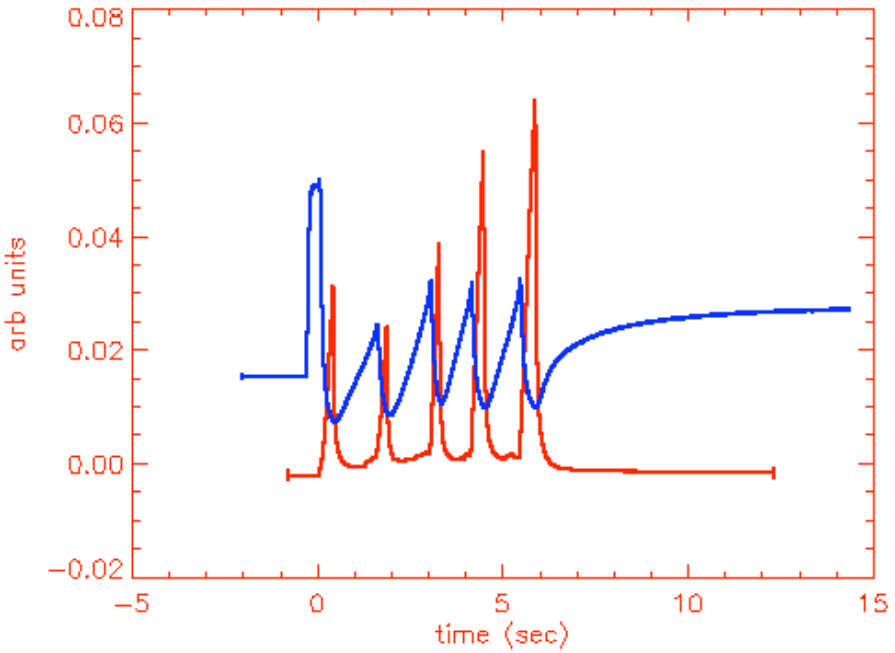

Figure 8-5: Plots of the ion gauge pressure (blue) and one of the flux loops (red). The plasma oscillates between the low density and high beta regimes.

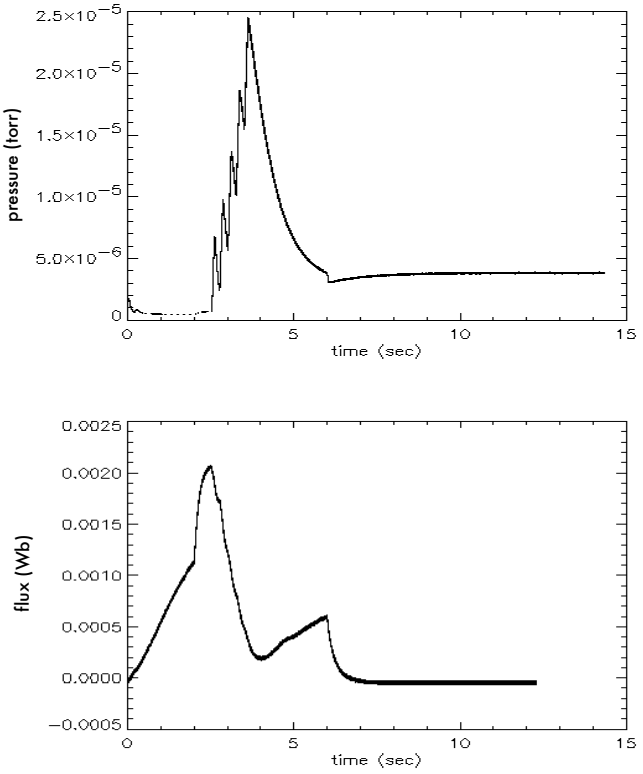

Figure 8-6: Plots of the ion gauge pressure (above) and one of the flux loops (below) for shot 50513002. Excessive fueling causes the plasma to almost disrupt.

The H-coil current was varied from 0 to 24 kA in steps of 8 kA. The plasma took on various shapes through the scan as Figure 8-7 depicts. As the H-coil current was raised from 0 to 8 kA, the plasma separated from the wall and assumed a double-null configuration. The two nulls converged into a single null at an H-coil current between 8 kA and 16 kA. As the current was further increased to 24 kA, the null moved further in towards the floating coil, substantially reducing the volume of the plasma.

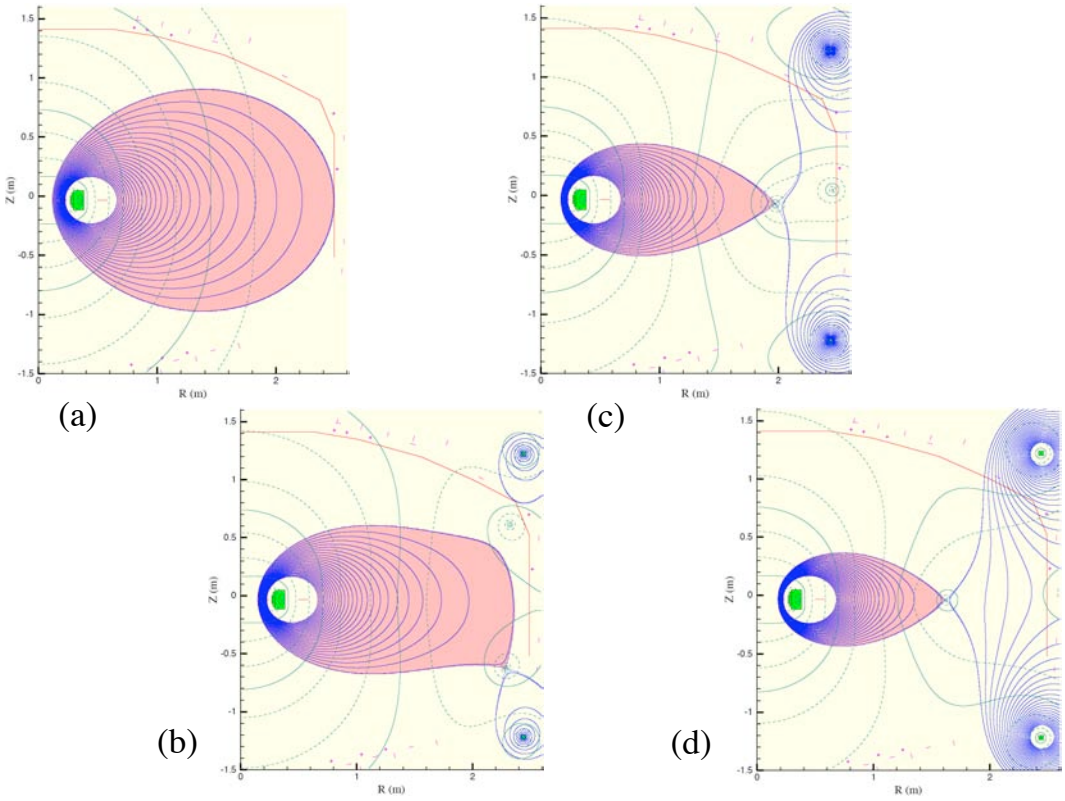

Figure 8-7: Shape of the plasma at a Helmholtz coil current of (a) 0 kA, (b) 8 kA, (c) 16 kA, and (d) 24 kA.

The pressure profile at each H-coil current was reconstructed using the DipoleEq isotropic model. Figure 8-8 shows the current and pressure profiles. Generally, the pressure and current profiles became more peaked as the vertical field increased and the plasma got smaller. This makes sense qualitatively since the profiles must become

steeper to accommodate the same amount of heating energy in a smaller plasma volume. The 8 kA and 16 kA cases had less edge pressure and steeper profiles compared to the 0 kA (no vertical field) case. At 24 kA, however, the edge pressure jumped beyond the no vertical field case while maintaining the steep profiles. It seems plausible that the plasma can sustain a high edge pressure in the presence of a separatrix.

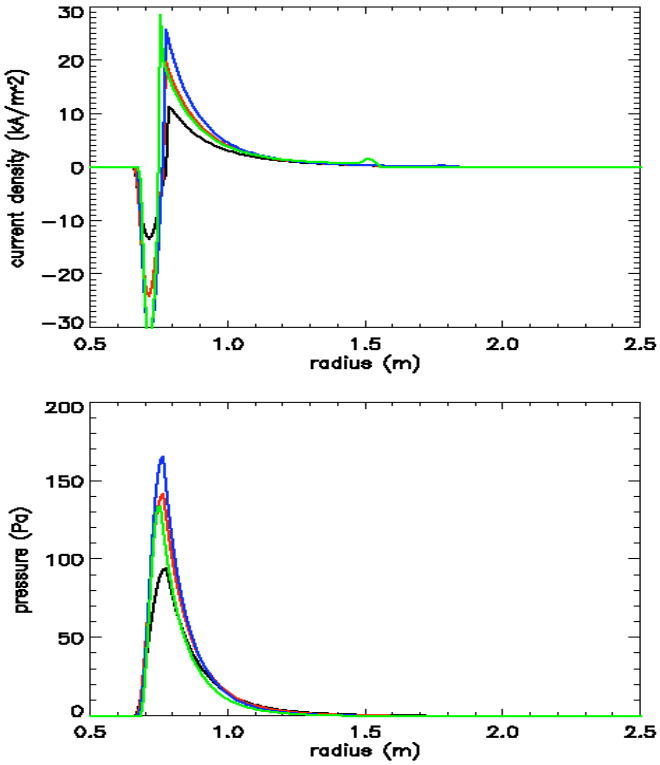

Figure 8-8: Current and pressure profiles for the four vertical field currents: 0 kA (black), 8 kA (red), 16 kA (blue), and 24 kA (green).

Table 8.2 lists the equilibrium parameters for the four vertical field cases. As seen from the pressure plots, the profiles are steeper and peak at higher values when the vertical field is present. The beta values increase as the vertical field is increased, because the separatrix moves in closer to where there is more pressure. The high peak beta values at higher Helmholtz currents are reached right around the X-point.

Equilibrium parameters	0 kA	8 kA	16 kA	24 kA
Pressure peak location (m)	0.77	0.76	0.76	0.75
Steepness parameter ($\times\frac{5}{3}$)	1.00	1.13	1.23	1.17
Peak pressure (Pa)	94	142	165	136
Peak beta (%)	4.4	6.5	37.9	83.1
Volume averaged beta (%)	1.3	1.8	4.0	4.4
Total stored energy (J)	76	81	8	50
Plasma volume (m^3)	28.4	12.0	6.0	3.8
Plasma current (kA)	1.44	1.67	1.66	1.31
Current centroid (m)	1.05	0.98	0.94	0.93
χ^2	20	40	78	117

Table 8.2: Equilibrium parameters for the four Helmholtz currents.

The total stored energy does not change too much (except for the 16 kA result, which may be spurious) regardless of the plasma size, giving credence to the necessity of the smaller plasmas to have steeper pressure profiles. The plasma current also remains fairly constant as the plasma shrinks from 28.4 m^3 to 3.8 m^3. The larger current density required to maintain a similar level of current in a smaller plasma is consistent with the smaller plasma having a steeper pressure profile. As for the current centroid, it naturally moves inward as the plasma is compressed about the floating coil.

8.4 Comprehensive Plasma Control

The previous sections demonstrate that LDX plasmas can be controlled in different ways using the three knobs. The controls can operate independently from each other or in conjunction. The RF power and frequency composition controls can be used to alter the pressure gradient and peak location while the gas control can set the edge fueling and weakly modify the density profile. The Helmholtz coils are used to control

the size and topology of the plasma. In terms of their utilities, the RF and gas controls will be instrumental in suppressing the MHD and hot electron interchange modes, respectively. For example, signals from the magnetic diagnostics and ion gauge can be fed back to control these instruments. Although the effect of the plasma topology on its stability properties is unclear at this point, we can envision a similar feedback system to control the Helmholtz coils to suppress, for example, a parasitic mode with certain spatial characteristics.

The RF, gas, and Helmholtz controls must be adjusted in unison on certain occasions. In particular, there may be an interaction between the different controls, and the effect of one must be taken into account when controlling another. For example, the neutral pressure threshold against the HEI increases as the plasma volume decreases and heating power increases. Hence if the plasma is stable against the HEI at a given gas fueling setting, it must be increased if the heating power is increased or the plasma volume is decreased or both. It is important to always be aware of the global effects of a control knob and its interactions with the other controls.

Chapter 9

Analysis

The goal of this chapter is to present what we have learned about dipole plasmas from magnetic measurements. These findings help us understand the most basic properties of dipole confinement and will shape the direction of future experiments. Given that the current set of magnetic diagnostics is the first generation, there undoubtedly are some shortcomings. Some of the shortcomings are inherent to magnetic diagnostics in general while others are attributed to the particular system on LDX. Some of the shortcomings particular to LDX and their possible remedies will also be discussed.

9.1 High beta measurement

One of the advantageous features and selling points of LDX is its ability to confine high beta plasmas. The theoretical possibility of attaining high beta must be corroborated through experimental measurements. The highest beta shot on LDX to date is shot 50513029. This shot has been reconstructed using both the isotropic and anisotropic models. The DipoleEq isotropic model is used in the full reconstruction, and the "smooth adiabatic" isotropic and anisotropic models are used in the vacuum reconstruction. The anisotropic result is important not only as a comparison to the isotropic result, but because LDX plasmas seem to be anisotropic from x-ray pictures and the anisotropic model ascribes a higher pressure and beta for a given current distribution.

Equilibrium parameters	DipoleEq	Smooth adiabatic (isotropic)	Smooth adiabatic (anisotropic)
Pressure peak location (m)	0.77	0.77	0.77
Steepness parameter ($\times\frac{5}{3}$)	1.09	1.44	2.11
$\frac{P_\perp}{P_\parallel}$	1	1	5
Peak pressure (Pa)	332	131	601
Peak beta (%)	14.4	12.1	26.5
Volume averaged beta (%)	2.4	3.6	2.0
Total stored energy (J)	238	320	309
Plasma current (kA)	4.13	4.15	3.48
Current centroid (m)	1.01	1.11	1.19
χ^2	32	24	23

Table 9.1: Equilibrium parameters obtained from the two isotropic and the anisotropic pressure models.

Table 9.1 summarizes the reconstruction results. The pressure peak location has been fixed accordingly to the x-ray emissivity data for each model. There are significant profile differences between the two isotropic models, but the beta values come out to be relatively similar. Despite the isotropic smooth adiabatic model having a much lower peak pressure compared to the DipoleEq model, its peak beta value comes out only slightly less than what the DipoleEq model gives. This is because the smooth adiabatic model gives a broad pressure peak, and the magnetic field drops off more quickly than the pressure until well after the peak. Consequently, its beta peaks far from the pressure peak where the field is low enough to give a comparable $\frac{P}{B^2}$ ratio to that of the DipoleEq model at its beta peak. On the other hand, the beta peaks at the pressure peak for the DipoleEq model because the pressure falls off much faster than the field (R^{-4g} vs. R^{-3}) from the peak on outwards. The broad profile of the smooth adiabatic model also accounts for its larger stored energy compared to the DipoleEq model. Figure 9-1 shows the reconstructed pressure and beta profiles

of the three models.

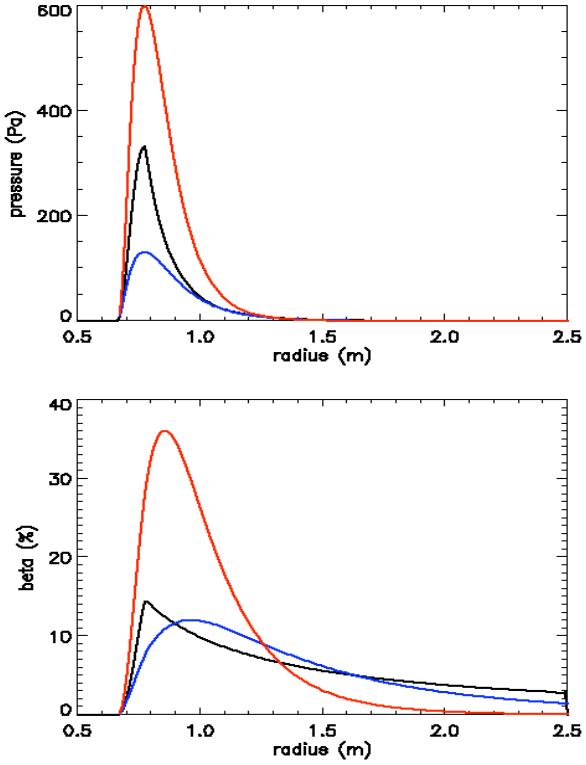

Figure 9-1: The reconstructed pressure and beta profiles of the DipoleEq model (black), isotropic smooth adiabatic model (blue), and anisotropic smooth adiabatic model with $\frac{P_\perp}{P_\parallel} = 5$ (red). The beta for the anisotropic case is the perpendicular beta.

The degree of anisotropy of the anisotropic model has been chosen to roughly agree with the x-ray pictures of typical ldx plasmas. As the plasma becomes more anisotropic, it becomes more confined to the midplane. X-ray pictures like Figure 6-5 help us estimate the anisotropy, and $\frac{P_\perp}{P_\parallel} = 5$ seems to be a plausible value. In light of the discussion in Ch. 6, it is not surprising that the anisotropic model gives a very steep pressure profile, leading to remarkably high peak pressure and beta values. A peak beta of 26.5 % (perpendicular beta of 36.2 %) is the highest seen to date. Because the energy of the anisotropic plasma is localized in a small volume around the

inner midplane, its volume averaged beta and total stored energy are comparable to (if not lower than) the isotropic plasma despite the very high peaks the pressure and beta attain. The contour plots of the pressure and current in Figure 9-2 demonstrate how they become more localized as the plasma goes from isotropic to anisotropic with $p \equiv \frac{P_\perp - P_\parallel}{2P_\parallel} = 2$. Notice that the pressure contours no longer coincide with the flux contours in the anisotropic case.

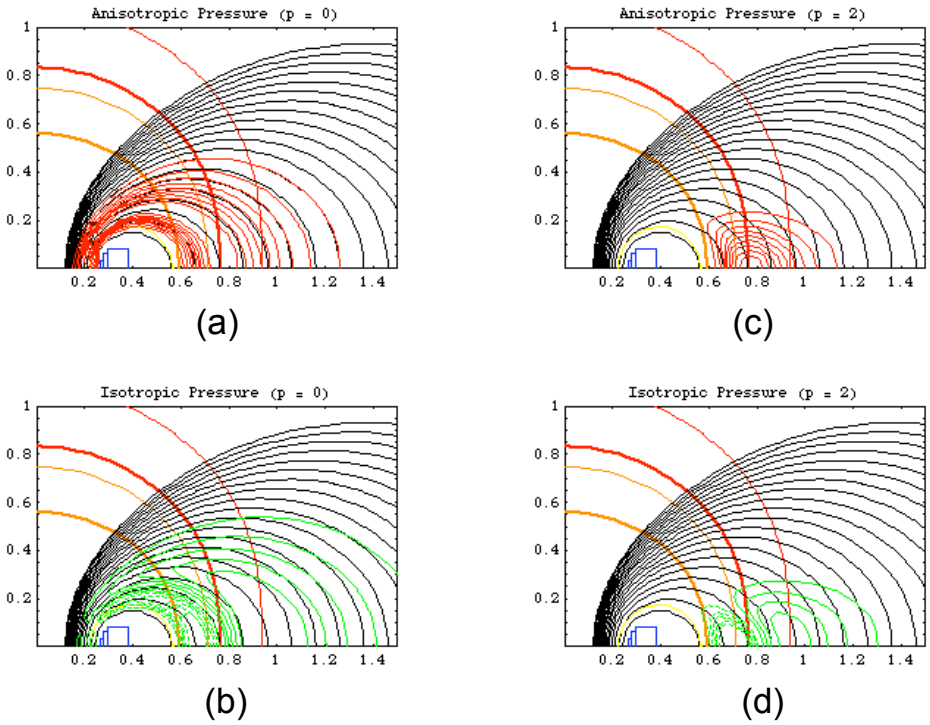

Figure 9-2: The reconstructed (a) pressure and (b) current contours using the isotropic smooth adiabatic model and (c) pressure and (d) current contours using the anisotropic model with $p = 2$.

The condition under which the high beta plasma was produced is worth noting. Prior to shot 50513029, many long-pulse conditioning shots had been performed to thoroughly clean the vessel and reach good vacuum status. Hence, shot 50513029

and its surrounding shots, which attained similar beta values, most likely produced plasmas that were cleaner than average. Besides that, the shot was no different from ordinary with both sources on at full power and sufficient fueling to avert HEI events during the high beta phase.

Finally, the reconstruction results show that the magnetic diagnostics alone are incapable of measuring the anisotropy of the plasma. The χ^2 values for the isotropic and anisotropic cases were virtually indistinguishable. But because the reconstructed current distributions were sufficiently different between the isotropic and anisotropic cases, there may be hope that additional well-placed sensors can acquire some information about pressure anisotropy. For now, we must depend on x-ray camera data to estimate the anisotropy of ldx plasmas.

9.2 Measurement of Supercritical Profiles

One of the key results of reconstructing LDX plasmas is the measurement of supercritical pressure gradients. It has been alluded in Ch. 2 that because hot electrons are subject to the HEI rather than the MHD criterion, they can exceed the MHD pressure gradient limit, $P \sim V^{-\gamma}$. One of the main importance of the magnetic diagnostics on LDX is their ability to verify whether hot electrons do indeed exceed the MHD limit. Figure 9-3 gives a plot of ten shots that have been discussed thus far in the R-g space, where R is the pressure peak location and g is the steepness parameter. All these shots have been reconstructed using the DipoleEq model, and the pressure peak has been constrained using x-ray emissivity data. The steepness parameter and edge pressure are unambiguously constrained by magnetic data. The plot shows that all but two of the ten shots give a best fit g that exceeds $\frac{5}{3}$. It is therefore fair to say that LDX plasmas routinely have pressure profiles that are steeper than what MHD allows.

To really verify that the supercritical steepness parameters are the best fit to the magnetics, plots of χ^2 vs. g for the highest beta shot are shown in Figure 9-4. It is clear that χ^2 does indeed reach a minimum at a supercritical $\frac{g}{\gamma}$ value of about 1.09

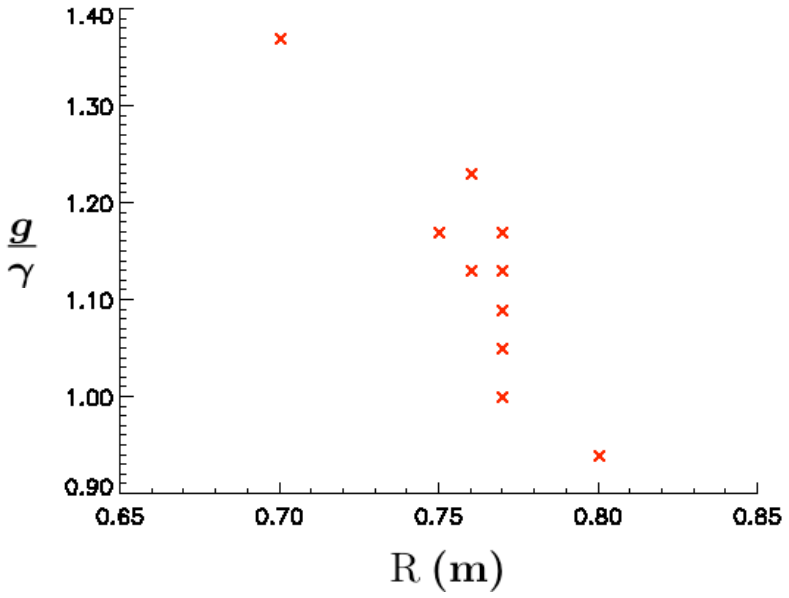

Figure 9-3: A plot of ten shots that have been reconstructed using the DipoleEq model. Most shots have pressure profiles steeper than $V^{-\frac{5}{3}}$

.

for the DipoleEq pressure model. The smooth adiabatic models give even higher g values, with the best fit g increasing as anisotropy increases, but this result is less relevant since the smooth adiabatic models do not exactly have the form of the MHD stability criterion.

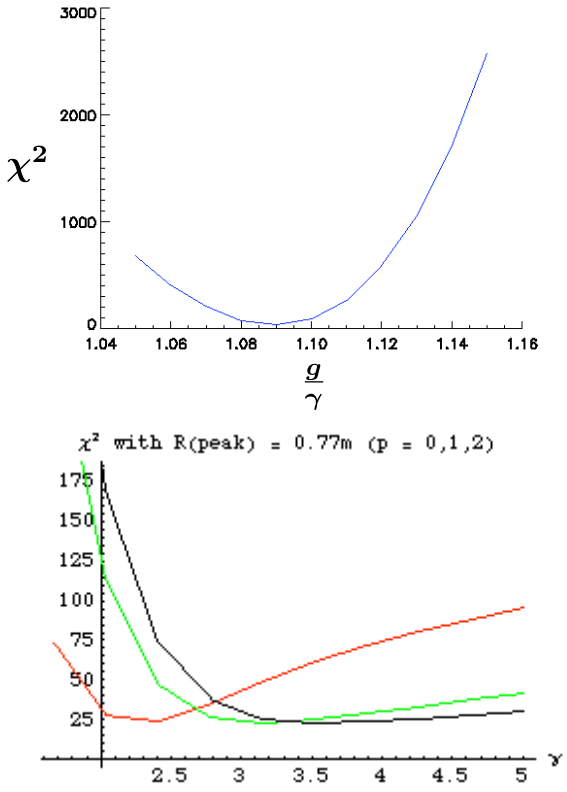

Figure 9-4: A plot of χ^2 vs. $\frac{g}{\gamma}$ for the highest beta shot using the DipoleEq model (top) and plots of χ^2 vs. g for the same shot using both the isotropic and anisotropic smooth adiabatic models (bottom). The red curve is the isotropic case, green is the anisotropic case with $p = 1$, and black curve is the anisotropic case with $p = 2$.

The LDX magnetic diagnostics have answered a key question concerning the stability of hot electrons. They have verified that hot electrons can indeed exceed the MHD gradient limit and are indeed not adequately described by MHD stability theory. We currently do not have enough interferometer chords to measure the density

profile, but it would be interesting to study how hot electrons are limited by their density gradient and whether the limit, if any, is consistent with the theory of the HEI.

9.3 Magnetic detection of the HEI

HEI events are most prominently detected by floating langmuir probes, but they also possess magnetic signatures as well. Depending on the severity of the event, a rapid fall of varying magnitudes in the diamagnetism can be seen on the B_p coil and flux loop signals. Some events are severe enough to destroy the plasma, and those are manifested as sharp spikes in Mirnov signals accompanied by a total loss of diamagnetism. These spikes in the Mirnov signals have been correlated to spikes in probe signals that have been extensively studied and characterized as HEI events [39]. Some examples of near-catastrophic HEI events are shown in Figures 9-5 - 9-8.

Shot 50513024 shown in Figure 9-5 displays a situation in which the HEI occurs seconds after all the RF is turned off. The after-glow regime is often susceptible to an HEI because the bulk electrons are quickly lost, and the right hand side of Eq. 5.15 can become very small. As this particular shot shows, an HEI event during an after-glow almost always leads to a quick and complete demise of what is left of the decaying plasma.

Figures 9-6 - 9-8 each show two shots that are completely identical in terms of the fueling, heating power, and heating frequencies. However, one sustains more HEI events than the other. In Figure 9-6, both shots 50513027 and 50513028 suffer an HEI event at the RF turnoff, but shot 50513028 has an extra HEI event during the high beta regime. Shot 50513040 in Figure 9-8 does not have an HEI event, but shot 50513041 does during the high beta regime. In these shots, the neutral pressure is near a critical level, and one shot happens to be on the "right" side of the stability boundary while the other shot happens to be on the "wrong" side. Shots 50513033 and 50513032 in Figure 9-7 are in a similar situation; shot 50513032 has an HEI event

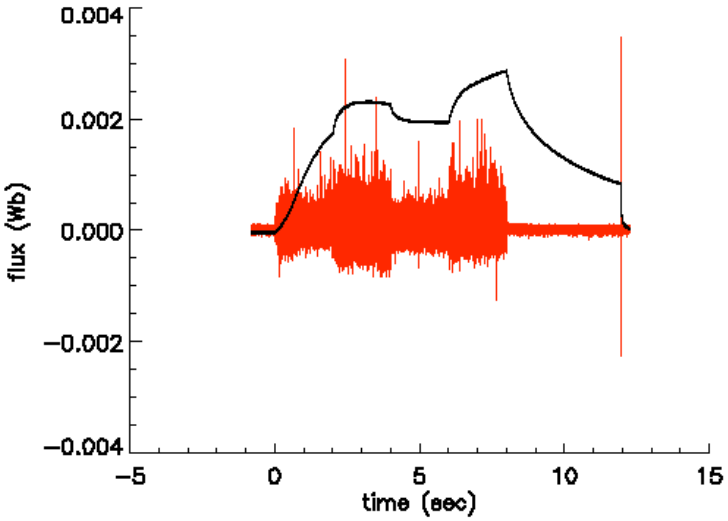

Figure 9-5: A Mirnov signal overlaid on a flux loop signal for shot 50513024. An HEI event occurs during the after-glow.

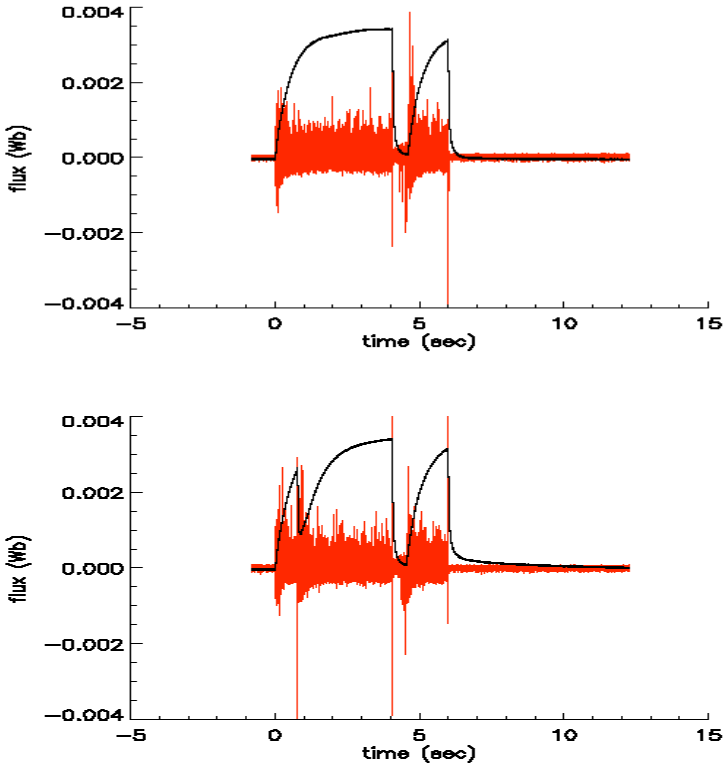

Figure 9-6: A Mirnov signal overlaid on a flux loop signal for shots 50513027 (top) and 50513028 (bottom). The two shots are identical except that shot 50513028 has an extra HEI event right before 1 sec. Both shots suffer an HEI event around 4 and 6 seconds.

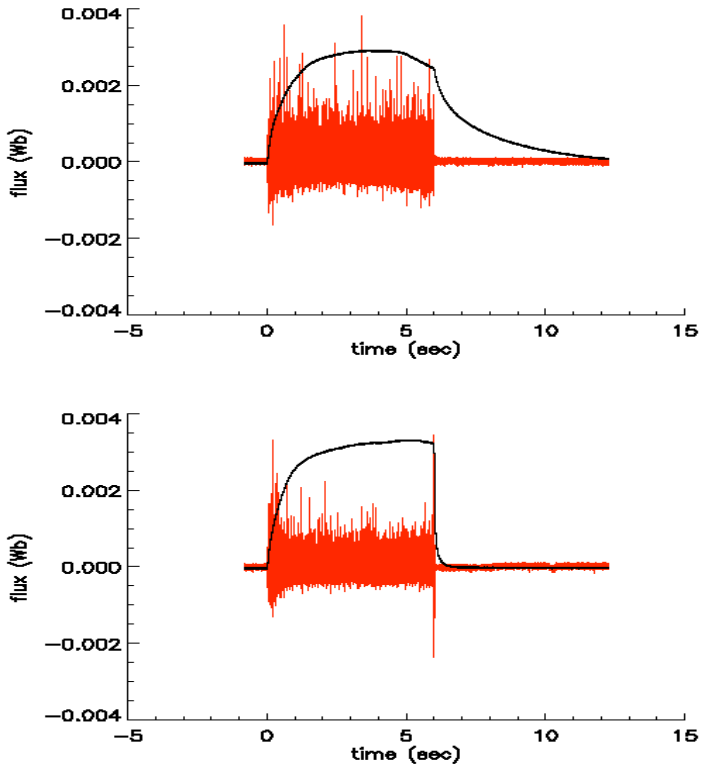

Figure 9-7: A Mirnov signal overlaid on a flux loop signal for shots 50513033 (top) and 50513032 (bottom). Shot 50513032 endures an HEI event the moment the RF's turn off. Otherwise, the two shots are identical.

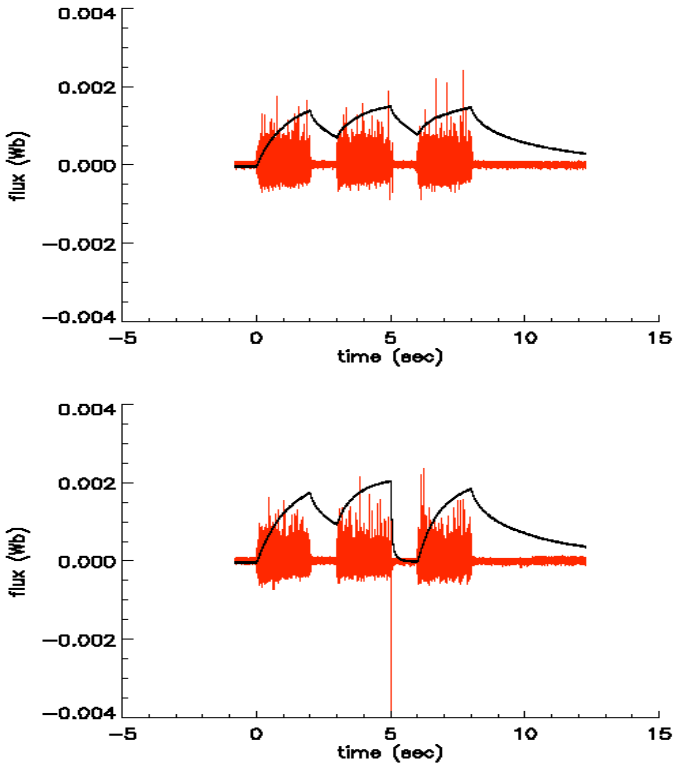

Figure 9-8: A Mirnov signal overlaid on a flux loop signal for shots 50513040 (top) and 50513041 (bottom). Again, the two shots are identical except for an HEI event that occurs around 5 sec for shot 50513041.

at the RF turnoff while shot 50513033 is HEI free. As during the afterglow regime, the plasma loses its bulk electrons at the RF turnoff and becomes extra vulnerable to an HEI event. The difference in the decay time is remarkably evident between a plasma that is terminated by an HEI event and a plasma that decays naturally from these shots.

Some HEI's that occur during the high beta regime are relatively benign and manifest themselves as periodic relaxations in the flux. When the density gradient or the $\frac{n_{eh}}{n_{eb}}$ ratio does not rise precipitously, the plasma can relax its profiles before the instability drive becomes too large. Since the plasma is at marginal stability when this happens, the relaxation process periodically repeats itself as the plasma vacillates between stable and unstable states. Figure 9-9 shows two identical shots with one enduring multiple relaxation events during the high beta regime. The relaxations lead to flux drops of only a few percent, and there are no significant accompanying Mirnov signatures.

9.4 Plasma current vs. Stored energy Relation

The dipole magnetic geometry allows us to establish an equilibrium integral relationship between the plasma current and the kinetic stored energy [37]. This problem was originally studied by geophysicists who wanted to examine the relationship between the magnetic field disturbance and the energy of the trapped particles during a geomagnetic storm. Dessler, Parker, and Sckopke eventually derived what is known as the D-P-S relation to directly tie these two quantities together [6, 44]. Here we derive an equivalent relationship but cast in a slightly different form. We start with the definitions of plasma current and stored energy,

$$I_p = \int_{\psi_1}^{\psi_2} d\psi \int \frac{d\chi}{B^2} \boldsymbol{\nabla}\phi \cdot \boldsymbol{J} \tag{9.1}$$

$$W = \frac{3}{2} \int_{\psi_1}^{\psi_2} d\psi \int \frac{d\chi}{B^2} P \ , \tag{9.2}$$

where (ψ, χ, ϕ) is the standard magnetic coordinate system. The ψ integral goes from the first closed flux surface to the last closed flux surface. The total plasma

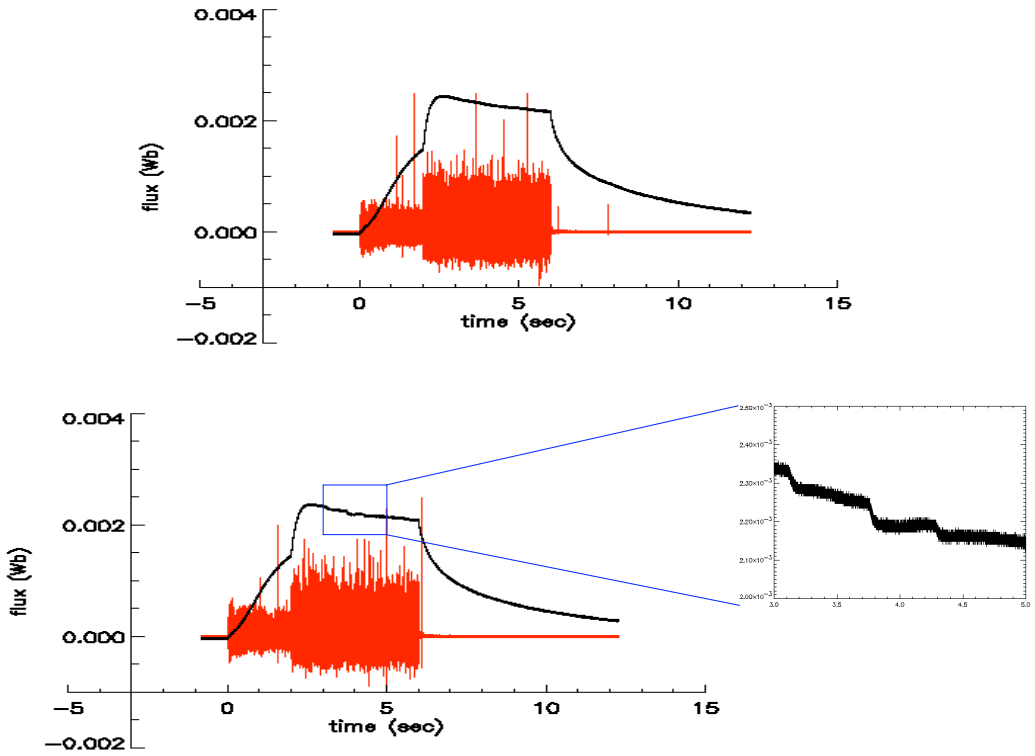

Figure 9-9: Shots 50318015 (top) and 50318016 (bottom) are identical, but shot 50318016 endures multiple relaxation events during the high beta regime. A blowup of the relaxation events is shown to the right.

volume is $\int d\psi \int \frac{d\chi}{B^2}$, and the differential flux tube volume per differential flux, V, is $\int \frac{d\chi}{B^2}$.

The MHD momentum equation, $\boldsymbol{\nabla} P = \boldsymbol{J} \times \boldsymbol{B}$, can be used to eliminate $\boldsymbol{J}$ from Eq. 9.2. After some simplification, the ratio of stored energy to plasma current can be written as,

$$\frac{W}{I_p} = \frac{3}{2} \frac{\int d\psi PV}{\int d\psi P \partial V/\partial \psi} \ . \tag{9.3}$$

For a low beta plasma, the equilibrium flux is not much different from the vacuum flux, in which $V \sim \psi^{-4}$, and Eq. 9.3 can be rewritten as,

$$\frac{W}{I_p} = \frac{3}{8} \frac{\int d\psi PV}{\int d\psi PV/\psi} \ . \tag{9.4}$$

Hence, the stored energy to plasma current ratio can be calculated once $P(\psi)$ is specified.

We can specify the pressure function to be the marginally stable profile, which is $PV^\gamma = $ const. and equivalent to the DipoleEq model profile. The energy to current ratio then becomes,

$$\frac{W}{I_p} = \frac{3}{8} \frac{\int d\psi V^{-\gamma+1}}{\int d\psi V^{-\gamma+1}/\psi} \ , \tag{9.5}$$

and again by letting $V \sim \psi^{-4}$, it becomes,

$$\frac{W}{I_p} = \frac{3}{8} \frac{\int d\psi \psi^{4\gamma-4}}{\int d\psi \psi^{4\gamma-5}} \ . \tag{9.6}$$

The above integrals can now be evaluated, and the result is the following:

$$\frac{W}{I_p} = \frac{3}{8} \left(\frac{4\gamma - 4}{4\gamma - 3} \right) \left(\frac{\psi_2^{4\gamma-3} - \psi_1^{4\gamma-3}}{\psi_2^{4\gamma-4} - \psi_1^{4\gamma-4}} \right) \ . \tag{9.7}$$

Now let us focus on the expression for the current centroid. We write the current centroid as follows:

$$\frac{R_c I_p}{I_p} = \frac{\int d\psi \partial P/\partial \psi \int (d\chi/B^2) r \sin\theta}{\int d\psi \partial P/\partial \psi \int (d\chi/B^2)} \ , \tag{9.8}$$

where r and θ are the radial and polar angle coordinates in the standard spherical coordinates. Upon computing $r \sin\theta$ along the field lines by transforming the χ integral into a ξ integral [31], with $\xi \equiv \sin^2\theta$, we get,

$$\frac{R_c I_p}{I_p} \approx \frac{\mu_0 M}{2} \frac{\int d\psi PV/\psi^2}{\int d\psi PV/\psi} \ , \tag{9.9}$$

where M is the magnetic moment of the floating coil. The above integrals can be evaluated as before using the marginally stable profile and by letting $V \sim \psi^{-4}$,

$$R_c \approx \frac{\mu_0 M}{2} \left(\frac{4\gamma - 4}{4\gamma - 5} \right) \left(\frac{\psi_2^{4\gamma-5} - \psi_1^{4\gamma-5}}{\psi_2^{4\gamma-4} - \psi_1^{4\gamma-4}} \right) \ . \tag{9.10}$$

The quantity of interest in the dipole equilibrium is $\frac{WR_c}{I_p}$, because it is nearly a constant as will be shown shortly. Multiplying the expressions for $\frac{W}{I_p}$ and R_c, we get,

$$\frac{WR_c}{I_p} \approx \frac{3}{16} \mu_0 M \frac{(4\gamma - 4)^2}{(4\gamma - 3)(4\gamma - 5)} \frac{(\psi_2^{4\gamma-3} - \psi_1^{4\gamma-3})(\psi_2^{4\gamma-5} - \psi_1^{4\gamma-5})}{(\psi_2^{4\gamma-4} - \psi_1^{4\gamma-4})^2} \ . \tag{9.11}$$

The expression on the right of M in the above equation is nearly unity in the range of γ we are interested in (Figure 9-10). For a floating coil charge of about 900 kA, its magnetic moment is equal to about 300 kA·m^2. Hence,

$$\frac{WR_c}{I_p} \approx \frac{3}{16} \mu_0 M \approx 70 \text{ J·m·kA}^{-1} \ . \tag{9.12}$$

The stored energy-current relationship is important, because it allows us to estimate the plasma stored energy without fully reconstructing the equilibrium; we can instead find the plasma current and its centroid using a current filament code like DFIT and use the above relationship.

Plots of W vs. $\frac{I_p}{R_c}$ is shown for all the 900 kA charge shots described in this thesis in Figure 9-11. The best fit line through the nine data points has a slope of about 60 J·m·kA^{-1}, which is about 14 % lower than the theoretical value. In the theoretical derivation, we assumed the pressure to have the marginally stable profile from the first closed flux surface to the last closed flux surface. In reality, the marginally stable profile is valid from the pressure peak to the last closed flux surface, and the profile should smoothly increase from the first closed flux surface to the peak. Hence, we may have overestimated the integrals involved in the calculations, leading to an overestimation of $\frac{WR_c}{I_p}$.

9.5 Energy confinement time

The ECRH modulation shots discussed in the previous chapter are helpful to learn about the effect of the heating frequency on the energy confinement time of the

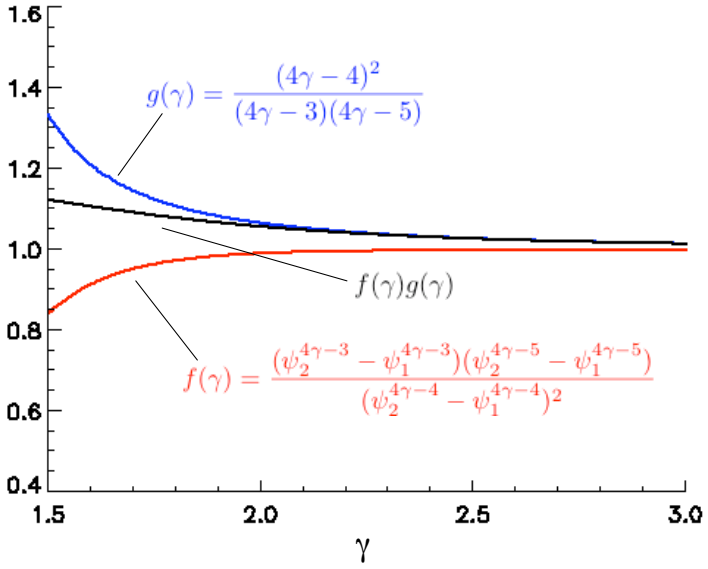

Figure 9-10: Plots of the two functions of γ and their product that appear in the expression for $\frac{WR_c}{I_p}$. The ψ values have been chosen for a floating coil charge of 900 kA.

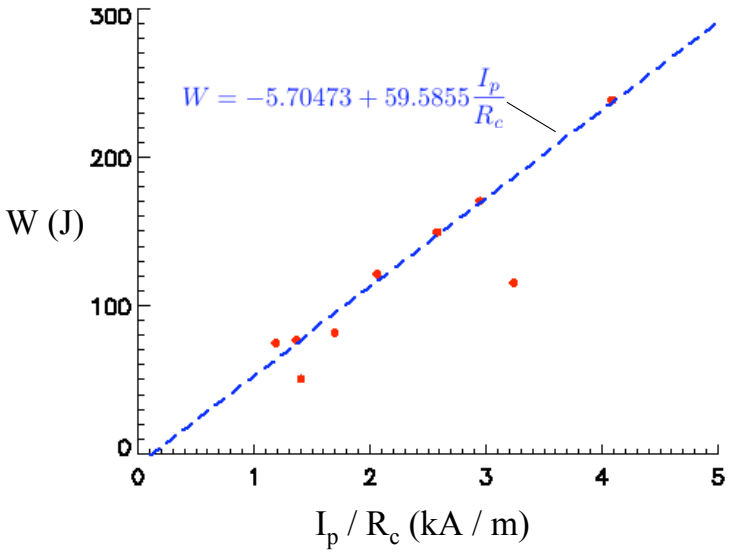

Figure 9-11: Plots of W vs. $\frac{I_p}{R_c}$ for nine 900 kA charge shots. The best fit line predicts a $\frac{WR_c}{I_p}$ value of about 60 J·m·kA^{-1}. Error bars have been suppressed since they are smaller than the dots in the y direction and on the order of their size in the x direction.

plasma. Simplistically, the energy confinement time can be found by dividing the plasma stored energy by the total heating power. Doing so for shots 50318009 and 50318010, we find the energy confinement time for the 2.45 GHz only heating case to be about 25 ms and that for the 6.4 GHz only heating case to be about 40 ms. When both sources are on, the energy confinement time is about 30 ms. It seems like 6.4 GHz heating results in a higher energy confinement time than 2.45 GHz heating. This trend is seen in a study of a larger number of shots with different heating powers of the two frequencies (Figure 9-12). There is a general trend that shows the greater the heating power fraction of 2.45 GHz, the worse the confinement time. Physically, the 2.45 GHz microwave heats a larger plasma volume, thereby creating more bulk species that are susceptible to parallel losses to the floating coil supports. It will be interesting to see how the confinement times change when the floating coil is levitated.

9.6 Analysis Summary

This chapter discussed some of the most important results of the experiment to date. By using the anisotropic pressure model, a peak beta of more than 26 % has been measured. It should be reiterated that the use of an anisotropic model is not only justified but absolutely required to obtain the correct beta values. For a given set of magnetic measurements, the reconstructed beta increases as the anisotropy increases. An anisotropy parameter value of 2 ($\frac{P_\perp}{P_\parallel} = 5$) is obtained for this reconstruction by comparing the model pressure contours to the x-ray emissivity contours.

Figure 9-3 displays the reconstruction results of 10 LDX shots and convincingly shows that supercritical pressure profiles are routinely obtained. As mentioned repeatedly before, the result is not surprising given that the hot electrons carry most of the pressure, but the affirmation of the expected result unequivocally proves the case that the MHD limit is irrelevant for the hot electrons. The next step is to test the applicability of the HEI limit by measuring the density profile of the hot electrons using a multi-chord interferometer. Also, it would be interesting to see if the MHD

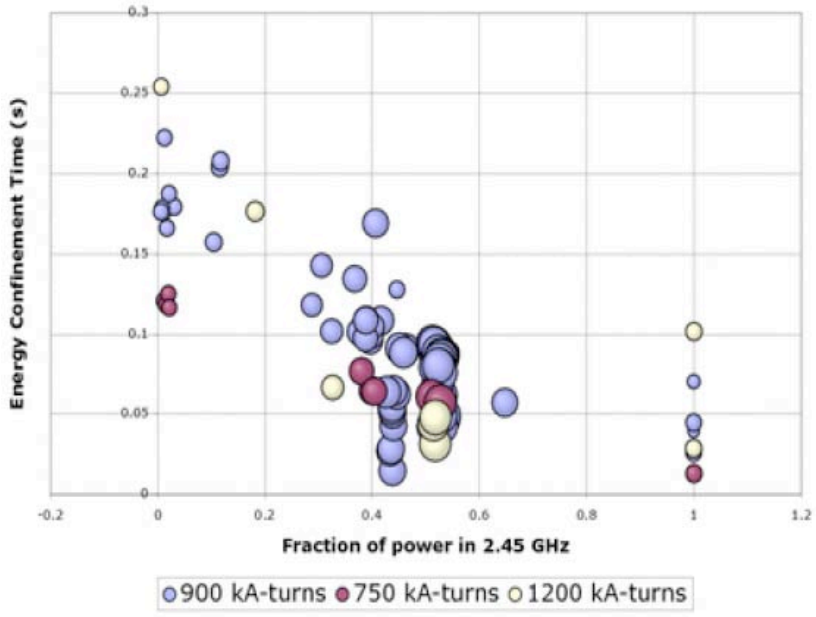

Figure 9-12: Plots of energy confinement time vs. 2.45 GHz heating fraction. The different colors represent the different floating coil currents, and the spot sizes represent the total heating power. The stored energies have been estimated using the current-energy relation of the previous section.

limit becomes relevant when the electrons are thermalized during the third phase of the experiment.

Although the Mirnov coils were never designed to measure the HEI's, their signatures are clearly visible in the data. The details of their mode properties cannot be extracted from the Mirnov signals, but their occurrences can be clearly correlated temporally to drops in the flux signals. This observation is sufficient to surmise that HEI events cause a global reorganization of the plasma current, possibly allowing for the density profile to relax.

Finally, a theoretical relationship between the plasma current and stored energy, much like the D-P-S relation, is derived and compared to empirical data. Perhaps due to an inaccurate approximation in the derivation, the empirical data slightly disagrees with the theoretical relation. Nevertheless, it is an important finding that the empirical data is consistent with a linear relationship between the current and stored energy. This relationship is very convenient since the plasma stored energy can be estimated by merely knowing its current. The relationship has been used to quickly estimate the energy confinement time of various LDX shots with different heating frequency compositions. Although the reasons are yet unclear, 2.45 GHz heating seems to be less efficient than 6.4 GHz heating.

Chapter 10

Conclusion

10.1 Main Results

The main results of the thesis clearly are the measurement of high beta and the measurement of supercritical pressure profiles. These two measurements answer some of the most basic questions regarding LDX physics. We have verified that LDX is capable of sustaining stable, high beta plasmas for a prolonged period if there is sufficient neutral fueling to suppress the hot electron interchange mode. Also, the relative importance of the MHD interchange mode and the HEI is now understood, at least as far as the hot electrons are concerned. In LDX the pressure is carried by the hot electron species, and we have seen that the pressure profile can be measured by the magnetics. Ideal MHD is not seen to play a role in determining the beta limit for this hot electron plasma. MHD may still provide a limit to the pressure gradient of the low beta background plasma, but the effect is difficult to measure since the background plasma contributes negligibly to the total pressure. This will inevitably change as we progress through the experimental phases and the electrons are made to thermalize.

10.2 Summary

This thesis has described the basic properties of the Levitated Dipole Experiment from a magnetic diagnostics standpoint. The work illuminates the basic physics of dipole MHD equilibrium and stability. Because the current phase of operation involves plasmas with a significant population of hot electrons, the basic properties of the hot electron interchange mode have been touched as well. All the hardware that makes this experiment possible, and the technological feat that had to be overcome is described in the very first chapter.

The main players of this work have been the magnetic diagnostics. The description and design of the different types of magnetic sensors are presented in Ch. 2, while Ch. 3 tackles the mathematical problem of positioning the sensors where they are most sensitive to changing plasma parameters. A comprehensive error analysis is performed in Ch. 4 to relate the measured field errors to errors in the reconstructed equilibrium parameters.

One of the main points of the thesis deals with the details of the reconstruction process as applied to LDX plasmas in particular. The unique experimental configuration of LDX brings about some difficulties in the reconstruction process. One such difficulty is the requirement to keep the flux linked by the superconducting floating coil constant while the plasma current ramps up. In theory, this requires an iterative solution to get the right plasma current and floating coil current. In practice, the current filament code, DFIT, helps estimate the change in the floating coil current, thereby eliminating the need to iterate for a solution. Another more serious difficulty is the inability of the magnetic sensors to decipher between different pressure profiles with the same dipole moment. The reason for this shortcoming is the large distance between the plasma and the magnetic sensors, hence making it difficult for them to measure higher order moments. Simulations show that this problem could be overcome by installing sensors closer to the plasma, but x-ray emissivity data is used for now to constrain the radial location of the pressure profile peak and permit the reconstruction of the constrained pressure profile.

The LDX configuration has its advantages as well. Unlike the tokamak, the LDX vacuum field closely resembles the plasma field, and the vacuum field can consequently be used to relate plasma pressure to plasma current without having to solve the Grad-Shafranov equation. This approximation works well for our plasmas with relatively low currents. The vacuum reconstruction technique gives us the potential to quickly reconstruct the equilibrium in real time and may be used in the future to provide input equilibrium parameters for feedback control of the plasma. The most notable advantage of the dipole magnetic configuration comes from its simplicity. From a reconstruction perspective, the lack of toroidal field in its equilibrium greatly simplifies the fitting process since $F \equiv RB_\phi$ need not be parameterized. This also gives a direct relationship between the plasma current and $\frac{dP}{d\psi}$, making the vacuum reconstruction possible.

A fair number of shots has been reconstructed to find the plasma equilibrium under various conditions. The plasma condition is varied using one of the three experimental knobs, including ECRH control, fueling control, and application of different magnitudes of vertical field. The reconstructed pressure profiles (with the help of x-ray data) clearly show that applying different heating frequencies can alter the peak position and steepness of the profile. DFIT results show an appropriate change in the current profile as the heating frequency is modulated. It is shown that sufficient fueling is necessary to avert HEI events, which are prevented by maintaining an adequate level of background plasma density, while too much fueling leads to a beta collapse. Different strengths of vertical field have been applied to the plasma to change its shape and size to different degrees. It is found that compressing the plasma does not significantly change the amount of current it carries, and the pressure profile is steepened accordingly to accommodate the current in a smaller volume.

The most important result in the thesis is the measurement of the high beta. The highest beta shot to date, shot 50513029, has been reconstructed using both an isotropic and anisotropic models. Although magnetic diagnostics cannot distinguish between an isotropic and anisotropic plasma, the physics of ECRH heating, corroborated by x-ray pictures, serves as an evidence that our plasmas are highly

anisotropic with $\frac{P_\perp}{P_\parallel} \sim 5$. As far as beta measurements go, using an anisotropic model is imperative since, as discussed in Ch. 6, it gives a larger pressure gradient for a given current density. The anisotropic reconstruction of shot 50513029 gives a peak perpendicular beta of a whopping 36 %. The average beta and total stored energy are not, however, significantly altered by the anisotropic model. It is important to keep in mind that the excellent vacuum condition achieved prior to and during shot 50513029 undoubtedly helped achieve the high beta.

Another significant result is the measurement of supercritical pressure profiles of hot electrons. The plots in Ch. 9 convincingly show that LDX plasmas routinely exceed the MHD gradient limit and have a typical steepness parameter between $\frac{5}{3}$ and $1.4 \times \frac{5}{3}$. This is evidence that hot electrons are not subject to the MHD criterion and the MHD stability analysis is not adequate to describe them. The next step would be to use density profile measurements to check the validity of the hot electron interchange limit.

Other important results of the thesis include correlating HEI events to beta drops and establishing a relationship between plasma current and stored energy. Chapter 9 shows a number of HEI events that cause substantial beta drops in the high-beta and afterglow regimes. The beta drops are always coincident with sharp spikes in the Mirnov data. Some HEI events that occur in the high-beta regime are more benign with only a few percent drop in the flux. These events often occur periodically throughout the high-beta regime and do not manifest themselves in the Mirnov signals. The relationship between plasma current and stored energy is derived assuming a marginally stable pressure profile, $PV^\gamma = \text{const.}$, and predicts stored energy is related to plasma current through the relation, $\frac{WR_c}{I_p} \approx 70$ J·m·kA^{-1}. The reconstructed empirical data, however, shows that $\frac{WR_c}{I_p} \approx 60$ J·m·kA^{-1}. The discrepancy may be due to the simplification that the marginally stable profile extends from the first closed flux surface to the last closed flux surface when it is valid only between the pressure peak location and the last closed flux surface. Nevertheless, the reconstructed data shows that there is a linear relationship between stored energy and plasma current that can be used to estimate the stored energy without having to fully reconstruct

the plasma. The stored energy-current relationship is used to estimate the energy confinement time of various shots with different compositions of heating frequencies. The trend shows a lower confinement time for a greater fraction of 2.45 GHz heating power. It is surmised that 2.45 GHz heating leads to the creation of more bulk electrons that do not have enough energy to be mirror trapped and are therefore lost to the floating coil supports through parallel transport. The eradication of the supports in the next phase of operation may significantly alter the confinement time.

10.3 Future Work and Levitation

A lot has been accomplished in the course of this thesis work, but there is ample future work to be pursued on the magnetic diagnostics and the Levitated Dipole Experiment project. Some potential magnetics hardware improvements have already been discussed at the conclusion of Ch. 2.

There can be several advances made in the reconstruction process discussed in Ch. 6. Although a lot of the procedures have been automated, they still rely too much on human control. Further automation will not only free the person from tedious work, but it will also allow the reconstructions to be done in an orderly manner. With respect to the physics of reconstruction, additional pressure models may be devised to describe the plasma more accurately. In particular, as mentioned in Ch. 8, there may be two pressure peaks when both microwave frequencies are used to heat the plasma. A two peak model may be developed and tested to check whether there indeed are two peaks when both frequencies are used.

As for the LDX apparatus itself, the next step in its operation is the levitation of the floating coil. As the name LDX implies, levitation is an important and necessary part of the experiment. One of the main improvements levitation may bring is the attainment of higher beta. Because of the elimination of parallel end losses, the energy confinement time is expected to increase as well. It has been alluded, if not stated, in Ch. 1 that the ultimate goal of LDX is to provide a physics basis for verifying the feasibility of utilizing the levitated dipole concept in a reactor design. To this end,

the ability to levitate a massive superconducting magnet using a feedback control system is in itself a momentous accomplishment. But more interesting is the unique physics results that only a levitated dipole can bring. If we can show that a plasma confined by a levitated dipole can support a higher beta and have a longer energy confinement time, that would lend a lot of support to the feasibility of a levitated dipole reactor. Magnetic diagnostics will continue to play a key role through this phase of the experiment by measuring these key parameters. Levitation is truly the next milestone in our experiment.

Appendix A

Figures

Figure A-1: Armadillo slaying lawyer.

Figure A-2: Armadillo eradicating national debt.

Appendix B

Reconstruction codes

This appendix describes some IDL codes involved in the reconstruction algorithm.

The first step in the reconstruction process is deducing the floating coil current from Hall probe measurements. The following codes retrieve Hall probe data from the mdsplus tree, use the calibrated magnetic field values to define a function of the floating coil current, and use the amoeba minimization scheme to find the best fit current:

```
function smoother_f, time, sensor
     y = mdsvalue(sensor)
     ;str = 'dim_of(' + '\r' + strmid(strtrim(sensor, 1), 2) + ')'
     str = 'dim_of(' + strtrim(sensor, 1) + ')'
     x = mdsvalue(str)
     i = (x[1048574] - x[0]) / 1048574 ; the sampling interval is found.
     j = -long(x[0] / i) ; the index for time = 0 is found.
     k = long(time / i) + j ; the index for the desired time is found.
     yavg = mean(y[0:k])
     print, yavg
     return, yavg
end



function automatic_f, shot, time
```

```
     mdsconnect, 'jove.psfc.mit.edu:8100'
     mdsopen, 'magnetics', shot
     m = fltarr(18, /nozero)
     m[0] = smoother_f(time, '\rhall1n')
     m[1] = smoother_f(time, '\rhall1p')
     m[2] = smoother_f(time, '\rhall2n')
     m[3] = smoother_f(time, '\rhall2p')
     m[4] = smoother_f(time, '\rhall3n')
     m[5] = smoother_f(time, '\rhall3p')
     m[6] = smoother_f(time, '\rhall4n')
     m[7] = smoother_f(time, '\rhall4p')
     m[8] = smoother_f(time, '\rhall5n')
     m[9] = smoother_f(time, '\rhall5p')
     m[10] = smoother_f(time, '\rhall6n')
     m[11] = smoother_f(time, '\rhall6p')
     m[12] = smoother_f(time, '\rhall7n')
     m[13] = smoother_f(time, '\rhall7p')
     m[14] = smoother_f(time, '\rhall8n')
     m[15] = smoother_f(time, '\rhall8p')
     m[16] = smoother_f(time, '\rhall9n')
     m[17] = smoother_f(time, '\rhall9p')
     mdsclose
     mdsdisconnect
     return, m
end


function fields_f, shot, lin_time
     raw = automatic_f(shot, lin_time)
     alpha = []
     beta = []
     gain = []
     mdsopen, 'magnetics', shot
     vcc = smoother_f(lin_time, '\VCC')
     mdsclose
     B = (1 / beta) * (raw / (gain * vcc) - alpha) / 10^4
```

```
     return, B
end


pro input_f, shot, time, p, r, f, B, f_current, h_current, h_on, z
     {}
end


function chisquared_f, I
     I = long(I)
     input_f, 50513029, 0, 0.000000001, 0.75, 1.0, [], I, 0, 0, -0.034
     spawn, 'dipoleq -f ' + strtrim(string(50513029), 1) + '_' + strtrim(string(0), 1) + '.in'
     ;spawn, 'rm *.hdf'
     spawn, 'rm *.pdf'
     spawn, 'rm *gs2.out'
     spawn, 'rm *PsiGrid.out'
     ;if I[1] lt 0 then str = strmid(strtrim(string(I[1]), 1), 0, 6) else str =
     strmid(strtrim(string(I[1]), 1), 0, 5)
     str = strmid(strtrim(string(-0.034), 1), 0, 6)
     file = 'F' + strtrim(string(I), 1) + 'Z' + str + '_Meas.out'
     x = read_ascii(file, data = 9)
     all = x.field1
     chi_squared = all[1, 22]
     printf, 2, 'F' + strtrim(string(I), 1) + 'Z' + str, chi_squared
     return, chi_squared
end


pro reconstruction_amoeba_f, shot, lin_time
     openw, 2, strtrim(string(shot), 1) + '_' + strtrim(string(lin_time), 1) + '.dat'
     minimum = amoeba(0.0001, function_name = 'chisquared_f', function_value = value, ncalls =
     number, p0 = 875250, scale = 80000)
     print, 'I = ', minimum
     print, 'chi-squared = ', value[0]
     print, 'number calls = ', number
```

```
     printf, 2, 'I = ', minimum
     printf, 2, 'chi-squared = ', value[0]
     printf, 2, 'number calls = ', number
     close, 2
end
```

The body of `input_f` has been suppressed because of its length, but the subroutine basically produces an input file that is read by the equilibrium code, DipolEq, which is called by the `chisquared_f` function. The contents of some arrays have been suppressed as well since they just contain numbers that take up space.

Upon obtaining the vacuum field corresponding to the best fit floating coil current, the total field is calculated by adding the calibrated measurements from the B_p coils and flux loops. The following codes subtract the integrator drift from B_p coil and flux loop data, find the total field, use it to define a function of the pressure profile parameters, and use the amoeba method to find the best fit parameter values:

```
function drift_helm, time, lin_time, ecrh_on, sensor
; this program attempts to eliminate the linear drift in the data caused by the integrator drift.
     raw = '\r' + strmid(sensor, 2)
     yr = mdsvalue(raw)
     yr = abs(yr)
     if max(yr) gt 9.8 then begin ; if the raw signal is ever greater than 9.8 then no further
          print, 100 ; analysis is done.
          return, 100
          end
     y = mdsvalue(sensor)
     str = 'dim_of(' + strtrim(sensor, 1) + ')'
     x = mdsvalue(str)
     y = smooth(y, 400, /edge_truncate)
     i = (x[1048574] - x[0]) / 1048574 ; the sampling interval is found.
     j = -long(x[0] / i) ; the index for time = 0 is found.
     m = long(lin_time / i) + j ; the index for the end/beginning time of the linear regime.
     if lin_time le 0 then begin
          ys = y[0:m] ; these new vectors are essentially truncated versions of x and y so that
          xs = x[0:m]     ; they only contain pre-trigger values.
```

```
     endif else begin
          ys = y[m:1048574] ; these vectors are also truncated versions of x and y so that
          xs = x[m:1048574] ; they only contain the end values.
     endelse
     w = linfit(xs, ys) ; w contains the coefficients of the linear regression.
     y = y - (w[0] + w[1] * x) ; the linear drift is subtracted here.
     y = y - y[j] ; y @ t = 0 is zeroed.
     plot, x, y
     final = '\f' + strmid(sensor, 2) ; the final signal goes into this node.
     expr = 'build_signal(build_with_units($, $), *, build_with_units(build_dim(*, $), $))'
     if strmid(sensor, 2, 1) eq 'm' then units = "Tesla" else units = "Weber"
     ;mdsput, final, expr, y, units, x, "sec"
     k = long(time / i) + j ; the index for the desired time is found.
     l = long(ecrh_on / i) + j ; the index for the ecrh turn on time.
     print, y[k] - y[l]
     return, y[k] - y[l]
end


function automatic, shot, time, lin_time, ecrh_on
     ;mdsconnect, 'jove.psfc.mit.edu:8100'
     mdsopen, 'magnetics', shot
     diam = fltarr(26, /nozero)
     diam[0] = drift_helm(time, lin_time, ecrh_on, '\rmag1n')
     diam[1] = drift_helm(time, lin_time, ecrh_on, '\rmag1p')
     diam[2] = drift_helm(time, lin_time, ecrh_on, '\rmag2n')
     diam[3] = drift_helm(time, lin_time, ecrh_on, '\rmag2p')
     diam[4] = drift_helm(time, lin_time, ecrh_on, '\rmag3n')
     diam[5] = drift_helm(time, lin_time, ecrh_on, '\rmag3p')
     diam[6] = drift_helm(time, lin_time, ecrh_on, '\rmag4n')
     diam[7] = drift_helm(time, lin_time, ecrh_on, '\rmag4p')
     diam[8] = drift_helm(time, lin_time, ecrh_on, '\rmag5n')
     diam[9] = drift_helm(time, lin_time, ecrh_on, '\rmag5p')
     diam[10] = drift_helm(time, lin_time, ecrh_on, '\rmag6n')
     diam[11] = drift_helm(time, lin_time, ecrh_on, '\rmag6p')
     diam[12] = drift_helm(time, lin_time, ecrh_on, '\rmag7n')
```

```
diam[13] = drift_helm(time, lin_time, ecrh_on, '\rmag7p')
diam[14] = drift_helm(time, lin_time, ecrh_on, '\rmag8n')
diam[15] = drift_helm(time, lin_time, ecrh_on, '\rmag8p')
diam[16] = drift_helm(time, lin_time, ecrh_on, '\rmag9n')
diam[17] = drift_helm(time, lin_time, ecrh_on, '\rmag9p')
diam[18] = drift_helm(time, lin_time, ecrh_on, '\rflux1')
diam[19] = -drift_helm(time, lin_time, ecrh_on, '\rflux2')
diam[20] = -drift_helm(time, lin_time, ecrh_on, '\rflux3')
diam[21] = -drift_helm(time, lin_time, ecrh_on, '\rflux4')
diam[22] = -drift_helm(time, lin_time, ecrh_on, '\rflux5')
diam[23] = -drift_helm(time, lin_time, ecrh_on, '\rflux7')
diam[24] = drift_helm(time, lin_time, ecrh_on, '\rflux8')
diam[25] = -drift_helm(time, lin_time, ecrh_on, '\rflux9')
smoother, '\phall1n'
smoother, '\phall1p'
smoother, '\phall2n'
smoother, '\phall2p'
smoother, '\phall3n'
smoother, '\phall3p'
smoother, '\phall4n'
smoother, '\phall4p'
smoother, '\phall5n'
smoother, '\phall5p'
smoother, '\phall6n'
smoother, '\phall6p'
smoother, '\phall7n'
smoother, '\phall7p'
smoother, '\phall8n'
smoother, '\phall8p'
smoother, '\phall9n'
smoother, '\phall9p'
fourier, '\pmir2'
fourier, '\pmir3'
;fourier, '\pmir4'
;fourier, '\pmir5'
;fourier, '\pmir6'
```

```
     ;fourier, '\pmir7'
     ;fourier, '\pmir8'
     ;fourier, '\pmir9'
     mdsclose
     ;mdsdisconnect
     return, diam
end


function fields, shot, time, lin_time, ecrh_on, vac
     raw = automatic(shot, time, lin_time, ecrh_on)
     NA = []
     tau = []
     B = (tau / NA) * raw
     m = B + vac
     return, m
end


pro input_r, shot, time, p, r, f, B, f_current, f_drop, h_current, h_on
     {}
end


function chisquared_r, p
     input_r, 50513029, 5.95, p[0], 0.77, p[1], [] , 904000, 2005, 0, 0
     spawn, 'dipoleq -f ' + strtrim(string(50513029), 1) + '_' + strtrim(string(5.95), 1) + '_' +
     'r' + strmid(strtrim(string(0.77), 1), 0, 1) + strmid(strtrim(string(0.77), 1), 2, 2) + '.in'
     ;spawn, 'rm *.hdf'
     spawn, 'rm *.pdf'
     spawn, 'rm *gs2.out'
     spawn, 'rm *PsiGrid.out'
     file = 'p' + strmid(strtrim(string(p[0]), 1), 2, 3) + $
            'r' + strmid(strtrim(string(0.77), 1), 0, 1) + $
                  strmid(strtrim(string(0.77), 1), 2, 2) + $
            'f' + strmid(strtrim(string(p[1]), 1), 0, 1) + $
```

```
                strmid(strtrim(string(p[1]), 1), 2, 2) + '_Meas.out'
     x = read_ascii(file, data = 9)
     all = x.field1
     chi_squared = all[1, 30]
     printf, 2, 'p' + strmid(strtrim(string(p[0]), 1), 2, 3) + $
                'r' + strmid(strtrim(string(0.77), 1), 0, 1) + $
                      strmid(strtrim(string(0.77), 1), 2, 2) + $
                'f' + strmid(strtrim(string(p[1]), 1), 0, 1) + $
                      strmid(strtrim(string(p[1]), 1), 2, 2), chi_squared
     return, chi_squared
end



pro reconstruction_amoeba_r, shot, time, r
     openw, 2, strtrim(string(shot), 1) + '_' + strtrim(string(time), 1) + '_' + 'r' +
     strmid(strtrim(string(r), 1), 0, 1) + strmid(strtrim(string(r), 1), 2, 2) + '.dat'
     minimum = amoeba(0.0001, function_name = 'chisquared_r', function_value = value, ncalls =
     number, p0 = [0.050, 1.10], scale = [0.010, 0.10])
     print, 'p = ', minimum[0], 'r = ', r, 'f = ', minimum[1]
     print, 'chi-squared = ', value[0]
     print, 'number calls = ', number
     printf, 2, 'p = ', minimum[0], 'r = ', r, 'f = ', minimum[1]
     printf, 2, 'chi-squared = ', value[0]
     printf, 2, 'number calls = ', number
     close, 2
end
```

Most often, the amoeba minimization is used only after the approximate location of the minimum is found through the brute force method. The brute force method is carried out with the following code:

```
pro input, shot, time, p, r, f, B, f_current, f_drop, h_current, h_on
     {}
end



pro reconstruction, shot, time, lin_time, ecrh_on, f_current, f_drop, h_current, h_on, vac
```

```
;a = automatic(shot, time, lin_time, ecrh_on)
;NA = []
;tau = []
;B = (tau / NA) * a + vac
B = []
p = [0.005, 0.010, 0.020, 0.030, 0.040, 0.050, 0.060, 0.070]
;r = [0.67, 0.69, 0.71, 0.73, 0.75, 0.77, 0.79, 0.81, 0.83]
r = 0.77
f = [0.80, 0.90, 1.00, 1.10, 1.20, 1.30, 1.40, 1.50]
openw, 2, strtrim(string(shot), 1) + '_' + strtrim(string(time), 1) + '.dat'
parameters = fltarr(3, 64, /nozero)
chi_squared = fltarr(64, /nozero)
for i = 0, 7 do begin
     for j = 0, 0 do begin
          for k = 0, 7 do begin
               input, shot, time, p[i], r[j], f[k], B, f_current, f_drop, h_current, h_on
               spawn, 'dipoleq -f ' + strtrim(string(shot), 1) + '_' + strtrim(string(time), 1)
               + '.in'
               file = 'p' + strmid(strtrim(string(p[i]), 1), 2, 3) + $
                      'r' + strmid(strtrim(string(r[j]), 1), 0, 1) + $
                            strmid(strtrim(string(r[j]), 1), 2, 2) + $
                      'f' + strmid(strtrim(string(f[k]), 1), 0, 1) + $
                            strmid(strtrim(string(f[k]), 1), 2, 2) + '_Meas.out'
               x = read_ascii(file, data = 9)
               all = x.field1
               printf, 2, 'p' + strmid(strtrim(string(p[i]), 1), 2, 3) + $
                          'r' + strmid(strtrim(string(r[j]), 1), 0, 1) + $
                                strmid(strtrim(string(r[j]), 1), 2, 2) + $
                          'f' + strmid(strtrim(string(f[k]), 1), 0, 1) + $
                                strmid(strtrim(string(f[k]), 1), 2, 2), all[1, 30]
               ;n = 90 * i + 10 * j + k
               ;n = 10 * i + k
               n = 8 * i + k
               parameters[*, n] = [p[i], r[j], f[k]]
               chi_squared[n] = all[1, 30]
          endfor
```

```
          endfor
     endfor
     chi_min = min(chi_squared, m)
     printf, 2, parameters[*, m], chi_min
     close, 2
end
```

The execution of the brute force method prior to running the amoeba scheme helps prevent it from converging to a local minimum.

Bibliography

[1] H. L. Berk. *Phys. Fluids*, 19:1255, 1976.

[2] P. R. Bevington and D. K. Robinson. *Data Reduction and Error Analysis for the Physical Sciences*. McGraw-Hill, 1992.

[3] B.J. Braams, W. Jilge, and K. Lackner. *Nucl. Fusion*, 26(6):699, 1986.

[4] A. Chan, M. Xia, and L. Chen. *J. Geophys. Res.*, 99:17351, 1994.

[5] W. W. Connor and R. J. Hastie. *Phys. Fluids*, 19:1727, 1976.

[6] A. J. Dessler and E. N. Parker. *J. Geophys. Res.*, 64:2239, 1959.

[7] J. R. Ferron, M. L. Walker, L. L. Lao, H. E. St. John, D. A. Humphreys, and J. A. Leuer. *Nucl. Fusion*, 38:1055, 1998.

[8] J. P. Freidberg. *Ideal Magnetohydrodynamics*. Plenum Press, 1987.

[9] D. T. Garnier, A. Hansen, M. E. Mauel, E. Ortiz, A. C. Boxer, J. Ellsworth, I. Karim, J. Kesner, S. Mahar, and A. Roach. *Phys. Plasmas*, 13:056111–1, 2006.

[10] D. T. Garnier, A. K. Hansen, J. Kesner, M. E. Mauel, P. C. Michael, J. V. Minervini, A. Radovinsky, A. Zhukovsky, A. Boxer, J. Ellsworth, I. Karim, and E. Ortiz. Design and initial operation of the ldx facility. *Fusion Engineering and Design*, to be published, 2006.

[11] D. T. Garnier, J. Kesner, and M. E. Mauel. *Phys. Plasmas*, 6:3431, 1999.

[12] D. A. Gates, J. R. Ferron, M. Bell, T. Gibney, R. Johnson, R. J. Marsala, D. Mastrovito, J. E. Menard, D. Mueller, B. Penaflor, S. A. Sabbagh, and T. Stevenson. *Nucl. Fusion*, 46:17, 2006.

[13] E. Hameiri, P. Laurence, and M. Mond. *J. Geophys. Res.*, 96:1513, 1991.

[14] A. K. Hansen, A. C. Boxer, J. L. Ellsworth, D. T. Garnier, I. Karim, J. Kesner, M. E. Mauel, and E. E. Ortiz. *J. Fus. Energy*, to be published, 2006.

[15] A. Hasegawa. *Comm. Pl. Phys. & Cont. Fus.*, 1(147), 1987.

[16] A. Hasegawa, L. Chen, and M. E. Mauel. *Nucl. Fusion*, 30:2405, 1990.

[17] R. D. Hazeltine and J. D. Meiss. *Plasma Confinement*. Perseus Books, 1992.

[18] I. H. Hutchinson. *Principles of Plasma Diagnostics*. Cambridge University Press, 2002.

[19] I. Karim, M. E. Mauel, J. L. Ellsworth, A. C. Boxer, D. T. Garnier, A. K. Hansen, J. Kesner, and E. E. Ortiz. *J. Fus. Energy*, to be published, 2006.

[20] J. Kesner, L. Bromberg, M. Mauel, D. Garnier, and J. M. Dawson. The dipole fusion confinement concept. Technical report, 1998.

[21] N. A. Krall. *Phys. Fluids*, 9:820, 1966.

[22] S. I. Krasheninnikov and P. J. Catto. *Phys. Plasmas*, 7:626, 2000.

[23] N. S. Krasheninnikova and P. J. Catto. *Phys. Plasmas*, 12:032101, 2005.

[24] L. L. Lao, J. R. Ferron, R. J. Groebner, W. Howl, H. St. John, E. J. Strait, and T. S. Taylor. *Nucl. Fusion*, 30:1035, 1990.

[25] L. L. Lao, H. St. John, R. D. Stambaugh, A. G. Kellman, and W. Pfeiffer. *Nucl. Fusion*, 25:1611, 1985.

[26] B. Levitt, D. Maslovsky, and M. Mauel. *Phys. Plasmas*, 9, 2002.

[27] W. Lochte-Holtgreven. *Plasma Diagnostics*. American Institute of Physics, 1995.

[28] R. H. Lovberg. *Plasma Diagnostic Techniques*, chapter 3, pages 69–112. Academic Press, 1965.

[29] D. Maslovsky, B. Levitt, and M. Mauel. *Phys. Rev. Lett.*, 10, 2003.

[30] D. Maslovsky, B. Levitt, and M. Mauel. *Phys. Plasmas*, 10, 2003.

[31] M. E. Mauel. *J. Phys. IV*, 7, 1997.

[32] M. E. Mauel. Another model pressure profile. Technical report, Columbia University, 2005.

[33] M. E. Mauel. Calculation of mutual inductance between f-coil and plasma. Technical report, Columbia University, 2005.

[34] M. E. Mauel. Calculation of mutual inductance between f-coil and plasma. Technical report, Columbia University, 2005.

[35] M. E. Mauel. Dipole equilibrium with anisotropic pressure. Technical report, Columbia University, 2005.

[36] M. E. Mauel. Dipole equilibrium with anisotropic pressure (revised). Technical report, Columbia University, 2005.

[37] M. E. Mauel. Equilibrium integral relations for dipole plasma. Technical report, Columbia University, 2005.

[38] M. E. Mauel. Measuring the plasma current profile in ldx. Technical report, Columbia University, 2005.

[39] E. E. Ortiz, A. C. Boxer, J. L. Ellsworth, D. T. Garnier, A. K. Hansen, I. Karim, J. Kesner, and M. E. Mauel. *J. Fus. Energy*, to be published, 2006.

[40] W. H. Press, B. P. Flannery, S. A. Teukolsky, and W. T. Vetterling. *Numerical Recipes in C: The Art of Scientific Computing*. Cambridge University Press, 1992.

[41] M. N. Rosenbluth and C. L. Longmire. *Ann. Phys.*, 1:120, 1957.

[42] H. Saitoh, Z. Yoshida, H. Himura, J. Morikawa, and M. Fukao. *Phys. Plasmas*, 11:3331, 2004.

[43] H. Saitoh, Z. Yoshida, C. Nakashima, H. Himura, J. Morikawa, and M. Fukao. *Phys. Rev. Lett.*, 92:255005–1, 2004.

[44] N. Sckopke. *J. Geophys. Res.*, 71:3125, 1966.

[45] A. N. Simakov, R. J. Hastie, and P. J. Catto. *Phys. Plasmas*, 7:3309, 2000.

[46] S. von Goeler, S. Jones, R. Kaita, S. Bernabei, W. Davis, H. Fishman, G. Gettelfinger, D. Ignat, F. Paoletti, G. Petravich, F. Rimini, P. Roney, J. Stevens, and W. Stodiek. Camera for imaging hard x rays from suprathermal electrons during lower hybrid current drive on pbx-m. *Rev. Sci. Instrum.*, 65:1621, May 1994.